Mathematical Methods for Classifying Fast Radio Bursts

A Thesis

Submitted for the Degree of

Doctor of Philosophy

in the Faculty of Science

by

Shruti Bhatporia

Department of Mathematics and Applied Mathematics
University of Cape Town
Cape Town – 77 00, South Africa

February 2025

Declaration

I hereby declare that the work reported in this doctoral thesis titled "Mathematical Methods for Classifying FRBs" is entirely original and is the result of investigations carried out by me in the Department of Mathematics and Applied Mathematics, University of Cape Town, Cape Town, under the supervision of Prof. Amanda Weltman.

I further declare that this work has not formed the basis for awarding any degree, diploma, fellowship, associateship or similar title of any University or Institution.

Date: 19/02/2025
Cape Town, South Africa

Shruti Bhatporia
Department of Mathematics and Applied Mathematics
University of Cape Town

Supervisor: Prof. Amanda Weltman
Department of Mathematics and Applied Mathematics
University of Cape Town

To my family,

who always stands by me, no matter what.

Acknowledgements

The successful completion of this dissertation would not have been possible without the invaluable guidance and support of many individuals. I am especially grateful to my supervisor, Professor Amanda Weltman. Her expertise in Fast Radio Bursts and Cosmology proved to be instrumental in shaping this work. Professor Weltman's willingness to share her knowledge and provide constant encouragement throughout my PhD journey was fundamental. Her patience and insightful feedback helped me refine my research and develop my skills as a scientist.

I would also like to express my sincere gratitude to the members of my thesis committee, Dr. [] and Dr. []. Their insightful comments and suggestions during the development of this dissertation significantly enhanced its quality. Their critical feedback pushed me to consider new perspectives and strengthen my arguments.

Furthermore, I am indebted to my colleagues in the Department of Mathematics and Applied Mathematics. Professor Jeff Murugan, Surajit Kalita, Anthony Walters, Dr. Mugundhan Vijayraghavan, and others fostered a supportive research environment. Stimulating discussions and a collaborative spirit were invaluable assets throughout my PhD journey. Their willingness to share ideas and offer a helping hand greatly contributed to my progress. This journey wouldn't have been complete without the unwavering support of my friends. Ranjani, Guy, Vrunda, Samskruthi, Farzana, Atique, Ruach, Margarita, Josh, Catherine, and Nitin provided invaluable emotional support throughout my three years in Cape Town. Their presence helped me navigate both the challenges and triumphs of graduate school. Their friendship offered a sense of community and a welcome escape from the pressures of research.

I gratefully acknowledge the financial support from the NRF Postgraduate Funding through grant number MND200622534919. This grant was instrumental in enabling my research and

allowing me to focus fully on my studies. Additionally, I am grateful for the support from the University of Cape Town Vice Chancellor's Future Leaders 2030 Awards programme and the South African Research Chairs Initiative of the Department of Science and Technology and the National Research Foundation. These funding opportunities provided crucial resources for my research endeavours.

Finally, my deepest appreciation goes to my family and friends for their unwavering love and support throughout my doctoral studies. Their constant encouragement and belief in me have been a source of immense strength, particularly during the toughest of times. In particular, I would like to express my heartfelt gratitude to my parents for their emotional support. Their love and unwavering faith have been a constant source of motivation.

Preface

The recent extragalactic discovery of **Fast Radio Bursts (FRBs)** has ignited a whirlwind of research, and numerous fundamental questions about them are being studied. This thesis delves into this field, aiming to bridge the gap in our exploration of FRB populations.

The FRBs are cosmic transients characterised by powerful millisecond-duration radio waves emanating from extragalactic distances. Their origins remain a mystery, fueling ongoing debate regarding progenitor models. Despite their ephemeral nature, the energy output of a single FRB can surpass the daily radiant energy emitted by a main sequence star in a radio band. While undoubtedly powerful astrophysical phenomena, their transient nature presents a significant challenge in pinpointing source locations. The discovery of the first FRB in 2001 was initially met with scepticism and attributed to instrumental error. However, advancements in telescope sensitivity and data analysis techniques have led to the detection of numerous subsequent FRBs, solidifying their status as a novel class of astronomical phenomenon. Unveiling the mysteries surrounding FRBs encompasses a multifaceted research endeavour. Astronomers are actively engaged in identifying their host environments, elucidating the mechanisms responsible for their tremendous energy release, and exploring potential sub-classifications within the FRB population. By deciphering the secrets of FRBs, we stand to gain invaluable insights into extreme astrophysical processes and the nature of the distant Universe.

The Hydrogen Intensity Real-time eXperiment (HIRAX) is a next-generation instrument specifically designed to detect and localise FRB along with intensity mapping. To efficiently manage the high-volume data stream generated by HIRAX, a dedicated FRB processing pipeline is essential. We explore FRB rates with the HIRAX instrument in this thesis. We also discuss the FRB detection pipeline with this radio telescope.

In recent decades, numerous modifications to general relativity have been proposed to address various cosmological and astrophysical challenges. While ongoing observations have ruled out many of these models, some remain viable with observationally-derived constraints on their parameters. Notably, FRBs have emerged as powerful tools for constraining cosmological and fundamental physics theories. As a part of this thesis, we investigate the implications of a generic modified gravity theory on the gravitational lensing of FRBs. We utilise a set of FRB observations to constrain the proportion of dark matter composed of primordial black holes within this theoretical framework. Furthermore, we demonstrate that modified gravity introduces a "screening effect" on gravitational lensing, akin to the influence of plasma acting as a scattering screen for light rays.

In addition, this study explores the fundamental nature of FRBs by leveraging Topological Data Analysis (TDA), a burgeoning field in mathematics for data science. TDA offers a unique perspective for characterising the underlying geometric structure of complex, high-dimensional datasets. In the context of FRBs – short, intense radio transients with unknown origins – TDA provides a novel approach to investigating their properties. We employ the mapper algorithm, a core technique within TDA, to visualise the intrinsic topological structure within a substantial FRB dataset. This algorithm identifies and connects data points based on shared features, essentially constructing a map of the complex relationships within the data. By analysing the resulting mapper graph, we can glean insights into the underlying organisation of the FRB population. The application of TDA in this study reveals the existence of three distinct FRB populations. These populations are differentiated based on their inferred radio signal properties, potentially hinting at diverse source environments or progenitor mechanisms. Furthermore, the analysis demonstrates a robust structure within the mapper graph, suggesting a non-random organisation of the FRB data. This structure potentially encodes information about the FRB morphology (shape) and energy distribution. Additionally, by analysing the proximity of FRBs within the mapper graph, we can identify candidate non-repeating FRBs that might exhibit repeating behaviour in the future. This capability stems from TDA's potential to capture underlying relationships that might be missed by traditional data analysis methods. This work underscores the potential of TDA as a powerful tool for unravelling the origin and nature of FRBs. By providing a novel framework for analysing complex astronomical data, TDA offers exciting possibilities for advancing our understanding of these mysterious objects.

The MeerKAT telescope in South Africa leverages the MeerTRAP real-time processing pipeline for efficient detection of Fast Radio Bursts (FRBs) within the deluge of data it collects. MeerTRAP functions as a high-throughput filter, meticulously sifting through the radio waves to identify the faint yet characteristic signatures of FRBs. This powerful framework boasts adaptability to various computing architectures, ensuring optimal performance during data

analysis. MeerTRAP meticulously eliminates background noise while searching for the short, impulsive radio signals emblematic of FRBs. This real-time processing capability is paramount for capturing the ephemeral nature of FRBs and maximizing the scientific output gleaned from MeerKAT observations. To add to this facility, as a part of this thesis, we developed a preprocessing module to aid the Fast Radio Burst Intelligent Distinguisher (FRBID) classifier of MeerTRAP pipeline as our last chapter in this thesis.

The following chapters are meticulously structured to guide the reader through the research journey, beginning with a comprehensive review of the existing literature in Chapter 1. Chapter 2 details on upcoming HIRAX telescope receiver chain for detecting FRBs. Chapter 3 presents the analysis of gravitational lensing of FRBs and using them as a probe for constraining fraction of dark matter, followed by a thorough discussion of categorising repeaters and non-repeaters FRBs with topological data analysis Chapter 4. Chapter 5 looks at the pre-processing of FRBID input data for MeerTRAP pipeline. Finally, Chapter 6 concludes the thesis by summarising the key findings, limitations, and future research directions.

List of Publications

I confirm that I have been granted permission by the University of Cape Town's Doctoral Degrees Board to include the following publication(s) in my PhD thesis, and where co-authorships are involved, my co-authors have agreed that I may include the publication:

- 'A Topological Data Analysis of the CHIME/FRB Catalogues', **Bhatporia S.**, Walters A., Murugan J., Weltman A., 2023, arXiv, arXiv:2311.03456. doi:10.48550/arXiv.2311.03456

Signature: Date: 01/11/2024

Student Name: Shruti Bhatporia Student Number: BHTSHR001

Table of contents

List of figures

List of tables

1 Introduction

For a long time, the universe was thought to be static. The visible matter of the universe, in the form of celestial objects, was assumed long-lived and didn't show rapid change in their properties during their lifetime. However, recent observations reveal a dynamic aspect of the universe, where compact objects exhibit continual changes in energy output and proper motion relative to Earth. Radio transients represent a particularly intriguing class within this dynamic landscape. These sources emit short-duration bursts or pulses of radio waves, often due to coherent emission mechanisms. The radio transient category encompasses diverse phenomena, from pulsars with highly precise periodicities to enigmatic Fast Radio Bursts (FRBs) – sources of immense energy output and as yet unknown periodicity.

The field of radio astronomy flourished throughout the 1960s, culminating in a breakthrough discovery in 1967. Jocelyn Bell Burnell, a graduate student at the University of Cambridge, used a radio telescope to detect a series of regularly spaced pulses from an enigmatic celestial object. This object, later identified as the first pulsar [2], emitted pulses with a remarkably precise separation of $1.337\,\mathrm{s}$. This pioneering discovery laid the groundwork for the characterisation of pulsars – rapidly rotating neutron stars possessing intense magnetic fields, extraordinary densities, and distinctive beamed radio emissions. Pulsars with spin periods ranging from $1.4\,\mathrm{ms}$ to tens of seconds and magnetic field strengths of $10^8 \mathrm{to} 10^{14}$ G, resemble interstellar lighthouses, emitting periodic pulses of radiation that sweep across Earth's line of sight, analogous to a lighthouse beam. The interstellar medium (ISM) contains free electrons that interact with and disperse radio waves. This phenomenon, known as dispersion, offers a valuable tool for estimating distances to pulsars. On the other hand, FRBs have opened up a new window in astronomy since their detection from an archival search of Parkes radio telescope in 2007 [3]. These are bright, short-lived transient events observed in the radio spectrum within approximately the 100 MHz to 8 GHz frequency range [4]. The expected rate

of FRBs across the entire sky is estimated to be approximately $100 - 1000$ per day [5]. FRBs show at some level similarities with galactic pulsars, but their distance is proven to be much higher than that of pulsars. With the remarkable exception of FRB 200428, which is verified to have originated from a Galactic magnetar SGR $1935 + 2154$ [6–8], their relatively large DMs imply that the majority of these FRBs have extragalactic origins. Dispersion manifests as a time delay, Δt, between the arrival times of high- and low-frequency components within a pulse. This delay is directly related to the dispersion measure (DM), a quantity that integrates the total column density of free electrons encountered along the path to the pulsar. As described earlier, the DM and the observed dispersion effect, along with a model for Galactic electron density, allow astronomers to estimate the distance to pulsars. A particularly noteworthy application of this technique is the Lorimer Burst, a groundbreaking discovery in radio astronomy. This extragalactic radio transient exhibited a DM of a remarkably high value: $375\,\mathrm{cm}^{-3}\,\mathrm{pc}$. This measurement provided crucial evidence for the extragalactic origin of the burst. This burst, inferred to be a catastrophic event, had an estimated energy of 10^{33} J and a size less than 1500 km. The luminosity of the Lorimer Burst was approximately 10 to 12 orders of magnitude brighter than any known source at that time, marking it as a prototype of a new class of distant radio sources. Understanding the nature of transient radio signals, their origins, and their potential links to the large-scale structure of the cosmos remains an active area of research. This quest holds immense promise for advancing our cosmological knowledge, fueled by the development of ever more innovative radio telescopes.

The Canadian Hydrogen Intensity Mapping Experiment (CHIME) has emerged as a revolutionary instrument in the quest to understand FRBs. Unlike conventional radio telescopes that meticulously scan the sky in sections, CHIME boasts a wide field of view, enabling it to observe a significantly larger celestial area simultaneously. This panoramic capability has revolutionised our understanding of FRBs. CHIME's immense data collection capacity began yielding significant results in 2018. The initial understanding of Fast Radio Bursts (FRBs) as singular events underwent a significant revision with the detection of eight repeating FRBs in 2019 [9]. Unlike the previously observed, one-time FRBs, these bursts exhibited multiple flares, suggesting a potentially more dynamic environment for their origin. This groundbreaking discovery challenged the prevailing view of FRBs and opened exciting new avenues for further exploration. The substantial data volume from these repeating FRBs has also facilitated the development of novel analysis techniques, as exemplified by the work of [10]. In a revolutionary discovery, the Canadian Hydrogen Intensity Mapping Experiment (CHIME) collaboration reported the detection of over 500 FRBs in its inaugural year of operation alone[1]. This dramatic increase in FRB detections significantly challenged previous estimations regarding their

[1] https://www.chime-frb.ca/

abundance in the cosmos. Furthermore, the CHIME/FRB collaboration has made significant progress in elucidating the intrinsic properties of FRBs. Through detailed analyses of pulse characteristics and the interstellar medium's influence on the signal, they were able to measure distances to some FRBs. Crucially, these distance measurements definitively established the extragalactic nature of these enigmatic objects. Further intrigue arose from CHIME's contribution to uncovering a potential link between FRBs and magnetars, a particular class of ultra-dense neutron stars [8]. The 2020 detection of an exceptionally bright pulse from a magnetar – a highly magnetized neutron star – exhibited striking similarities to certain FRBs, suggesting a potential link between these two enigmatic phenomena. The CHIME has not only discovered a substantial population of these elusive bursts but has also provided critical data that is essential for unravelling the mysteries surrounding their origin and nature.

Discovered by PALFA survey and heavily followed up by CHIME and other telescopes, FRB 121102 [11], is a first of repeating FRBs. Discovered on UTC date 2 Nov 2012, this burst showcased a unique set of characteristics that set it apart from other known celestial sources. The bright individual pulse of FRB 121102 was detected at a DM of $375\,\mathrm{cm}^{-3}\,\mathrm{pc}$. This pulse, originating from an extragalactic source, exhibited an anomalously high DM, suggesting a significant distance. After accounting for the expected DM contribution from the Milky Way, approximately $330\,\mathrm{cm}^{-3}\,\mathrm{pc}$ of **extragalactic dispersion** was observed. Based on astronomical surveys, the density of the intergalactic medium is estimated to be around one electron per cubic meter, leading to an implied distance of $330\,\mathrm{Mpc}$ for FRB 121102. Further calculations [12], estimates as far as $1\,\mathrm{Gpc}$. This immense distance, coupled with the burst's inferred energetics of approximately 10^{33} J, suggested a catastrophic source mechanism, possibly involving phenomena like neutron star in-spirals, supernovae, or gamma-ray bursts.

The hunt for FRBs is an ongoing pursuit shrouded in mystery. These enigmatic transients emit millisecond-duration radio flashes, akin to cosmic needles in a haystack – infrequent, unpredictable, and evanescent. Current observations suggest FRBs are relatively rare events. By surveying a larger swath of the sky simultaneously, wide-FoV telescopes significantly enhance the probability of detecting FRBs in real-time. A larger sample size is crucial for drawing statistically robust inferences about FRBs. Are they a uniform population, or do distinct subclasses exist with varying frequencies or distributions? Wide-FoV instruments like CHIME and its successor, the High-Resolution Array (HIRAX), provide the data necessary to address these questions and refine our understanding of the FRB population. The success of CHIME has invigorated FRB research, demonstrating that wide-FoV telescopes are not merely advantageous but essential tools. The advent of even more powerful next-generation instruments like the Square Kilometre Array (SKA) promises to revolutionise our understanding

of FRBs. Wide-FoV telescopes are at the forefront of this exciting endeavour, leading the charge in deciphering the mysteries of these cosmic transients.

1.1 Fast Radio Bursts: Parameters and Properties

- **Duration:** The pulse duration of an FRB is a complex interplay between the intrinsic properties of the burst itself and the effects it experiences during propagation through interstellar space. Intrinsic Emission Time is the actual duration of the radio emission generated at the FRB source. This duration is believed to be very short, on the order of nanoseconds or tens of microseconds, based on theoretical models and observations of ultra-fast FRBs. Dispersion Smearing occurs as the FRB signal travels through the ISM, it interacts with free electrons. These electrons cause lower radio frequencies to experience a greater delay compared to higher frequencies, an effect known as dispersion. This differential delay stretches the pulse duration, making the observed pulse longer than the intrinsic emission time. Instrumental Response is the time resolution of the observing telescope. Telescopes with limited time resolution might not capture the full details of the short FRB pulse, leading to an underestimation of its true duration. Imperfect calibration of the telescope and data processing pipelines can introduce artefacts that mimic or mask the actual pulse duration. Careful calibration and sophisticated algorithms are necessary to extract the intrinsic pulse duration from the observed data.

$$\mathrm{W}^2 = (\mathrm{W_{int}})^2 + (\mathrm{t_{samp}})^2 + (\Delta \mathrm{t_{DM}})^2 + (\Delta \mathrm{t_{DM_{err}}})^2 + (\tau_\mathrm{s})^2 \tag{1.1}$$

where, W^2 is width_ms observed time resolution, $(\mathrm{W_{int}})^2$ is intrinsic pulse width, $(t_{samp})^2$ is sampling time, $(\Delta t_{DM})^2$ - dispersive delay across an individual frequency channel inversely proportional to the bandwidth, $(\Delta \mathrm{t_{DM_{err}}})^2$ - dispersive delay corresponds to slightly incorrect dispersion, $(\tau_s)^2$ - scattering timescales.

- **Flux Density:** It represents the total power received by a telescope per unit area and unit frequency bandwidth. For FRBs, the flux density is incredibly high, typically reaching thousands of Jyanskys during the burst duration, which can be milliseconds or even less. However, it is crucial to remember that this high flux density is measured over a very short time interval. The total energy output of an FRB, obtained by integrating the flux density over the entire pulse duration, is quite low compared to other astronomical objects. Figure 1.1 shows the transient phase space diagram for CHIME/FRBs, where repeaters to some extent show lower luminosity values. Furthermore, the observed flux density of an FRB is influenced by the distance to the source. FRBs from farther distances will exhibit lower observed flux densities due to the expansion of the signal during its

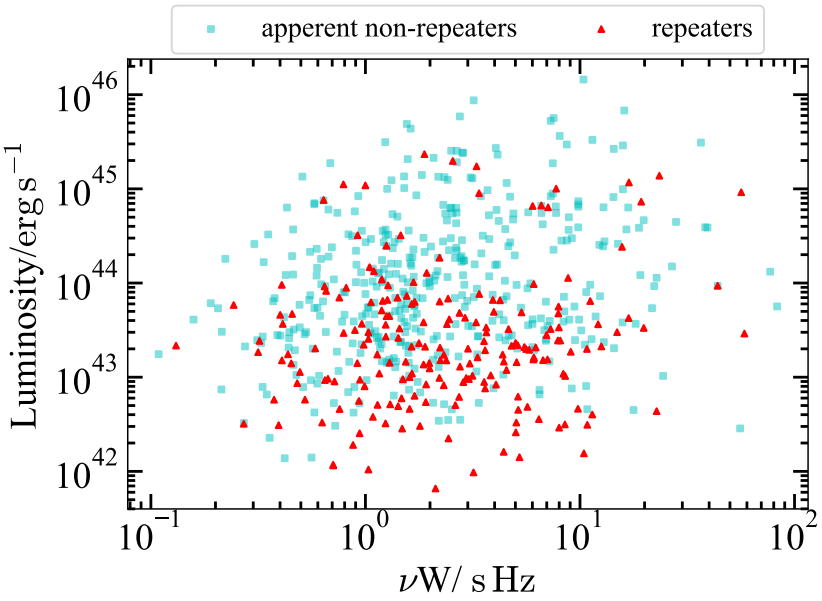

Figure 1.1 Collected FRBs, specifically with CHIME/FRB project so far for the measure of energy for phase space diagram. Repeaters seem to be of low energy comparatively, with observational effects.

propagation through the universe. Additionally, factors like interstellar scattering and intervening material within the Milky Way can further diminish the received flux density. By measuring the flux density and considering these distance and propagation effects, an estimation of the intrinsic luminosity and energies of FRBs is made.

- **Dispersion measure (DM):** The dispersion measure (DM) of a Fast Radio Burst (FRB) is not directly measured. Instead, it is inferred through analysis of the FRB's intrinsic properties. **Frequency Sweep:** FRBs propagating through interstellar space encounter free electrons in the i.e. These electrons introduce a frequency-dependent delay, where lower frequencies experience a greater delay compared to higher frequencies. This phenomenon manifests as a characteristic "dispersion sweep" within the FRB pulse itself. The signal is effectively stretched in time, with higher frequencies arriving first and lower frequencies trailing behind, creating a distinctive sweep from high to low frequencies.

  Dispersion Measure Calculation: When an electromagnetic (EM) wave propagates through a plasma, its different frequency components experience different phase velocities. This phenomenon is called dispersion. Plasma, an ionised gas, interacts with the electric and magnetic fields of the EM wave, causing a frequency-dependent delay. This delay is quantified by the dispersion measure in units of pc cm^{-3} (parsec cubic centime-

tre). Here's the relationship between DM, electron density n_e along the propagation path L, and the constant of proportionality $(e^2/(4\pi\varepsilon_0 m_e))$:

$$\mathrm{DM} = \frac{\mathrm{e}^2}{4\pi\varepsilon \mathrm{m_e}} \int \mathrm{n_e(l)dl}, \tag{1.2}$$

where, e is the elementary charge is the permittivity of free space, m_e is the electron mass, $n_e(l)$ is the electron density at a specific point l along the path length L.

In a dispersive medium like plasma, the phase velocity $v_p h$ of an EM wave depends on its frequency ω. However, information encoded in a wave packet travels at the group velocity v_g, which is different from the phase velocity. The group velocity can be calculated using the following relationship derived from the dispersion relation (the equation that describes the relationship between wave vector k and frequency ω in a medium):

$$v_g = d\omega/dk \tag{1.3}$$

In a plasma, the group velocity of an EM wave generally decreases with increasing frequency due to the dispersive nature of the medium. This means that higher frequency components of the wave travel slower than lower frequency components. This effect can lead to a broadening of the wave packet as it propagates through the plasma.

Analysis of the arrival times for various frequencies within an FRB burst allows for the measurement of the time delay, denoted by Δt. This time delay is directly proportional to the DM. The relationship between the time delay and the DM is described by the following equation;

$$\Delta \mathrm{t} = \mathrm{DM} \times \mathrm{constant} \tag{1.4}$$

The constant in this equation incorporates the specific observing frequencies employed. This allows astronomers to leverage the measured time delay (Δt) and the observing frequencies to directly calculate the DM of the FRB. The DM acts as a signature of the total number of electrons encountered by an FRB during its propagation. By analysing the "stretch" of the FRB signal, characterised by the time delay between different frequencies, astronomers can infer the DM. This value offers valuable insights into the distance travelled by the FRB. However, it's crucial to recognise that DM only reveals the total column density of electrons along the line of sight, not their specific distribution within the path. This limitation introduces some uncertainties in distance estimates for FRBs.

- **Rotation Measure (RM):** RM of an FRB offers a valuable window into the magnetised environment along the path the signal travels. It quantifies the total amount of Faraday rotation, where the plane of polarisation of the FRB's radio waves is rotated due to the presence of a magnetic field and charged particles in the ISM. A higher RM generally indicates a stronger magnetic field integrated along the line of sight. By measuring the RM, scientists can probe the overall magnetic field strength within the ISM surrounding the FRB source and within its host galaxy. The RM depends not only on the magnetic field strength but also on the total electron density along the propagation path. Combining RM measurements with other observations, like DM, can help disentangle the contributions of magnetic field and electron density within the ISM. If RM measurements reveal variations across different bursts from the same source, it could suggest a turbulent or structured magnetic field environment near the FRB progenitor. Therefore, the RM of an FRB serves as a unique probe for investigating the magnetised environment along the propagation path and within the FRB's host galaxy. By analysing the RM alongside other parameters, scientists can gain valuable insights into the physical conditions surrounding radio transients.

$$\mathrm{RM} = \frac{e^3}{2\pi m_e^2 c^4} \int_0^d n_e B_{||} \, \mathrm{d}l \,, \tag{1.5}$$

  where e is an electron charge, m_e is mass, c is the speed of light, magnetic field $B_{||}$ perpendicular to line of sight and d is the cosmological distance.

- **Non-repeating vs. Repeating:** Non-repeating FRBs: Chapter 4 investigates this topic for FRBs in length. This category constitutes the vast majority of FRBs detected so far. These bursts appear as singular events, emitting a single, powerful radio pulse and then remaining silent. The origin of the immense energy released within these objects and the reason for their apparent one-time nature remain a mystery. A much smaller population of FRBs exhibits repeated bursts from the same location. These bursts can vary in intensity and may show periodic or quasi-periodic behaviour. The discovery of repeaters has opened exciting avenues for studying FRBs in more detail. By monitoring the repeating bursts one can constrain on the physical properties of the source environment and shed light on the underlying mechanism responsible for FRB generation. Figure 1.2 shows a majority of FRBs are observed so far. The colour-coded circular disks are repeaters and the grey crosses are non-repeating FRBs.

1.2 Fast Radio Bursts: Progenitors

Different models have been proposed to explain the physical mechanism driving FRBs [4], most of which incorporate white dwarfs, neutron stars, or black holes. These theories can broadly

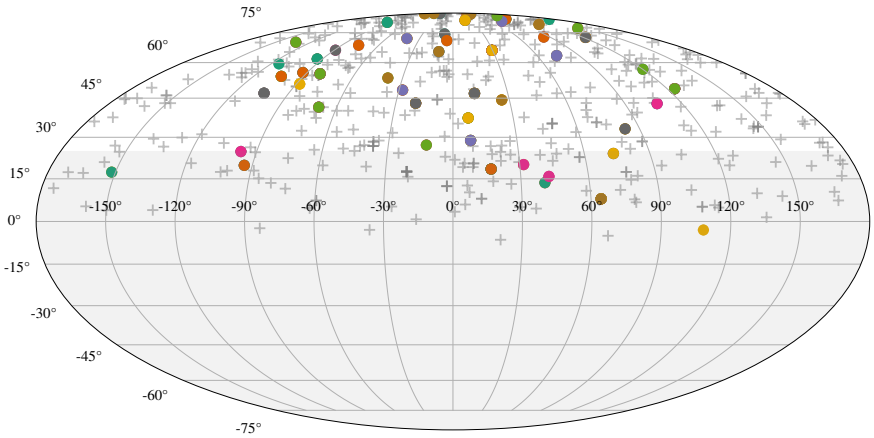

Figure 1.2 Collected FRBs, specifically with CHIME/FRB project so far for the northern hemisphere out of around 600 candidates 30 of them are found to repeat, although these numbers are continuously changing with more incoming data.

be classified into two categories. First, the merger of these compact objects where coherent radio emission is produced at the time of the merger [13–16]. The second category broadly involves mechanisms that do not require any merger event and some physical activity in the compact object can cause the emission of radio waves. Examples of these mechanisms include the curvature radiation mechanism [17, 18], starquake mechanisms such as the crustal activity of a magnetar [19], synchrotron maser emission from relativistic, magnetized shocks [20], giant flares in soft gamma repeaters [21], Gertsenshtein-Zel'dovich effect [22], etc. Detailed reviews of progenitor theories can be found in [4] and [23]. Here is a glimpse into some of the leading contenders. **Magnetars:** These are highly magnetized neutron stars, possessing ultra-strong magnetic fields that are theorized to store immense energy. Sudden reconfigurations within these fields, known as starquakes or giant flares, are hypothesized to be capable of producing the extreme radio luminosities observed in FRBs. **Neutron Star Mergers:** The coalescence of two neutron stars is a violent astrophysical event that releases a tremendous amount of energy across the electromagnetic spectrum. While the peak emission is expected at higher energies (gamma-rays), some models suggest that a portion of this energy could be channelled into an intense radio burst, consistent with the observed properties of FRBs. **Accretion Disks around Stellar-Mass Black Holes:** When matter falls onto a stellar-mass black hole, it forms a hot, rapidly rotating disk of gas known as an accretion disk. Under specific, yet to be fully understood, conditions, this accretion process is theorized to be capable of launching powerful jets that could produce radio emissions similar to FRBs. However, the specific mechanism responsible for generating such extreme bursts within the black hole environment remains an active area of research. **Exotic Phenomena and Unidentified Objects:** The vastness of the

universe might harbour objects beyond our current understanding of physics that could be responsible for FRBs. Hypothetical objects such as cosmic strings or quark stars, with their extreme properties, are proposed as sources of FRBs. However, significant theoretical and observational work is necessary to explore the feasibility of these exotic scenarios.

1.2.1 Compact Object Mergers/Interactions

- **Neutron Star–Neutron Star Mergers/Interactions Magnetic Braking:** The merging of two differentially rotating neutron stars (NSs) generates coherent radiation as the merger spins down due to magnetic braking. This scenario is consistent with the expected FRB rate, but significant mass ejections might render FRBs undetectable. Magnetic Reconnection: During the final stages of inspiral of two NSs, toroidal magnetic field induced by the stars approaching each other can lead to magnetic reconnection. The magnetic reconnection accelerates particles, producing FRBs. Changing Magnetic Flux: The close encounter of two NSs with highly elongated orbits leads to a changing magnetic flux, which bunches particles that radiate coherently. This scenario is also consistent with the observed FRB rate.
- **Neutron Star–Supernova Interactions:** A supernova shock interacts with a NS magnetosphere, sweeping out a magnetospheric tail and triggering reconnection, which produces FRBs.
- **Neutron Star–White Dwarf Mergers:** The rapid rotation of the NS as it accretes matter from the WD, and triggers magnetic reconnection, producing curvature radiation. This model is consistent with repeating FRBs, but the lack of counterparts makes it less testable.
- **Binary White Dwarf Merger:** The merger of two WDs forms a rapidly rotating, magnetized WD. Magnetic reconnection in the polar region injects electrons into the polar region, which accelerate and create curvature radiation.
- **White Dwarf–Black Hole Mergers:** During the merger, a transient accretion disk forms around the BH, producing a high-speed wind and rope-like flux structures. The collision of these structures releases energy, powering FRBs.
- **Neutron Star–Black Hole Mergers:** The NS's magnetic field lines thread around the BH, accelerating charged particles and producing FRBs. The theory predicts a distinct signature with a precursor and a double peak.
- **Pulsar–Black Hole Interactions:** A rapidly spun-up NS near a spinning BH can produce a giant pulse, which is consistent with an FRB.

- **Kerr-Newman–Black Hole Interactions:** Inspiral: A binary BH system with a spinning BH carrying a charge produces an FRB as the magnetic flux changes during inspiral. This scenario is consistent with the observed association of a sGRB with GW 150914. Induced Magnetosphere Collapse: Magnetic instabilities in KNBHs trigger reconnection, producing a curvature radiation consistent with FRBs.

1.2.2 Collapse of Compact Objects

- **Supramassive Neutron Star to Kerr-Newman Black Hole:** The collapse of a magnetized, rotating supramassive NS into a BH could lead to magnetic reconnection outside the event horizon, producing a non-repeating FRB. This model predicts GWs as the primary counterpart.

- **Neutron Star to Quark Star:** The collapse of a NS into a quark star could lead to the emission of a burst of synchrotron radiation, consistent with the observed FRB timescale. This model predicts GWs, X-rays, and γ-ray as possible counterparts.

- **Dark Matter Induced Neutron Star Collapse:** The capture of dark matter particles by an NS could lead to the collapse of the star into a BH, producing an FRB via magnetic reconnection. This model predicts no transient counterparts and a possible X-ray or γ-ray excess.

- **Collapse of Strange Star Crust:** Accretion of matter onto a strange star (SS) could lead to the collapse of its hadronic crust, generating FRB emission through magnetic reconnection. This model predicts no thermal emission counterpart.

1.2.3 Supernovae Remnants

- **Giant Pulses:** Powerful, coherent pulses from rapidly rotating young pulsars or magnetars could explain FRBs. These models predict repeating and stochastic events and a possible SN explosion as a counterpart.

- **Giant Flares in Magnetars:** A giant flare from a magnetar could produce a shock front in its wind nebula, leading to FRB emission. This model predicts repeating FRBs, a possible GRB, a broadband afterglow, and a persistent radio signal as counterparts.

- **Ejecta Penetration:** SN ejecta could be opaque to FRBs, making their penetration and detectability dependent on the age of the ejecta. This model predicts a variable DM with time.

1.2.4 Active Galactic Nuclei

- **AGN Jet Interacting with Cavitons:** Cavitons formed by an AGN jet interacting with surrounding material could lead to the production of pulsed Bremsstrahlung radiation, consistent with FRBs. This model predicts a persistent radio signal as a counterpart.
- **Kerr Black Hole Interacting with AGN:** A KBH surrounded by highly magnetized plasma could be triggered to accrete matter by episodic winds from an AGN, producing FRB emission. This model predicts the possible detection of a SN Type Ib/c explosion, a GRB, and GWs as counterparts.
- **Strange Star Interacting with AGN:** The interaction of a strange star (SS) with an AGN wind could induce torsional oscillation, leading to FRB emission. This model predicts persistent GWs, neutrinos, and γ-ray as possible counterparts.
- **AGN-like Wandering Beams:** A scaled-down version of an AGN jet could produce FRBs by sweeping across an observer's line of sight. This model predicts a persistent radio signal and very soft X-ray or extreme UV emission.

1.2.5 Collisions and Close Encounters

- **Neutron Stars and Small Bodies:** Comet/Asteroid Captured by a NS: The capture of a small body by a NS could lead to the generation of a non-repeating FRB through magnetic reconnection. This model predicts X-ray and γ-ray emission. Pulsar Traveling Through Asteroid Belt: A pulsar passing through an asteroid belt could encounter multiple asteroids, leading to coherent emission. This model predicts a series of bursts, consistent with the repeating nature of FRB 121102. Body Orbiting Pulsar: A body orbiting a pulsar could be influenced by the pulsar wind, leading to coherent emission. This model predicts a periodic emission with one to four peaks.
- **Collisions Between Neutron Stars and Primordial Black Holes:** A primordial black hole (PBH) passing through a NS could lead to magnetic reconnection and a possible repeating FRB. This model predicts GWs as a counterpart.

1.2.6 Interactions Between Axions and Compact Bodies

- **Axion Star and Neutron Star:** An axion star colliding with a NS produces coherent radiation, consistent with FRBs.
- **Axion Star and Black Hole:** An axion star interacting with a BH's accretion disk produces FRBs.

- **Induced Collapse of Axion Clumps by a Highly Magnetic Compact Object:** Axion clumps decay explosively in the magnetic field of a compact object, producing FRBs.
- **Superradiant Axion Cloud and Spinning Black Hole:** A spinning BH with superradiant instabilities produces FRBs from a dense superradiant axion cloud.
- **Axion Quark Nugget and Neutron Star:** An AQN falling through an NS magnetosphere triggers magnetic reconnection and produces FRBs.

1.2.7 Other Models

- **Starquake-Induced Repeaters:** Starquakes in pulsars could be responsible for repeating FRBs, with the event rate and burst energy distribution consistent with FRB 121102. This model predicts a possible association with SGRs.
- **Variable Stars:** Variable stars could produce FRBs through a synchrotron emission process, leading to a variable DM and possibly multiple peaks. This model requires a positive frequency sweep followed by a negative frequency sweep.
- **Lightning in Pulsars:** The discharge of electrostatic energy stored in pulsars could explain FRBs, with the observed variation of burst widths potentially due to pulsar lightning scintillation.
- **Wandering Pulsar Beam:** A wandering pulsar beam could produce FRBs as it sweeps across the observer's line of sight. This model predicts a random walk of the beam.
- **Tiny Electromagnetic Explosions:** The collision of two relativistic superconducting dipoles could lead to a tiny explosion, generating an FRB. This model predicts both repeating and non-repeating FRBs with variable linear polarisation.
- **White Hole Explosions:** The explosion of a white hole, potentially formed from a collapsing Planck star or primordial black hole, could explain FRBs. This model predicts an accompanying infrared and γ-ray signal.
- **Neutron Star Combing:** The combing of a NS magnetosphere by a strong plasma flow could produce FRBs. This model predicts a periodic, variable, and polarized FRB signature with a changing polarisation angle.
- **Neutral Strings:** The decay of cosmic strings could produce FRBs. This model predicts an event rate, timescale, and flux consistent with FRB observations.

- **Superconducting Strings:** Superconducting cosmic strings could produce FRBs through various mechanisms, including string oscillations, collisions of string structures, and the interaction of a current-carrying loop with a galaxy's magnetic field. This model predicts linear polarisation and potential counterparts, such as GRBs, cosmic rays, and neutrinos.
- **Dicke's Superradiance in Galaxies:** The simultaneous transition of a large number of atoms in a galaxy could lead to DSR emission consistent with FRBs. This model predicts a varying time delay and repeating bursts.
- **Alien Light Sails:** Extra-galactic, artificial, beam-powered light sails could be the source of FRBs. However, this model is highly speculative and lacks testability.

1.2.8 Theories That Have Been Ruled Out:

- **Stellar Coronae:** The theory that flare stars produce FRBs has been largely ruled out due to the inability of stellar coronae to produce the required DM and brightness temperature.
- **Annihilating Mini Black Holes:** This theory was ruled out because the inferred distance for the Lorimer burst was incompatible with a galactic origin.

The above catalogue represents a diverse set of models, illustrating the challenges and excitement surrounding the study of FRBs. The ultimate goal is to find the correct model, which will provide a deeper understanding of the physics behind these enigmatic bursts and their potential as cosmological probes. The ongoing search for more FRBs, with precise localisation and multi-wavelength counterparts, will provide crucial constraints to refine and test these models, ultimately guiding us towards a definitive explanation for the origin of these fascinating signals.

1.3 Fast Radio Bursts: As Probes

FRBs hold immense potential as probes of cosmology due to their unique properties and their extragalactic placement. Additionally, their DMs encode information about the total electron content along the line of sight, offering insights into the large-scale structure of the intergalactic medium (IGM) and constraining cosmological parameters. Furthermore, the study of FRB populations across different redshifts can shed light on the evolution of the IGM and star formation rates throughout cosmic history.

1.3.1 Probing Intergalactic medium

Most FRBs seem to be non-repeating (one-off bursts) while some do repeat albeit with no known periodicity. As a result, progenitor theories that predict repeating FRBs seem more promising

because they can explain the apparently one-off bursts, indicating that they may repeat after a long period or we have not yet seen their repetitions, possibly due to selection biases in our observations. Of course, it is possible, even likely, that there are simply multiple classes of FRBs and this work is agnostic on that front. Their unique properties offer compelling advantages for studying IGM [24]: **High Brightness:** FRBs are exceptionally bright radio transients, capable of piercing through the tenuous IGM with minimal attenuation. This allows them to carry information about the intervening medium over vast cosmological distances. **Dispersion Measure:** As an FRB signal propagates through IGM, it interacts with free electrons, causing a delay that is proportional to the electron density along the path. By measuring this delay, known as the DM, scientists can probe the total electron content of IGM along the sightline to the FRB. Spatial Distribution: Studying the statistical distribution of FRBs as a population can reveal information about the large-scale structure and evolution of the IGM. By analysing the variations in DM across different FRBs, scientists can map out the clumpiness and evolution of the electron density within the IGM. **Magnetised IGM:** Some FRBs exhibit RM, which indicates the presence of a magnetised IGM along the propagation path. By measuring RM alongside DM, scientists can gain insights into the magnetic field strength and topology within the IGM, providing a more comprehensive picture of this vast cosmic web.

1.3.2 Host Galaxy Environments and Probing Circumgalactic medium

FRBs are astronomical tools for investigating both their host galaxy environments and the circumgalactic medium (CGM). Due to their extreme brightness and ability to penetrate dense interstellar gas, FRBs offer a powerful tool for studying these regions. **Host Galaxy Environments:** By precisely localising FRBs and studying their host galaxies, we can investigate the stellar populations and physical conditions surrounding the burst. This can shed light on progenitor associations, such as links to massive stars or specific environments within the host galaxy. Additionally, the spatial distribution of FRBs within their host galaxies can reveal clues about the formation and evolution of transients. **Probing the CGM:** The CGM, a vast reservoir of gas and dust surrounding galaxies, remains poorly understood. FRBs act as natural probes as their signals travel through the CGM, experiencing dispersion due to interactions with free electrons. By measuring the DM of FRBs, we can estimate the total electron content along the line of sight. Statistical studies of FRB DMs can provide insights into the average properties and distribution of gas within the CGM, aiding our understanding of galaxy evolution and the interaction between galaxies and their surrounding environments. Therefore, FRBs offer a novel and powerful approach for studying both the immediate surroundings of their host galaxies and the vast, diffuse CGM. By leveraging their unique properties and employing

advanced analysis techniques, we can unlock a new window into the complex ecosystems of galaxies and the interconnected within the cosmic web [25].

1.3.3 Milkyway and Interstellar Medium, Halo

FRBs are powerful probes of the ISM and galactic structures. Their high brightness and ability to travel through vast distances make them unique tools for studying the Milky Way and its environment: **Mapping the Milky Way ISM:** FRB DMs – a measure of the total electron content along the path – can be used to map the distribution of free electrons within the Milky Way's ISM. By analysing the statistical properties of FRB DMs, we can create three-dimensional maps of electron density variations, revealing the structure and evolution of the interstellar medium within our galaxy. Probing the Galactic Halo: Due to their extragalactic origins, FRBs can act as probes of the Milky Way's halo [26], a vast region of hot, diffuse gas surrounding the galactic disk. As FRB signals traverse the halo, they interact with this gas, revealing its properties like temperature, density, and magnetic field distribution. Studying RMs of FRBs – a measure of the rotation experienced by the polarisation plane due to the halo's magnetic field – can provide valuable insights into the magneto-ionic environment within the galactic halo. Interstellar Medium Studies: FRBs can also be used to study the properties of the ISM between galaxies. Observations of repeating FRBs, where the source location is known, allow scientists to measure the contribution of IGM to the total dispersion. By comparing this value to the Milky Way's ISM contribution (derived from the DM), we can estimate the electron density and structure of the IGM along the line of sight.

1.4 Fast Radio Bursts: Tests of Cosmology

As FRBs are spaced at the cosmological distances, they hold the capacity to probe the large-scale structure and cosmic web as DM contains imprints of electron column density. Measuring DM of FRBs, which quantifies the total electron density along their path maps the distribution of baryonic matter along the line of sight. Additionally, the arrival time delays of FRBs due to gravitational lensing by massive objects like galaxies can provide valuable information about the distribution of dark matter. This information complements other cosmological probes, offering a unique perspective on the structure and evolution.

1.4.1 Cosmic Re-ionisation

The information from FRBs provides crucial insights into the re-ionization epoch, the period when the universe transitioned from a mostly neutral state to its current ionized state. With a large number of high DM FRBs, and their interaction with the ionized gas (plasma) within galaxies and the IGM various techniques have developed for probing ionization history. Due to finite ionised gas less than the redshift of 15 maximum DM contribution from IGM is constant.

Therefore, the maximum observable DM measured for the FRBs at the high redshifts (> 6) probes Hydrogen-reionization. Another method is to put constraints based on FRB population rate per DM as this quantity depends on reionisation history with an assumption that the FRBs follow the Star Formation Rate (SFR). The third method is dependent on a small number of accurate measurements FRB redshifts with $z > 6$ during reionization epoch [27]. Simulations for measuring Helium reionisation are explored with DM–z relation of FRBs in redshifts on 3–4 with models of He-re-ionisation at redshifts of 3 and 6 [28].

1.4.2 Dark Energy Equation of State and Curvature Density parameter

The FRBs hold promise as radio probes of cosmology when combined with different surveys. The DM–z relation can be utilised to constrain parameters such as curvature parameter, Ω_k and dark energy equation of state [29]. For that the cosmic DM–z relation is realised as;

$$\langle \mathrm{DM_{IGM}}(z_\mathrm{S}) \rangle = \frac{3cH_0\Omega_\mathrm{b}}{8\pi G m_\mathrm{p}} \int_0^{z_\mathrm{S}} \frac{f_\mathrm{IGM}(z)\chi(z)(1+z)}{\sqrt{\Omega_\mathrm{m}\,(1+z)^3 + f(z)\Omega_\mathrm{DE} + \Omega_\mathrm{k}\,(1+z)^2}}\,\mathrm{d}z\,, \tag{1.6}$$

here along with regular physical constants, $f_\mathrm{IGM}(z)$ is a fraction of galactic feedback, $\chi(z)$ is ionisation fraction as a function of redshift and the dark energy equation of state $f(z)$ is given by,

$$f(z) = exp\left[3\int_0^z \frac{(1+w(z'')\,\mathrm{d}z''}{(1+z'')}\right], \tag{1.7}$$

Further, the specific case of equation of state $w(z)$ is as follows,

$$w(z) = w_0 + w_a \frac{z}{(1+z)} \tag{1.8}$$

Statistical studies of FRB populations can further constrain the dark energy equation of state allowing tests of the ΛCDM model. By leveraging Markov Chain Monte Carlo Simulations (MCMC) methods, simulated FRBs have forecast constraints on these cosmological parameters independent from existing constraints with Supernovae measurements, galaxy surveys and measurements of BAOs. FRB properties and their large-scale distribution, FRBs offer a powerful and independent approach to unravelling the mysteries of dark energy and baryon content in the universe.

1.4.3 Baryon Density and Hubble parameter

The DM, coupled with redshift information, allows for direct measurement of the baryon density (Ω_b) [30]. Additionally, fixing Dark energy equation of states in Equation (1.6) as

Ω_Λ, estimates of the Hubble constant is given by [31–34]. The estimations of the Hubble constant are extremely sensitive to accurate measurements of redshift and host galaxy DM contributions. The current estimates of the Hubble constant with FRBs agree with the late-time universe measurements. These constraints will be further refined as more localised FRBs will be available with future radio telescopes.

1.4.4 Millicharged Dark Matter and Neutrinos

Models for the millicharge and axion-like dark matter can be constrained by FRBs. Currently, magnetar-like radio bursts are predicted to emit neutrinos and hence a potential multi-messenger observable for FRBs.**Millicharge Dark Matter:** If dark matter consists of weakly charged particles, they contribute to the dispersion delays of FRBs. This dispersion delay will be proportional to ϵ/m_{milli}, the fractional charge of dark matter (DMa) particles and the mass of DMa. Based on measurements of FRB121102, current bounds are of the order of $10^{-14} - 10^{-11}$ for the mass range $10^{-23} - 10^{-20}$ eV [35]. **Neutrino-Photon Interactions:** In the presence of extremely high energies such as FRBs can be a precursor of neutrino emissions from magnetar-like progenitor. Observing these interactions in the vicinity of FRBs could provide a novel way to study neutrino properties and constrain their masses.

1.4.5 Tests of relativity: Photon mass, Weak Equivalence Principle and Lorentz Invariance

Allowing photon mass to vary in Equation (1.6) with ΛCDM as prior will strengthen bounds on photon mass. **Photon Mass:** A massive photon would exhibit dispersion in the ISM that is distinct from the dispersion caused by free electrons. However, the current uncertainties in FRB distances and the inherent dispersion within the ISM make it challenging to definitively detect a mass-induced signature. Future accurate measurements and understanding of FRBs and their properties will help directly in probing relativity concepts such as Weak Equivalence Principle (WEP), and Lorentz Invariance Violation (LIV) [36]. **Weak Equivalence Principle (WEP):** WEP postulates that all objects, regardless of mass or composition, experience the same acceleration in a gravitational field. Shapiro delay-based tests of WEP with low DM FRBs typically < 1, if used to probe WEP violations, would require extremely precise measurements of their arrival times and redshifts, which are currently beyond our observational capabilities. **Violations of Lorentz Invariance Principle (LIV):** LIV implies a violation of Lorentz symmetry, a cornerstone of special relativity. Utilising FRBs to constrain LIV effects demands high-precision measurements of their dispersion and arrival times across a wide range of redshifts as well as a change in polarisation arising from vacuum birefringence. However,

limitations in telescope sensitivity and source identification make achieving such precision difficult.

Observations of distance, source luminosity, flux density at various DMs, and brightness temperature inform physical constraints on FRBs. DM can be separated into contributions from the host galaxy, Milky Way, and IGM. Assuming a uniform IGM, DM yields redshift and luminosity distance, enabling estimation of source luminosity limits. Similar to pulsars, FRB brightness temperature is derived from pulse width, peak flux density, luminosity distance, and observed frequency.

1.5 Summary

The thesis attempts to work on a few of the above topics. In Chapter 2 we explore statistics and quantifiable capabilities of FRBs with an upcoming survey telescope called Hydrogen Intensity and Real-time Analysis eXperiment (HIRAX), In Chapter 5 we understand MeerKAT FRB and single pulse processing pipeline and explore an algorithm to preprocess data features and improve the state of the art machine learning model for the telescope. In Chapter 3 we shift gears and explore the possibility of detecting primordial black hole (PBH) fractions using FRBs as probes. Chapter 4 attempts to answer with limited noisy data such as the CHIME/FRB survey, how to identify repeaters from apparent non-repeaters.

2

Hydrogen Intensity and Real-Time Analysis eXperiment (HIRAX) Telescope FRB pipeline

This chapter presents a review of the current instrumentation status of the HIRAX telescope, drawing upon established literature [37, 38]. We delve into the instrument's sensitivity and field of view, followed by an in-depth analysis of FRB rate calculations. The latter half of the chapter focuses on the proposed FRB detection pipeline for HIRAX. In particular, we address the aspect of temperature monitoring for the pipeline's GPU components. We elaborate on a temperature monitoring model incorporated within the `ketkan` pipeline, examining its effectiveness across various processing speeds.

2.1 Scientific motivation for HIRAX

Following the establishment of gravity through the Einstein Field Equations, a cosmological model for the large-scale universe was formulated based on the assumptions of [39]. This initial static model incorporated a cosmological constant to counteract solutions suggesting an expanding universe. However, subsequent theoretical arguments for a non-static universe emerged [40, 41], and Hubble's observations provided the first observational evidence for expansion [42]. The static universe models were definitively discarded after independent observations of the Cosmic Microwave Background (CMB) radiation [43, 44]. Finally, in the late 1990s, studies comparing local Type Ia supernovae with those at higher redshifts ($z \approx 0.5$) revealed a discrepancy. Supernovae at higher redshifts were fainter than expected in a universe dominated by matter ($\Omega_{\mathrm{m}} \approx 0.2$), exhibiting a dimming of about 0.2 magnitudes [45, 46]. This unexpected observation provided the foundation for the concept of dark energy, a mysterious repulsive force responsible for the accelerating expansion of the universe.

Thus, one of the unanswered questions in modern-day cosmology is the accelerated expansion of the universe and measurements of precise cosmological distances to chronologically mark events in the expansion history. Theoretically, cosmic distances are estimated based on the Friedmann equations but have ΛCDM model as prior. Observational measurements of distances estimated from parallax, dispersion measures of transients and spectroscopic are model-independent tools but are limited by telescope instrument limitations. Specifically, the faint objects far away, typically $z > 5$ are difficult to observe because of telescope sensitivity limits.

Unlike these observational distances or cosmic ladders, Baryon Acoustic Oscillations (BAOs) are acoustic ripples in space-time and hence echoed upon matter distribution over redshift ranges [47]. Therefore measurements of BAO distances do not get affected by relative motions of the Earth. Such **standard scalars** have been measured for an early universe with CMB measurements and for a late universe with Baryon Oscillation Spectroscopic Survey (BOSS) [48], Dark Energy Survey (DES) [49]. HIRAX aims to detect these oscillations by measuring matter distributions with intensity mapping in a neutral hydrogen gas-dominated era. The HIRAX will be a complementary measurement specific to redshifts between **0.775 to 2.55**. Correlating measurements of HIRAX with new surveys such as Euclid [50] will provide precise measurements of BAOs. In addition to detecting BAO signatures experiments such as HIRAX, because of their large Field of View (FoV) are excellent **radio transient search** instruments in the frequency range of 400 MHz to 800 MHz.

2.2 Radio Interferometry and Aperture Synthesis

Radio interferometry is a powerful technique that utilises an array of radio antennas functioning as a single, much larger telescope. Unlike a traditional dish telescope, the antennas within the array are separated by significant distances, ranging from meters to kilometres or even continents. The key principle lies in exploiting the subtle phase differences that arise when radio waves from the same astronomical source arrive at each antenna. These phase differences, meticulously measured and analysed, provide information equivalent to that collected by a telescope with a diameter equal to the maximum separation between the antennas in the array. The van Cittert-Zernike theorem [51] relates the spatial coherence function received by the antenna array to the distribution of intensity in the sky of the incoming radiation. It shows that the spatial correlation function of the received signal V(r1, r2) depends only on $\mathrm{r1} - \mathrm{r2}$ and that if all the measurements are in a plane, then the intensity is a Fourier transform of signal V.

$$V(r1, r2) = \mathcal{F}\{I(s)\} \tag{2.1}$$

where $\mathcal{F}$ implies taking the Fourier transform. Let us assume that the source is distant and can be approximated as a brightness distribution on the celestial sphere of radius R (see Figure 2.2). Let the electric field at a point $P_1'(x_1', y_1', z'1)$ at the source be given by $E(P_1')$. The field $\mathcal{E}(P_1)$ at the observation point $P_1(x_1, y_1, z_1)$ is given by,

$$E(P_1) = \int \mathcal{E}(P_1') \frac{e^{-ikD(P_1,P_1')}}{D(P_1, P_1')} \mathrm{d}\Omega_1, \tag{2.2}$$

where $D(P_1', P1)$ is the distance between P_1' and P_1. Similarly, if $E(P_2)$ is the field at some other observing point $P_2(x_2, y_2, z_2)$. The spatial correlation function $\langle E(P_1) * E(P_2) \rangle$ is also referred to as the "visibility" $V(u, v, w)$.

$$V(u, v, w) = \int \mathcal{I}(l, m) e^{-i2\pi[lu+mv+nw]} \frac{\mathrm{d}l\mathrm{d}m}{\sqrt{1 - l^2 - m^2}}, \tag{2.3}$$

where $\mathcal{I}$ is the intensity at the point P_1'. And (l, m, n) are called "direction cosines". It can be easily shown that $l_2 + m_2 + n_2 = 1$ and that $\mathrm{d}\Omega = \frac{\mathrm{d}l\,\mathrm{d}m}{\sqrt{1-l^2-m^2}}$.

This fundamental relationship between the visibility and the source intensity distribution is the basis of radio interferometry. In the optical literature, this relationship is also referred to as the Van Cittert-Zernike theorem. Combining signals from an array of radio antennas effectively creates a virtual telescope with a diameter equal to the maximum separation between the antennas. This technique relies on interferometry principles explained above, where the radio waves from an object arriving at different antennae are overlapped or interfered with, to create a fringe pattern. The detailed analysis of these fringes and the Earth's rotation that changes the baseline lengths between antennae allows a reconstruction of a high-resolution image of the radio source. This approach enables the study of faint and intricate structures in astronomical objects, providing invaluable insights into their formation and evolution.

2.3 Correlators in Radio Astronomy

The correlation of signals from multiple antennas is an indispensable technique for achieving high angular resolution, surpassing the limitations of single-dish telescopes. The process of correlation involves combining the signals from different antennas to extract the phase information of the incoming radio waves, which ultimately unveils the spatial structure of celestial sources. Among various correlator architectures, the FX correlator stands out as a highly efficient and powerful tool, particularly for applications in Very Long Baseline Interferometry (VLBI) [52]. The FX correlator, as its name suggests, operates in the frequency-time (FX) domain, departing from the conventional time-lag (Lag) correlator approach. It leverages the Fast Fourier Transform (FFT) to perform a spectral analysis of the signals received from each antenna. This spectral representation allows for efficient and accurate manipulation

of the phase information across the entire frequency band. The key advantage of the FX correlator lies in its ability to handle a vast number of input signals, making it ideal for VLBI, where arrays of antennas spread across vast distances are involved.

The FX correlator operates in a three-stage process. The first stage involves transforming the time-domain signal from each antenna into the frequency domain using the FFT. This process effectively converts the signal into a spectral representation, providing a detailed snapshot of the signal across different frequencies. In the second stage, the frequency spectra from all antennas are cross-multiplied. This cross-multiplication operation creates the correlation function, which encapsulates the phase information between the signals received from different antennas. The correlation function ultimately represents the spatial distribution of the radio source being observed. The final stage involves transforming the correlation function back into the time domain through an inverse FFT. This step produces the final output, a series of time-domain correlations that correspond to different spatial locations in the sky. These correlations are then used to synthesize an image of the radio source, revealing its structure and morphology with unprecedented detail.

One of the major advantages of the FX correlator is its inherent flexibility and scalability. It can be easily adapted to accommodate a wide range of observational configurations, including varying numbers of antennas, different antenna spacings, and various bandwidths. The modular design of the FX correlator allows for the incorporation of new antennas or the expansion of the array without significant re-engineering. Another key advantage is its efficiency in terms of computational speed and processing time. The use of the FFT enables a significant reduction in the number of multiplications required for correlation, compared to traditional time-lag correlator architectures. This efficiency translates into shorter processing times, allowing for faster data reduction and analysis. In addition to its efficiency, the FX correlator exhibits remarkable accuracy in its ability to preserve the phase information across the entire frequency band. The spectral representation employed in the FX correlator minimizes the impact of errors introduced by imperfect timing or other imperfections in the data acquisition process. This precision is crucial for high-resolution imaging, especially when dealing with VLBI observations where the distances between antennas are vast.

2.4 HIRAX Telescope Overview

The 21 cm signals from the neutral hydrogen are optically thin and are used for tomographic measurements of large comoving gas volumes over cosmological scales. Therefore they are statistically different from the foreground signals. To acquire such signals from the southern hemisphere, HIRAX will be situated in the Karoo desert located near the Square Kilometer Array (SKA) site in South Africa. The telescope will observe in transit mode and, therefore not

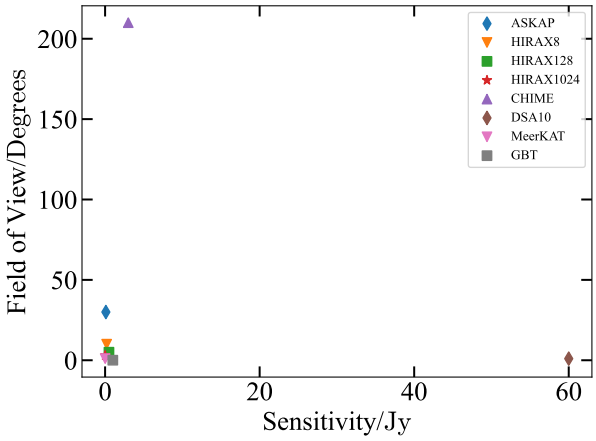

Figure 2.1 Comparison of HIRAX FoV and sensitivity with FRB search telescopes, HIRAX provides better sensitivity than CHIME by compromising FoV with accurate localisation. HIRAX-8 gives comparative performance to DSA-10, MeerKAT and GBT.

have a pointing system. This type of interferometer finds application in the 21 cm intensity by trading off tracking a source in the sky. To cover signals for redshifts between 0.775 to 2.55 operational frequency range for the instrument is **400 to 800 MHz**.

The receiver system for the HIRAX instrument is modelled as a low noise amplification system followed by filtering systems to select the bandwidth of interest. The resulting interferometric outputs are used to generate fringes computationally. These fringes - complex visibilities are energy per unit frequency and in the 21 cm cosmology converted to the units of temperature for ease of comparison. The beam of the interferometer is calibrated/normalised - the sky is assumed to have a uniform brightness temperature which is a valid assumption of a large field of view receivers. The signal establishes the sensitivity of the radio interferometer to noise (SNR) ratio. The sensitivity of the radio telescope is determined by the following equation

$$\sigma_K = \frac{T_{\text{sys}}}{\sqrt{N_{\text{dish}}}} \times \delta\nu \times \Delta t, \tag{2.4}$$

where T_sys system temperature which can be converted to Jy and represented as

$$\left[\frac{\text{T}}{\text{Jy}}\right] = 10^{-26} \times \frac{A_e}{2k}. \tag{2.5}$$

Figure 2.1 projects FoV and sensitivity of different radio telescopes. HIRAX provides sensitivity comparable to radio telescopes such as ASKAP and therefore an ideal telescope for FRB searches and localisation. Moreover, the outriggers will add to the sensitivity described in the figure when combined with the main array.

The final HIRAX instrument will be 1024 6-m solid $f/0.23$, dishes with $400 - 800\,\mathrm{MHz}$ clover-leaf feeds at focus with dual-polarization antennae. The instrument instantaneous Field of view (FoV) is $15000\,\mathrm{deg}^2$. Its single antenna beam resolution is 300 degrees [53] but combined beam response measurements are underway. Signals are amplified using receivers with noise temperature below 50K and are bandlimited to $400 - 800\,\mathrm{MHz}$. At Analoguge to Digital Converters (ADCs), They are sampled at 800 MSPS. The system specifications are motivated by capturing 21 cm signals with an angular line-of-sight resolution to measure BAOs. At lower frequencies, the signal faces subsequent RFI from the terrestrial radio transmissions and these signals are removed from the system by RFI mitigation techniques. The BAO signals can be resolved with the current FoV at the line of sight to $\sim 11\,\mathrm{Mpc}$ at a redshift of 0.775 (800 MHz) and $\sim 45\,\mathrm{Mpc}$ at the redshift 2.55 (400 MHz) with HIRAX. Frequency separation derived from the required spatial scale for BAO is $\sim 3.5\,\mathrm{MHz}$ at the redshift of 800 MHz and around 2.2 MHz at the redshift of 2.5 (400 MHz). Because of 1024 frequency channels for the 400 to 800 MHz range, the frequency resolution comes around 0.4 MHz wide. The minimum temperature of neutral hydrogen at the redshifts of interest is around 320 μK. The fluctuations in this temperature are expected to be around 100 μK. For HIRAX, therefore, the observation per unit sky area is approximately 35 hours with frequency separation around 2 MHz and system temperature around 50 K.

To aid in better localisation, with proposed outriggers in the distant part of South Africa, the HIRAX FRB pipeline will include long baseline interferometry in real-time enabling voltage dump for the FRB detection window. HIRAX array with the outrigger is planned at Durban and HartRAO. Localisation of the extragalactic FRBs is a challenging task for the widefield survey with radio telescopes. Therefore, the planned focus is on FRB localisation with outriggers along with a direct imaging correlator for the upcoming HIRAX 8-element prototype and subsequently, HIRAX 256-element pathfinder, at the radio-quiet SKA site in the Karoo desert.

In conclusion, the HIRAX system is a wide field of view interferometer with FX correlator and calibration system used in three applications: 21 cm mapping, FRB pipeline and pulsar backend. The CHIME system deployment and calibration are being tested in stages for system stability for the HIRAX instrument as well.

2.5 FRBs detection rate with HIRAX

The effective detection rate of any object is extrapolated empirically from telescope FoV and several detected sources for given flux/fluence limits [54]. Although in gamma-ray astronomy [55] generally the number of sources is given by the following equation

$$N(>S) = \frac{\Omega T}{4\pi} \int_0^{z(L_{\max},S)} \int_{L_{\min}(z,S)}^{L_{\max}} \Phi(L,z) \frac{\Psi(z)}{1+z} \frac{\mathrm{d}V}{\mathrm{d}z}\, \mathrm{d}L\, \mathrm{d}z\,, \tag{2.6}$$

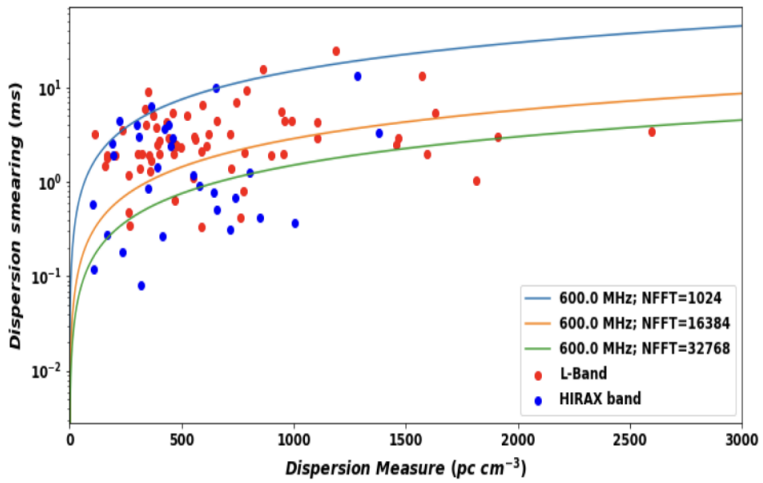

Figure 2.2 Dispersion smearing/delay(ms) vs Dispersion Measure, blue dots are FRBs that fall in HIRAX band (400 - 800 MHz) and red dots are L-band FRBs. solid curves give smearing limits for dispersion for different channel resolutions and centre frequencies of HIRAX. 32k frequency channels provide resistance against dispersion smearing.

where N is the number of detected sources, Ω and T are system FoV and Temperature. $\Phi(L, z)$ is GRB formation rate, and $\Psi(z)$ is luminosity function. Finally, $\mathrm{d}V/\mathrm{d}z$ is the comoving volume with respect to redshifts. this equation can be adapted in FRB astronomy [56] as follows:

$$R_k = R_l \frac{\Omega_k}{\Omega_l} \left(\frac{\mathrm{SEFD}_l}{\mathrm{SEFD}_k} \sqrt{\frac{B_k n_{p,k}}{B_l n_{p,l}}} \right)^{\alpha}. \tag{2.7}$$

The rates are divided between two frequency bands and Ωs are FoVs for those bands. SEFD_k is flux density, B_k is bandwidth and $n_{p,k}$ is number of polarisations. For current estimations α is taken as $3/2 R_l$ is known and R_k is derived from Equation (2.7). The HIRAX is predicted to detect a few hundred FRBs per unit solid angle per day (Figure 2.2). In this regard, it has been proposed to develop a pipeline capable of detecting FRBs at various DMs in real-time. For Figure 2.3, we follow [57] as described in Equation (2.8), where survey with the known rate is taken as Parkes survey and all the calculations are done with uniform FRB source distribution with Euclidean sky

$$\mathcal{N}(> F_{\mathrm{obs}}) = \frac{1.2 \times 10^4}{4\pi} \left(\frac{F_{\mathrm{obs}}}{1.8\,\mathrm{Jy\,ms}} \right)^{-\alpha} \mathrm{sr}^{-1}\,\mathrm{day}^{-1}. \tag{2.8}$$

Figure 2.2 shows the minimum time resolution needed for the HIRAX receiver to detect FRBs at dispersion measures below three thousand parsecs per cc, at the centre frequency of HIRAX (600 MHz) with different Fast Fourier Transform (FFT) channel widths. It shows dispersion smearing as a function of dispersion measure for different observing frequencies and FFT sizes. The dispersion smearing increases with increasing dispersion measure. This is because the interstellar medium slows down the radio waves, and the amount of slowing down depends on the frequency of the radiation. The higher the frequency, the less the slowing down. This means that the dispersion smearing is greater for lower frequencies. The dispersion smearing increases with increasing FFT size. This is because a larger FFT size means that the data is being sampled at a higher rate, and this results in a finer time resolution. This means that the dispersion smearing is greater for larger FFT sizes. The different coloured lines in the figure represent different observing frequencies and FFT sizes. The red dots represent the dispersion smearing of pulsars observed in the L-band, while the blue dots represent the dispersion smearing of pulsars observed in the HIRAX band. Figure 2.2 shows that the HIRAX band has a lower dispersion smearing than the L-band. This is because the HIRAX band has a higher frequency than the L-band. The dispersion smearing is greater for larger FFT sizes. This is because a larger FFT size means that the data is being sampled at a higher rate, and this results in a finer time resolution. This means that the dispersion smearing is greater for larger FFT sizes. For HIRAX, dispersion smearing is a function of both the dispersion measure and the observing frequency and FFT size. The HIRAX band has a lower dispersion smearing than the L-band, and the dispersion smearing is greater for larger FFT sizes. It is seen that HIRAX will require more than a thousand channels at its centre frequency to efficiently detect FRB pulses and characterise its dispersion measure. The wider beamwidth of HIRAX facilitates a survey of large areas of the southern hemisphere. With current estimates, HIRAX is expected to detect a few hundred bursts daily with 256 elements on average.

The plot in Figure 2.3 shows the expected number of FRBs that can be detected by the HIRAX telescope, as a function of the fluence of the FRBs. The plot compares the sensitivity of the telescope for both coherent and incoherent beams. Coherent beams are computationally more expensive to process, but they provide higher sensitivity, meaning the telescope can detect fainter FRBs. This is because coherent beams focus the energy from the FRBs onto a smaller area, increasing the signal-to-noise ratio. The plot shows that the incoherent beam sensitivity is much lower than the coherent beam sensitivity for the same fluence. This means that a coherent beam configuration can detect more FRBs than an incoherent beam configuration, even though it is more computationally expensive.

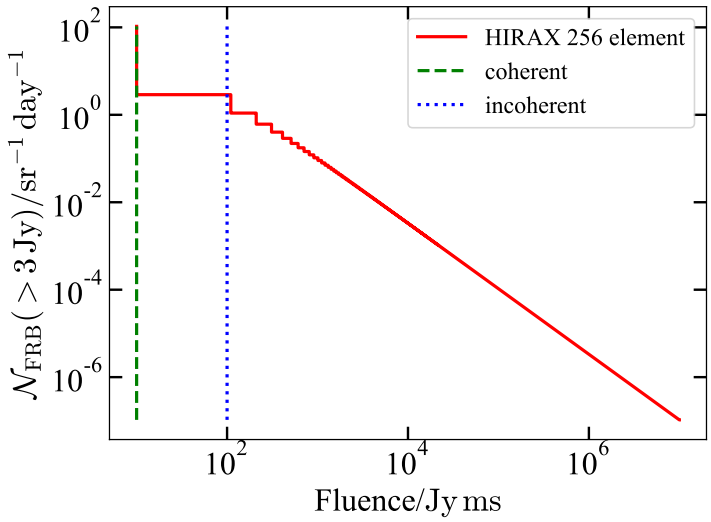

Figure 2.3 Expected number of FRB with HIRAX 256-elements. We show flux cutoff/telescope sensitivity for incoherent and coherent beam sets of FRBs. Even though computationally expansive, coherent beam configuration provides higher sensitivity of telescope

2.6 Lensing FRB Rates Over Redshifts for HIRAX

In the next Chapter, we discuss constraints on the fraction of primordial black holes with gravitational lensing of FRBs. Here, we discuss detection prospects of lensed FRBs with HIRAX/FRB receiver search over a range of redshifts. We calculate some lensed FRBs over redshift considering lensing sources happen to be in the travelling path over the year. We follow [56] for our FRB lensing rate detection for the HIRAX. Microlensing sources such as massive compact halo objects, primordial black holes, stars and free-floating planets, lensing from heavier objects such as intermediate-mass black holes and dark matter haloes, galaxy lensing at larger distances and galaxy clusters.

Assuming a uniform distribution of lensing sources and FRBs over the sky we predict that lensing events detected by HIRAX will be around one per year and are comparable with that of CHORD an upgrade of CHIME. In this analysis, we have included an upgraded CHIME instrument, The Canadian Hydrogen Observatory and Radio-transient Detector (CHORD) [58]. Although a higher number of FRBs, CHIME will not be able to probe distant FRBs because of telescope sensitivity, however, HIRAX and CHORD will be able to find a few FRBs between redshifts of 2 to 3.

The Figure 2.4 shows the distribution of FRBs over redshift for different telescopes: CHIME, CHORD (an upgrade of CHIME), and HIRAX. The plot shows that HIRAX can detect a comparable number of lensed FRBs (those that are gravitationally lensed by galaxies or

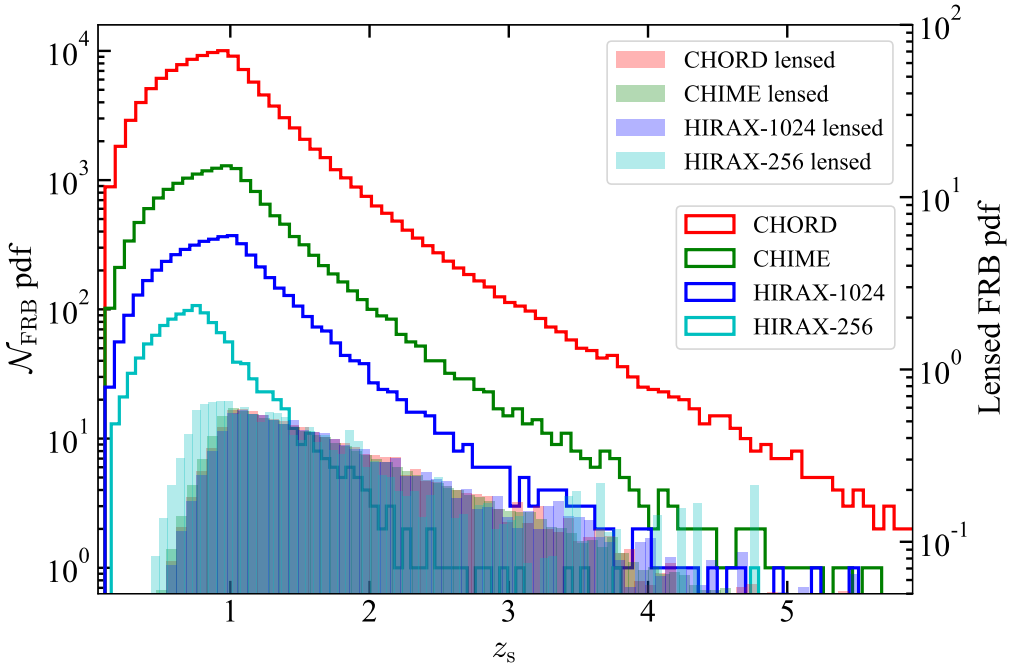

Figure 2.4 Distribution of FRBs over redshifts: We compared here three telescopes CHIME, an upgrade of CHIME called CHORD and HIRAX. HIRAX gives a competitive number of lensed FRBs with that of CHORD.

clusters) as CHORD. This is significant because lensed FRBs can help us study the distribution of matter in the universe. The plot also shows that HIRAX has a different distribution of FRBs than CHIME, suggesting that HIRAX is sensitive to a different population of FRBs. This suggests that HIRAX may be able to make significant contributions to our understanding of FRBs.

2.7 Proposed FRBs detection pipeline with HIRAX

Crudely, Radio Frequency (RF) bandpass filters are used to band limit the signals received at the HIRAX dual-band dual-polarisation feeds. And are amplified using room temperature with noise performance below 50 K. HIRAX uses the Fourier Transform-Multiplication (FX) engine to generate time-frequency plots. These signals are then averaged over a few time samples to increase signal strength and save disk space in the data allocation system. For modern digital FX correlators, signals are digitised with 800 MSPS and 8 bits, and the bandwidth is divided into 1024 channels of resolution 0.4 MHz. This data from the F-engine is then sent to the X-engine for spectra generation (cosmology pipeline), FFT beamforming and up-channelization (FRB backend) and Tied-array beamforming (pulsar and FRB timing backend). The Analog front-end for the HIRAX receiver employs a low noise amplifier for the early amplification of

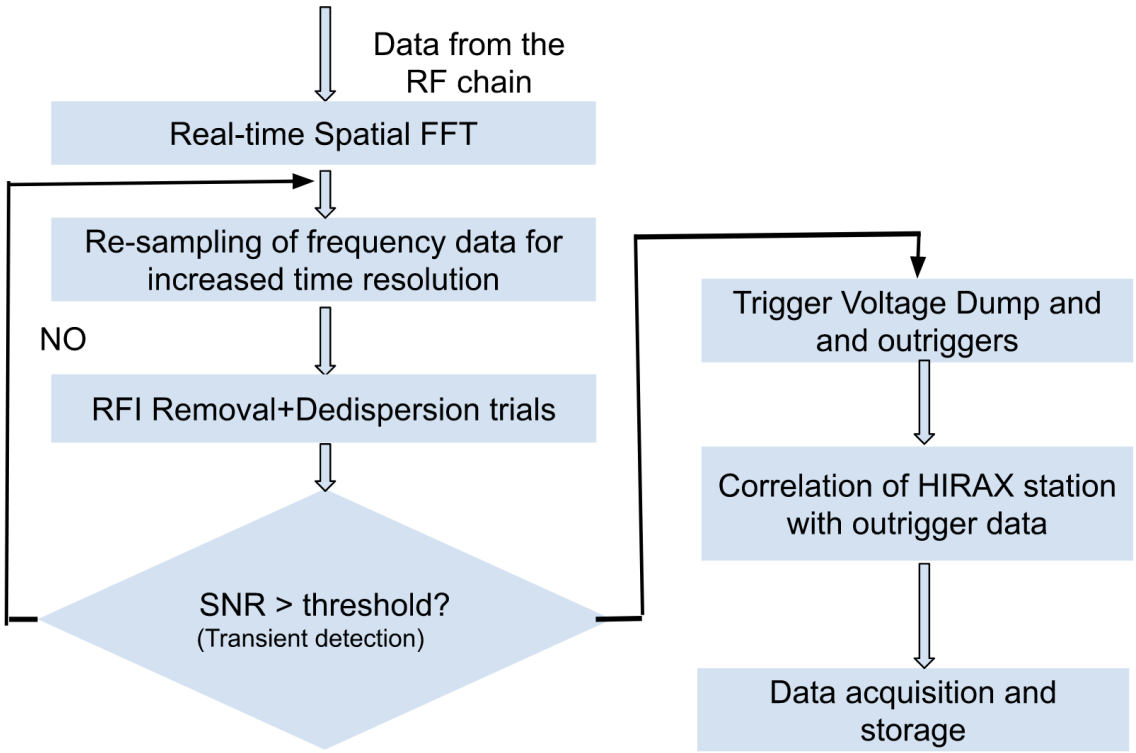

Figure 2.5 Correlator pipeline for HIRAX FRB: Data from the RF chain is received form and FFT is taken of the data, we resample the data for increased time resolution and algorithms for RF removal and dedispersion are applied. After dedispersion, if the signal is of higher flux/SNR, typically above 10, voltage data is saved to the system and outriggers are notified for the possible transient event. After that, correlation process is done at the HIRAX station and data is saved to a drive afterwards.

$\sim$ 40 dB [53], followed by low attenuation coaxial cable of 50 m with an attenuation of -4 -6 dB. The signal is bandlimited to 400 to 800 MHz with 30 to 36 dB amplification in the receiver hut. The signal is then sampled in time and quantised in amplitude.

The F-engine is comprised of a custom-made system called ICE motherboards for sampling and digitising signals. One ICE board digitises ten analogue inputs at 800 MSPS with 8 bits. The bandlimited sky signals are directly sampled using the second Nyquist zone. Each piece of information is then fed to a custom Polyphase Filter Bank (PFB) that splits the 400 MHz bandwidth into 1024 frequency bins 390 kHz wide. The corner turn operation is performed in four stages; the last stage is completed in the X-engine cluster. An output correlation matrix is a +4-byte real and +4-byte imaginary complex value.

Digitisation of the signal introduces the quantisation noise as the amplitude is encoded in the finite set of discrete values. These quantisation effects need to be addressed at 8-bit digitisation of the analogue signals, computation of FFT and data reduction after the channelisation stage. The frequency resolution receiver gains are adjusted to utilise ADC's entire dynamic range (3.5 bits RMS) to minimise quantisation noise at the 8-bit digitiser. To minimise signal-to-quantisation noise ratio in the FFT stage, the results are because of the round of errors in the FFT calculations. The scaling of FFT output is done in stages in Field Programmable Gate Array (FPGA) register shifting operations to prevent overflow. To ensure the signal is not lost in 4×4 bit data reduction after channelisation, the frequency data is adjusted for high precision (35+35 bits) and gain (k bits) and selecting 4-bit MSB.

Quantisation bias in digital correlators is introduced because of the truncation of the amplitude of the signals. The quantisation error is always real in the complex-valued quantiser with circularly symmetric Gaussian input. This error is negative when the quantisation levels are odd and positive when quantisation levels are even for the low-level signals. If both inputs to the correlator are optimally quantised, the magnitude of quantisation effects in the correlator's output signal is minimal. The quantisation phase error is negligible when either input signals are optimally quantised or both input signals are uncorrelated. With a correlator like CHIME, quantisation is insignificant as the analogue signal is dominated by receiver noise.

With the receiver system described above we note that mapping the 21 cm universe with the HIRAX involves taking into account the curvatures of the sky because of the interferometer's enormous field of view. For comparatively small FoV scenarios, the sky can be assumed to be flat. The visibility can be considered the 2D Fourier transform of the sky to analyse transit radio telescopes in the spherical harmonic domain m-mode analysis. The sky data's m-mode formalism allows an efficient method to separate the 21 cm signal from the foreground. The well-calibrated instrument provides better foreground modelling for extracting a 21 cm signal from the received data. CHIME employs three calibration strategies: Beam characterisation, receiver gain calibration, and digital calibration. The receiver calibration and thermal stabilisation environment of the analogue receiver is controlled by hosting it in a temperature-controlled chamber. To precisely characterise variations in receiver gain in real-time, a broadband injection calibration scheme is employed for tracking jitter in the F-engine.

2.8 Temperature Measurement Module in kotekan

Graphical processing Units (GPUs) rely on a delicate balance between performance and temperature. To handle demanding tasks, GPUs run at high clock speeds, but this inevitably generates heat. As the GPU temperature climbs, it nears a critical point known as the thermal throttling threshold. To safeguard against overheating and potential damage, the GPU automatically

reduces its clock speed at this point. This translates to a direct performance hit, limiting the number of instructions processed per second. For optimal GPU performance, it's crucial to maintain a safe operating temperature. Techniques like adjusting fan curves or undervolting can help strike a balance between thermals and performance. Conversely, robust cooling solutions allow for sustained higher clock speeds, maximizing performance potential. Therefore, understanding the interplay between temperature and frequency is essential to optimise GPU performance and ensure its long-term health.

Due to their compact design and intense processing power, GPUs generate significant heat. This heat can negatively impact performance and lifespan in several ways. Firstly, excessive temperatures can trigger throttling, a mechanism that reduces processing speed to prevent overheating and potential damage. Temperature monitoring allows users to identify potential throttling and adjust settings like clock speed or fan control to maintain optimal performance. Secondly, high operating temperatures accelerate component degradation, shortening the lifespan of the GPU. By monitoring temperature, users can identify situations that could lead to premature failure and take preventative measures such as improving airflow or replacing thermal paste. Finally, temperature readings can serve as valuable diagnostic tools. Unusual spikes might indicate issues with airflow, failing fans, or malfunctioning components, allowing for early detection and troubleshooting to prevent more serious hardware failures. Therefore, for optimal performance, longevity, and overall health of the GPU, temperature monitoring is a crucial practice.

The kotekan[1] software was initially developed for CHIME software pipeline [59]. Traditional CPUs struggle with the real-time processing demands of CHIME's observations. By leveraging the parallel processing power of GPUs, kotekan can efficiently filter, calibrate, and transform the raw telescope data into a format suitable for further scientific analysis. Following immense efficiency with CHIME afterwards, this pipeline is being used to develop digital receiver software for HIRAX and CHORD. The X-engine software running on the HIRAX correlator experiences power fluctuations due to fluctuating GPU clock speeds. These fluctuations arise from the GPUs dynamically adjusting their clocks based on incoming work. However, the workload for the X-engine exhibits a consistent arrival rate. This presents an opportunity to optimise energy usage and reduce power fluctuations. The rationale of the project is optimised as follows;

- Rationale for Optimisation:
  - Consistent workload: The X-engine software receives data at a uniform rate (e.g., every 120 ms).

[1] https://github.com/kotekan/kotekan

  - Dynamic clocking inefficiency: The GPUs dynamically adjust their clock speeds (e.g., 2000 MHz) based on the incoming work, leading to underutilization (e.g., 50% when processing a frame in 60 ms).

- Proposed Solution:

  - Static clock adjustment: By setting the GPU clock to a fixed value (e.g., 1050 MHz) that aligns closely with the average workload (e.g., to achieve $\sim 90\%$ utilization), we can significantly improve power efficiency and minimize power fluctuations.

- Benefits:

  - Increased efficiency: Setting a static clock based on average workload reduces power consumption and optimises GPU utilisation. Reduced fluctuations: A fixed clock reduces power fluctuations on the AC lines, leading to improved system stability.

In the CHIME system, we did this manually by running AMD commands to set the clocks of the GPU. For HIRAX and other Nvidia-based GPU systems, we can set the clocks dynamically with the NVIDIA Management Library (NVML) when the X-engine starts. Following is the step-by-step routine for making the adjustments,

```
num_blocks:~(num_elements/block_size)*(num_elements/block_size + 1)/2
sizeof_int: 4
```

Addition of hardware clock namely core clock for GPU to time GPU processing such as multiplication and addition operations. Memory clock is dedicated to time memory transfer. We are setting these two clocks as follows;

```
      # Hardware clocks
       gpu_core_clock: 1005    #in MHz
       gpu_mem_clock: 7251     #in MHz
```

For a GPU in High Perfomance Computing (HPC) nodes allowed range of frequencies is limited. To put a sanity check for the clock value that GPU won't be able to recognise, we add the following patch to the module;

```
cudaSetDevice(gpu_id);

   // Find out how many GPUs clocks are allowed.
   unsigned int* mem_clock, core_clock;
   unsigned int mem_count, core_count;
   CHECK_CUDA_ERROR(nvmlDeviceGetSupportedMemoryClocks(gpu_id_, &
  mem_count,  &mem_clock));
```

```
    CHECK_CUDA_ERROR(nvmlDeviceGetSupportedGraphicsClocks(gpu_id_, &
    core_count,  &core_clock));

    INFO("Allowed GPU core clocks(MHz): ");
    for~(int i = 0; i < mem_count; ++i)  {
        INFO("{:d}  ", mem_clock[i]);
    }

    INFO("Allowed GPU graphics clocks(MHz): ");
    for~(int i = 0; i < core_count; ++i)  {
        INFO("{:d}  ", core_clock[i]);
```

Clock setup;

```
set_device_clocks(mem_clock, core_clock, mem_count, core_count);
```

Set all clocks to zero if no frequencies has been chosen by the user;

```
void cudaDeviceInterface::set_device_clocks(unsigned int* mem_clock,
    unsigned int* core_clock,
                                            unsigned int mem_count,
    unsigned int core_count) {

    // Set default clocks to zero
    uint32_t gpu_mem_clock = std::runtime_error(config.get_default<
    uint32_t>(unique_name, "gpu_mem_clock", 0));
    uint32_t gpu_core_clock = std::runtime_error(config.get_default<
    uint32_t>(unique_name, "gpu_core_clock", 0));
```

Userdefined files are fetched from the `config` fie setup.

```
    uint32_t get_gpu_mem_clock, get_gpu_core_clock;

    nvmlDeviceGetMaxClockInfo~(gpu_id_, gpu_mem_clock, get_gpu_mem_clock);
    nvmlDeviceGetMaxClockInfo~(gpu_id_, gpu_core_clock, get_gpu_core_clock
    );
        // Get and update the GPU clocks from the config file
    gpu_mem_clock = std::runtime_error(config.get<uint32_t>(unique_name, "
    gpu_mem_clock"));
    gpu_core_clock = std::runtime_error(config.get<uint32_t>(unique_name,
    "gpu_core_clock"));

    int_gpu_mem_clock = round(gpu_mem_clock);
    int_gpu_core_clock = round(gpu_core_clock);

    if~(int_gpu_mem_clock != 0 && int_gpu_core_clock != 0) {
```

```
      /* For memory clcoks */
      //minima
    if~(int_get_gpu_mem_clock <= round(mem_clock[0]))
      return mem_clock[0];
      //maxima
    if~(int_get_gpu_mem_clock >= round(mem_clock[mem_count - 1]))
      return mem_clock[mem_count - 1];
      //in between cases, apply a search algorithm such as binary search
      int i = 0, j = mem_count, mid = 0;
    while~(i < j) {
      mid =~(i + j) / 2;

      if~(round(mem_clock[mid]) == int_get_gpu_mem_clock)
        return mem_clock[mid];

      /* Assuming the clock values are saved in
          ascending order,
          If target is less than array element,
    then search in left */
      if~(int_get_gpu_mem_clock < round(mem_clock[mid])) {

        // If target is greater than previous
        // to mid, return closest of two
        if~(mid > 0 && int_get_gpu_mem_clock > round(mem_clock[mid - 1])
)
                  if~(int_get_gpu_mem_clock - round(mem_clock[mid - 1])
>= round(mem_clock[mid]) - int_get_gpu_mem_clock)
                      return mem_clock[mid - 1];
                  else
                      return mem_clock[mid];
        j = mid;
      }
```

Follow same searching process to the other half of the array to search nearest value to the clock values passed by the user.

```
        /* Repeat for left half */

      // If target is greater than mid
      else {
        if~(mid <~(mem_count - 1) && int_get_gpu_mem_clock < round(
mem_clock[mid + 1]))
                  if~(int_get_gpu_mem_clock - round(mem_clock[mid]) >=
round(mem_clock[mid + 1]) - int_get_gpu_mem_clock)
                      return mem_clock[mid + 1];
```

```
                    else
                        return mem_clock[mid];

        // update i
        i = mid + 1;
      }
      }
```

Read out the clock setup by the GPU that has the nearest valid value for allowed GPU clocks. And print it out to the kernel prompt.

```
      /* For processing clcoks */
      //minima
    if~(int_get_gpu_core_clock <= round(core_clock[0]))
      return core_clock[0];
      //maxima
    if~(int_get_gpu_core_clock >= round(core_clock[core_count - 1]))
      return core_clock[core_count - 1];
      //in between cases, apply a search algorithm such as binary search
      i = 0, j = core_count, mid = 0;
    while~(i < j) {
      mid =~(i + j) / 2;

      if~(round(core_clock[mid]) == int_get_gpu_core_clock)
        return core_clock[mid];

      /* If target is less than array element,
    then search in left */
      if~(int_get_gpu_core_clock < round(core_clock[mid])) {

        // If target is greater than previous
        // to mid, return closest of two
        if~(mid > 0 && int_get_gpu_core_clock > round(core_clock[mid -
1]))
                    if~(int_get_gpu_core_clock - round(core_clock[mid -
1]) >= round(core_clock[mid]) - int_get_gpu_core_clock)
                        return core_clock[mid - 1];
                    else
                        return core_clock[mid];
        j = mid;
      }
        /* Repeat for left half */

      // If target is greater than mid
```

```
      else {
        if~(mid <~(core_count - 1) && int_get_gpu_core_clock < round(
core_clock[mid + 1]))
                if~(int_get_gpu_core_clock - round(core_clock[mid]) >=
 round(core_clock[mid + 1]) - int_get_gpu_core_clock)
                    return core_clock[mid + 1];
                else
                    return core_clock[mid];

        // update i
        i = mid + 1;
      }
      }
 }

 INFO("Memory clock(MHz) of CUDA GPU: {:d} is {:d}", gpu_id_, mem_clock
[i]);
 INFO("Graphics clock(MHz) of CUDA GPU: {:d} is {:d}", gpu_id_,
core_clock[j]);
```

This experiment investigates the impact of different GPU clock speeds on device temperature. Our initial observations suggest that moderate overclocking can improve performance while prioritising execution time. This finding strengthens the importance of the HIRAX correlator system, which relies on efficient GPU utilisation to achieve optimal processing speeds.

2.9 Concluding Remarks

The Hydrogen Intensity and Real-time Analysis eXperiment (HIRAX) is a highly anticipated radio telescope under construction in the southern hemisphere. With its extensive sky coverage, HIRAX promises to be a powerful tool for FRB research, exceeding the capabilities of instruments like CHIME. The use of outriggers will further enhance FRB localisation. This chapter explored HIRAX's sensitivity compared to other upcoming telescopes and modelled FRB detection rates assuming a uniform source distribution in a nearby universe. Additionally, we discussed the potential for detecting gravitationally lensed FRBs. We also provided a brief overview of the HIRAX digital receiver pipeline, including a module that monitors GPU temperature under varying clock frequencies. The following chapter delves into the application of gravitational lensing in FRBs to investigate the presence of primordial black holes.

3 Gravitational lensing of FRBs

General relativity has undergone rigorous testing within the solar system and for objects at relatively low redshifts. This success has firmly established it as the cornerstone of our understanding of gravity. However, when applied to cosmological scales, the theory appears incomplete. Specifically, it struggles to explain two key phenomena: the current accelerated expansion of the universe, and the inflationary epoch thought to have occurred in the very early universe. These discrepancies suggest the need for additional theoretical elements to reconcile general relativity with observations at the largest scales. [46]. The theory further predicts the existence of singularities, points of infinite density under specific conditions. However, these singularities are often confined to microscopic scales, raising questions about their physical relevance [60]. The limitations of General Relativity (GR) in the strong-field regime necessitate continued investigation of alternative gravity theories. This is further underscored by the inability of GR to fully account for the existence of massive white dwarfs and neutron stars. These objects, inferred from observations of peculiar Type Ia supernovae, exhibit properties that challenge the predictions of GR under extreme gravitational conditions. [61, 62] and LIGO/Virgo GW merger events [63, 64].

The past few years have witnessed a surge in interest in applying modified gravity models not only to cosmological phenomena but also to astrophysical contexts. This renewed focus has seen researchers explore these models in the realm of compact object physics, particularly for explaining the existence of massive white dwarfs [65, 66] and neutron stars [67], the possibility of detecting additional modes of GWs [68, 69], etc. It is important to note that modified theories of gravity often predict the existence of additional gravitational wave modes beyond the standard tensor modes of general relativity. These additional modes can be scalar (spin-0) or vector (spin-1) in nature, and their masses depend on the specific background environment. However, due to their massive nature, these modes are expected to be exponentially damped

on cosmological scales. As a consequence, current gravitational wave detectors, which are primarily sensitive to the weak gravitational waves described by general relativity, are unlikely to be able to detect these additional massive modes [70], and hence it is not straightforward to verify modified gravity theories from GW observations. However, using LIGO/Virgo merger events, constraints were put on the speed of GWs ($c_{\rm gw}$); for example, with the observed time delay between the GW merger event GW 170817 and the gamma-ray burst event GW 170817A, it was found that $-3 \times 10^{-15} < c_{\rm gw}/c - 1 < 7 \times 10^{-16}$ where c is the speed of light [71]. It was later shown that the Horndeski theory satisfies the bounds provided the mass scale m satisfies $2 \times 10^{-35} \lesssim m \ll 10^{15}\,{\rm GeV}$ [72]. Note that in this work, we only consider the massive modes with different spins. For the massless case, the situation could be different as discussed in [73, 74] for constraining the Einstein-æther theory. Using FRB 150418, it was earlier found that the constraint on the photon mass $m_\gamma < 1.8 \times 10^{-14}\,{\rm eV\,c^{-2}}$ [75] and this bound is now stronger over time considering many other FRBs [76, 77]. Moreover, using 16 localized and 60 unlocalized FRBs, the Hubble constant H_0 was estimated to be $H_0 = 73^{+12}_{-8}\,{\rm km\,s^{-1}\,Mpc^{-1}}$ [31]. Note that the error bars are large because of the relatively few FRBs used. Furthermore, using the concept of gravitational lensing in FRBs, Muñoz et al. showed for the first time that the constraint on the fraction of dark matter made up of primordial black holes is $f_{\rm PBH} < 0.08$ assuming some FRBs are lensed by the black hole of mass $M > 20\,M_\odot$ [78]. Later these bounds were improved considering FRB microstructures [79] and extended mass functions [80]. With this technique, Liao et al. visualized this constraint using 110 real FRB data with null detection of lensed FRBs [81]. More recently, using 172 bursts from 114 CHIME FRBs, it was shown that the $f_{\rm PBH}$ bound can change significantly if there is plasma in the path of the light ray which also acts as a decoherence or scattering screen [82]. In this paper, we investigate the effect of modified gravity on the $f_{\rm PBH}$ bound using the non-detection of lensing of 636 CHIME FRBs. We show that modified gravity behaves similarly to plasma lensing, which acts as a screen in the path of the light ray. They both complicate the task of accurately deriving the best constraints.

Gravitational time delays, observed in strong lens systems where a variable background source is multiply imaged by a massive foreground galaxy, provide a direct and powerful method for measuring cosmological distances. The success of time delay cosmography relies on several key factors, including the availability of a suitable sample of lensed quasars or supernovae, precise measurements of time delays, accurate modeling of the gravitational potential of the lensing galaxy, and a thorough understanding of the mass distribution along the line of sight to the source [83]. Accurate modeling of the lensing galaxy's mass distribution is crucial for interpreting time delay measurements. Early models often relied on simplified assumptions, such as the singular isothermal sphere, which led to significant discrepancies in the inferred

values of the Hubble constant (H_0) [84]. Recent advancements in observational techniques, including high-resolution imaging and spectroscopic data, have allowed for more sophisticated mass modeling approaches that incorporate additional constraints [85].The increasing number of known lensed systems due to ongoing and future surveys, such as the LSST (Ivezic et al., 2019) [86]. The ability to measure time delays in a larger sample of lenses will enhance statistical analyses and improve the precision of cosmological parameter estimates. Furthermore, the integration of time delay measurements with other cosmological probes, such as baryon acoustic oscillations and supernovae, will provide a more comprehensive understanding of the universe's structure and dynamics [87].

3.1 Primordial Black Holes for Dark Matter Candidate

Primordial black holes (PBHs) are a fascinating and intriguing candidate for a significant component of dark matter. Formed in the very early universe, possibly during periods of rapid expansion or phase transitions, these compact objects possess immense density and gravitational pull, making them invisible to conventional observation methods. The concept of PBHs as dark matter hinges on their formation in the early universe when density fluctuations were large, leading to the collapse of matter into black holes. The mass of these PBHs would have been determined by the size of the horizon at the time of their formation [88]. The existence of PBHs is supported by various theoretical models and observational evidence, including the detection of gravitational waves from merging black holes, which could potentially be the result of PBHs merging. However, the evidence for PBHs as a substantial fraction of dark matter is still indirect and subject to ongoing research and debate.

One of the key challenges in establishing PBHs as dark matter is the need to constrain their abundance. The fraction of dark matter in PBHs must be within a range that does not conflict with various observational limits. These limits arise from observations of the cosmic microwave background, microlensing events, gamma-ray emissions from evaporating PBHs, and the dynamics of galaxies and clusters. While some studies suggest that PBHs could make up a significant portion of dark matter, other constraints restrict their abundance to a much smaller fraction.

3.1.1 Formation Mechanisms

The formation of PBHs is a complex process that is still not fully understood. It is believed that they form from density fluctuations in the early Universe, which can arise from various sources like inflation, phase transitions, or even the quantum fluctuations of the vacuum [**?**]. These fluctuations, if they exceed a certain threshold, can collapse under their gravity, forming a black hole before the universe has had time to smooth them out.

Primarily, PBHs are theorized to originate from regions of high density in the early universe that undergo gravitational collapse. The conditions for their formation can be elucidated through the concept of density fluctuations, characterized by the density contrast ($\delta = \frac{\rho - \bar{\rho}}{\bar{\rho}}$), where ρ represents the local density and $\bar{\rho}$ denotes the average density of the universe. For a region to collapse into a black hole, the density contrast must exceed a critical threshold, typically around ($\delta_c \approx 0.5$). The mass of the PBH can be estimated by considering a spherical region of radius R that collapses, leading to the expression ($M = \frac{4}{3}\pi R^3 \bar{\rho}$). The average density ($\bar{\rho}$) at the time of collapse can be related to the critical density of the universe, given by ($\rho_c = \frac{3H^2}{8\pi G}$), where H is the Hubble parameter and G is the gravitational constant. Assuming a radiation-dominated universe during the epoch of PBH formation, we find that ($\bar{\rho} \propto a^{-4}$), where a is the scale factor. To connect the mass of the PBH to the density fluctuations, we express the average density in terms of the critical density, leading to the conclusion that the density contrast can be approximated as ($\delta \sim \frac{M}{\bar{\rho} R^3}$). By substituting the relationship between R and M, we derive that (δ) is proportional to the average density. The mass function of PBHs can be derived from the power spectrum of density fluctuations, with the number density of PBHs expressed as ($n(M) \propto P(k) \left|\frac{d\delta}{dM}\right|^{-1}$), where k is related to the mass scale M. Several promising scenarios for PBH formation have been proposed [89], including:

- **Collapse from scale-invariant fluctuations:** If the primordial density fluctuations are scale-invariant, meaning they have the same amplitude across all scales, then a power-law mass function for PBHs is expected. However, this scenario is not favoured by current observations of the cosmic microwave background.

- **Collapse from inflationary fluctuations:** Inflationary models, which are widely accepted to explain the homogeneity and flatness of the universe, can generate density fluctuations that lead to PBH formation. However, the required amplitude of these fluctuations needs to be fine-tuned, raising concerns about their plausibility.

- **Collapse at phase transitions:** During the early Universe, several phase transitions occurred, such as the electroweak phase transition and the QCD [90] phase transition. These transitions can create large density fluctuations that could collapse to form PBHs. The mass of these PBHs is typically determined by the horizon mass at the time of the transition, leading to potentially interesting mass ranges.

- **Collapse from bubble collisions:** During phase transitions, bubbles of different phases can collide and interact. This process can generate enough energy and density fluctuations to form PBHs.

- **Collapse of cosmic strings:** Cosmic strings, which are hypothetical topological defects formed in the early Universe, can self-intersect and form loops. These loops can then collapse to form PBHs, potentially leading to an extended mass function.
- **Collapse of domain walls:** Domain walls [91], which are another type of topological defect, can also collapse to form PBHs. This scenario is less well-studied than the others, but it could potentially lead to PBHs with a wide range of masses.

It is important to note that these are just a few examples of the many proposed scenarios for PBH formation. The exact mechanism by which PBHs form is still a subject of ongoing research and debate. The potential implications of PBHs as dark matter are far-reaching. They could provide a mechanism for seeding the formation of supermassive black holes at the centres of galaxies, and their gravitational interactions could influence the large-scale structure.

3.1.2 Potential Signatures and Observational Evidence of PBH and Observational Bounds

The search for observational signatures of PBHs is a challenging but rewarding task. Here are some of the potential signatures that scientists are looking for:

- **Gravitational Wave Detections**: One of the most significant sources of constraints on PBHs comes from gravitational wave observations, particularly those made by the Laser Interferometer Gravitational-Wave Observatory (LIGO) and Virgo. These observatories have detected several events of black hole mergers, which can be analyzed to infer the masses of the merging black holes. If PBHs constitute a significant fraction of the dark matter, their mergers would contribute to the observed gravitational wave signals [92]. The mass distribution of the detected black holes provides constraints on the possible mass range of PBHs [92]. For instance, the detection of black hole mergers with masses in the range of a few to several tens of solar masses suggests that if PBHs exist in this mass range, they must not exceed a certain abundance to avoid conflicting with the observed merger rates. Studies have shown that the fraction of dark matter composed of PBHs in this mass range is constrained to be less than approximately 10% to 20%, depending on the specific models of PBH formation and the merger rates observed.
- **Microlensing Surveys**: Microlensing surveys conducted by the MACHO (Massive Compact Halo Objects) and EROS (Experience for Research on Observational Supernovae) collaborations, search for transient events caused by the gravitational lensing of light from distant stars by compact objects, including PBHs. The results from these surveys have provided upper limits on the fraction of dark matter that can be composed of PBHs,

particularly in the mass range of (10^{-8}) to (10^{-5}) solar masses [93]. For example, the MACHO collaboration found that PBHs could not account for more than about 20% of the dark matter in the Milky Way halo in this mass range. These constraints are critical because they help delineate the parameter space for PBH models and inform theoretical predictions regarding their formation mechanisms.

- **Cosmic Microwave Background (CMB) Observations** : CMB observations also impose significant constraints on PBHs. The CMB provides a snapshot of the universe when it was about 380,000 years old, and its temperature fluctuations encode information about the density fluctuations that existed at that time. If PBHs formed from large density fluctuations, they would leave an imprint on the CMB. Specifically, the presence of PBHs can affect the amplitude of the CMB power spectrum, particularly on small scales. Current CMB data, such as those from the Planck satellite, have been used to constrain the abundance of PBHs by analyzing the power spectrum of temperature fluctuations. These analyses suggest that PBHs cannot constitute a significant fraction of dark matter, particularly in the mass range of (10^{-6}) to (10^{-3}) solar masses [88], as their presence would lead to observable deviations from the expected CMB power spectrum.

- **Signatures of accretion and evaporation:** PBHs can accrete gas and dust, leading to the emission of X-rays and γ-rays. Observations of these emissions from galaxies and clusters of galaxies can be used to constrain the abundance of PBHs [94]. Additionally, the evaporation of small PBHs through Hawking radiation could lead to the production of high-energy particles, which could be observed as a diffuse flux of γ-rays or neutrinos.

- **Dynamical effects on galaxies and clusters:** PBHs can affect the dynamics of galaxies and clusters of galaxies [94], such as by disrupting star clusters or by generating tidal tails. Observing these effects can be used to constrain the abundance of PBHs in the mass range 106M to 1012M.

Various observational techniques have been employed to place bounds on the abundance and mass distribution of PBHs. For instance, gravitational wave detections from mergers of black holes, such as those observed by LIGO and Virgo, provide constraints on the mass range of PBHs, particularly in the range of a few to several tens of solar masses. Additionally, microlensing surveys, such as those conducted by the MACHO and EROS collaborations, have been used to constrain the fraction of dark matter that can be composed of PBHs, particularly in the mass range of $(10^{-8})to(10^{-5})$ solar masses. Furthermore, cosmic microwave background (CMB) observations impose limits on the density fluctuations that could lead to PBH formation, thereby constraining the power spectrum of primordial density perturbations. Figure 3.1 shows

the constraints on PBH mass with different observations, described above [1]. In this chapter, we attempt to add another bound based on FRBs assuming the presence of the simplest case of modified gravity. These constraints collectively inform theoretical models of PBH formation and help delineate the parameter space in which PBHs can exist without conflicting with current astrophysical observations.

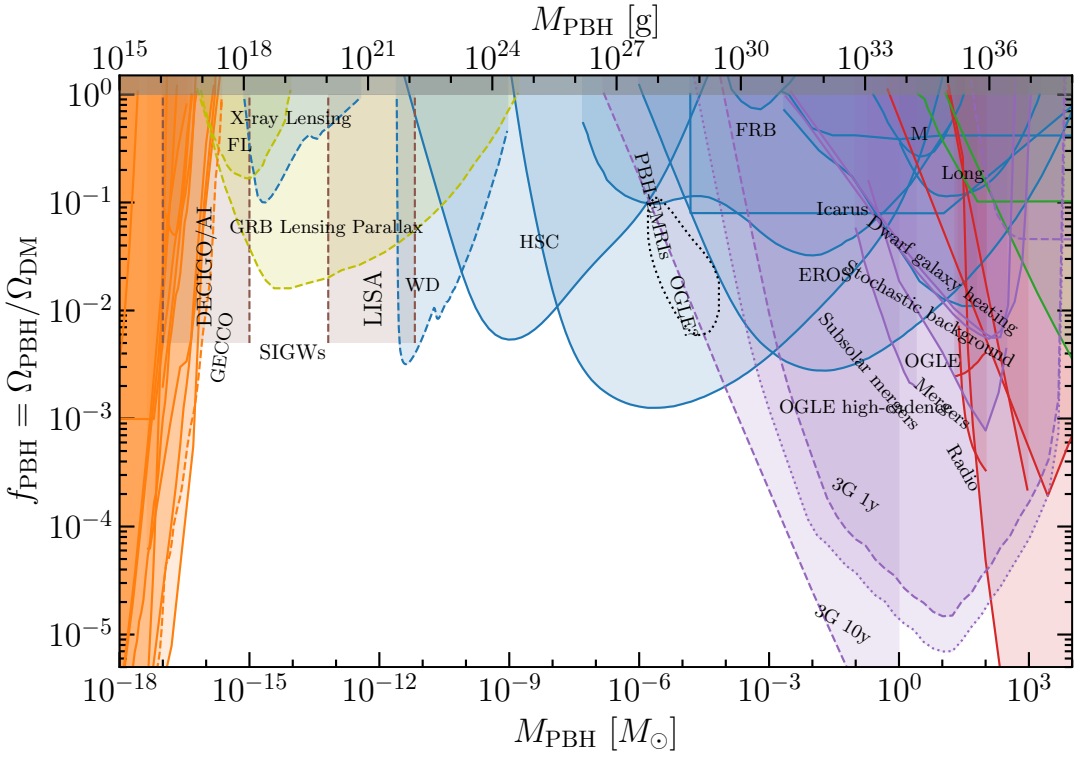

Figure 3.1 The image shows the constraints on the abundance of PBHs as a function of their mass. The horizontal axis represents the mass of PBHs in units of solar mass (M), while the vertical axis represents the fraction of dark matter made up by PBHs. The coloured regions represent various observational constraints from different methods, such as gravitational lensing, gravitational waves, and microlensing. The shaded regions represent the allowed regions, while the unshaded regions represent excluded regions. This plot helps to narrow down the possible range of masses and abundances for PBHs, providing insights into their role in the early universe and their potential as a source of dark matter [1].

3.1.3 Primordial Black Holes Versus Particle Dark Matter

The possibility of PBHs contributing to the dark matter is compelling, but there are still challenges:

- **Fine-tuning:** The small fraction of overdense regions that need to collapse to form PBHs to account for the observed dark matter density requires fine-tuning of cosmological parameters [95]. This raises questions about the naturalness of the PBH scenario.
- **Clustering:** The clustering of PBHs could significantly weaken the constraints [96] derived from lensing and dynamical effects, making it difficult to definitively rule out their contribution to the dark matter.
- **Alternative Dark Matter Candidates:** Particle physics offers a rich array of alternative dark matter candidates, such as WIMPs [97], sterile neutrinos, axions, and fuzzy dark matter. Determining the true nature of dark matter requires extensive experimental searches and theoretical investigation.

3.1.4 Combined Primordial Black Holes and Particle Dark Matter Scenarios

The dark matter might not be dominated by a single type of particle or object. Combined scenarios involving PBHs and particle dark matter have been proposed:

- **WIMP Annihilation Around PBHs:** If WIMPs make up most of the dark matter, they could be accreted around PBHs, leading to enhanced annihilation rates and a distinctive flux of gamma rays [**?**]. This scenario could be tested by observations of the gamma-ray sky and the distribution of dark matter halos.
- **Planck-Mass Relics from PBH Evaporation:** The evaporation of PBHs might leave behind stable Planck-mass relics [98]. These relics could potentially contribute to the dark matter and might be detectable through their gravitational effects or possibly through their electric charge.

These combined scenarios provide a more nuanced picture of dark matter, where different components interact and contribute to the overall energy density. Further investigations and observational tests are necessary to explore the possibility of these combined scenarios.

3.1.5 Power Spectrum from Primordial Black Holes (PBHs)

The mass spectrum of these black holes is crucial for understanding their potential contributions to dark matter and their effects on cosmic structure formation. The power spectrum of density perturbations, which describes the distribution of fluctuations in the early universe, plays a significant role in determining the abundance and mass distribution of PBHs. Density Fluctuations and PBH Formation The formation of PBHs is closely linked to the amplitude of

primordial density fluctuations. During inflation, quantum fluctuations in the inflaton field lead to a spectrum of density perturbations characterized by a power spectrum (P(k)), where (k) is the wave number associated with the perturbations. The power spectrum can be expressed as:

$$[P(k) \propto k^n] \tag{3.1}$$

where (n) is the spectral index. A scale-invariant spectrum corresponds to (n = 1), while deviations from this value indicate a tilt in the spectrum [99]. Critical Collapse and Mass Function The mass function of PBHs is influenced by the critical collapse of overdense regions in the early universe. The relationship between the density contrast (δ) and the mass of the resulting black holes can be described by critical scaling relations. For a Gaussian distribution of density perturbations, the fraction of the universe's mass in PBHs can be approximated by:

$$[\beta(M) \propto \int_{\delta_c}^{\infty} P(\delta), d\delta] \tag{3.2}$$

where (δ_c) is the critical density threshold for collapse [100]. This integral reflects the probability of forming a PBH of mass (M) from the density fluctuations characterized by ($P(\delta)$). Power Spectrum and PBH Mass Distribution The mass distribution of PBHs can be derived from the power spectrum of density fluctuations. For a given inflationary model, the power spectrum can be computed, and the resulting PBH mass function can be expressed as:

$$[\frac{dn}{dM} \propto M^{-2} P(M)] \tag{3.3}$$

where (n) is the number density of PBHs [94]. The mass function is expected to be extended rather than monochromatic, reflecting the broad range of scales present in the primordial power spectrum. Further discussion regarding power spectrum generation is given in [94] and this point is out of the scope of this thesis.

3.2 Types of Gravitational Lensing

Gravitational lensing is a phenomenon predicted by Einstein's theory of general relativity where the gravity of massive objects, such as galaxies or clusters of galaxies, bends and distorts the path of light from distant objects passing through their gravitational field. The concept of gravitational lensing was first proposed by astronomer Orest Chwolson in 1924 [101]. He envisioned how a star could act as a lens, creating multiple images of a more distant star aligned behind it. This effect, known as strong lensing, would result in a dramatic magnification and distortion of the light from the distant source. However, the probability of observing strong lensing was considered to be extremely low due to the precise alignment required. The community focused on the prediction of light bending by the Sun, leading to the famous 1919

solar eclipse expedition organized by Arthur Eddington and Frank Dyson. This expedition aimed to confirm Einstein's prediction of starlight deflection by the Sun's gravity. While the results were initially controversial, they ultimately solidified Einstein's theory of general relativity and brought gravitational lensing to the forefront of scientific attention. This effect acts as a cosmic magnifying glass, providing the community with a unique tool to study distant and faint objects that would otherwise be invisible. Gravitational lensing is categorized based on the strength of the lensing effect and the observed image characteristics. Three main types are commonly recognized: strong lensing, weak lensing, and microlensing.

3.2.1 Strong Lensing

Strong lensing occurs when the gravitational field of the lens is sufficiently strong to create multiple images of a distant background source. This typically happens when the source, lens, and observer are closely aligned, forming an "Einstein Ring" or multiple, distorted images. A key parameter in strong lensing is the Einstein radius, denoted by ΘE. This is the angular radius of the region around the lensing object where a significant amount deflects light rays. The mass of the lensing object, the distance to the lens, and the distance to the source determine the Einstein radius. When a source is located within the Einstein radius of a lens, multiple images of the source can be observed. These images are often distorted and magnified compared to the source. The number and configuration of images depend on the relative positions of the lens, the source, and the observer [101]. The brightness of the images created by strong lensing is amplified compared to the source. This magnification is related to the lensing potential and the positions of the images.

3.2.1.1 Strong Lensing Applications

Strong lensing has proven to be a valuable tool [102] for a variety of astronomical studies:

- **Mass Determination:**Strong lensing allows us to measure the mass of the lensing object, such as a galaxy or cluster of galaxies, by analysing the positions and magnifications of the multiple images [103]. This provides a direct way to estimate the mass of dark matter within these structures.
- **Distant Object Studies:** Strong lensing can magnify distant objects, making them appear brighter and larger. This allows us to study faint, high-redshift galaxies and quasars [103] that would otherwise be too faint to observe directly.
- **Cosmological Parameters:** By measuring the time delay between the arrival of light from multiple images of a variable source, we can determine the Hubble Constant [101], a key parameter in cosmology that describes the expansion rate of the universe.

- **Structure of Dark Matter:** Strong lensing can be used to probe the distribution of dark matter within galaxies and clusters of galaxies. By studying the shapes and positions of lensed images [101], we can map the distribution of dark matter in a way that is not possible with other methods.

Detecting strong lensing events by PBHs is challenging, especially for smaller PBHs that induce microlensing events. These events are rare and often difficult to distinguish from other astrophysical events. While strong lensing provides valuable information about PBHs, it doesn't provide a complete picture. For example, it is difficult to determine the mass of a PBH from a single lensing event. Since this initial discovery, numerous other strong lensing systems have been discovered, ranging from simple cases of double images to complex cases of multiple images, arcs, and rings. These systems have provided a wealth of information about the distribution of matter, the properties of distant galaxies and quasars, and even the expansion rate.

3.2.2 Weak Lensing

Weak lensing occurs when the gravitational field of the lens is not strong enough to create multiple images, but still causes a subtle distortion of the shapes of background galaxies. This distortion, while subtle, is measurable through statistical analysis of a large number of galaxies [104].

3.2.2.1 Shear and Convergence

Weak lensing manifests itself through two main effects: shear and convergence. Shear stretches and twists the images of background galaxies, while convergence magnifies them. The amount of shear and convergence experienced by a galaxy depends on the mass distribution of the lens and its relative position to the background galaxy.

3.2.3 Weak Lensing Applications

Weak lensing provides a powerful tool to study the large-scale structure:

- **Mapping Dark Matter:** Weak lensing allows us to map the distribution of dark matter on large scales, providing a unique and independent method of measuring its abundance and distribution compared to other methods [101].

- **Cosmological Parameters:** Weak lensing can be used to measure the geometry of the universe [104], including its curvature, and to constrain cosmological parameters such as the matter density and dark energy density.

- **Understanding Galaxy Evolution:** Weak lensing can reveal how the distribution of dark matter affects the evolution of galaxies [101], providing insights into their formation and growth.

3.2.4 Microlensing

Microlensing is a special case of gravitational lensing where the source and lens are both unresolved. In microlensing, several images of the source are formed. The observer does not resolve them and thus appears as a single, brighter source. This typically occurs when a star passes in front of another star or a compact object like a brown dwarf [101]. The lensing object magnifies the light from the background star, causing its brightness to increase temporarily.

3.2.4.1 Microlensing Light Curves

The magnification of the source star due to microlensing results in a characteristic light curve. This light curve shows a temporary increase in the brightness of the star as the lensing object passes in front of it. The duration and shape of the light curve depend on the mass of the lensing object, its relative speed, and the alignment of the source and lens.

3.2.4.2 Microlensing Applications

- **Dark Matter Detection:** Microlensing surveys have been used to search for dark matter in the form of massive compact halo objects (MACHOs) [105] within the Milky Way halo.
- **Exoplanet Detection:** Microlensing can be used to detect exoplanets, or planets orbiting stars other than our Sun. The presence of a planet orbiting the lensing star will cause a characteristic "bump" in the light curve, providing evidence of the planet [106].
- **Stellar Properties:** Microlensing can be used to study the properties of stars, such as their masses and radii.

Gravitational lensing has proven to be a powerful tool in modern astronomy, providing insights into the distribution of dark matter, the properties of distant objects, and the evolution of the universe.

3.3 Transients and Strong Lensing

The field of strong gravitational lensing has undergone a dramatic transformation in recent years, fueled by the advent of powerful new telescopes and innovative analysis techniques. One of the most exciting recent developments has been the application of strong gravitational lensing to the study of radio transients.

Radio transients are ideal targets for strong gravitational lensing for several key reasons. First, they are often extremely luminous and compact, making them bright enough to be detectable even at high redshifts and small enough to be effectively lensed by intervening galaxies [107]. Second, their fast variability on timescales ranging from milliseconds to seconds provides a unique tool for measuring time delays. The compact size of the source also means that wave optics effects can play an important role in the lensing process, introducing intriguing additional features in the lensed images that can be exploited for further insights.

The first confirmed detection of a plasma lensed radio transient was a repeating FRB known as FRB 121102. This event, discovered in 2012, is characterised by properties such as its repetitive nature and association with a low-metallicity dwarf galaxy. The time delays between the multiple images were found to be far shorter than expected, indicating that the lensing object must be highly compact and massive [108]. Although the lensing is due to plasma and not gravitational lensing, it cannot be used to constrain the nature of dark matter but observations of strongly lensed FRBs can be used to study the properties of FRBs themselves, including their intrinsic luminosities, their emission mechanisms, and their spatial distribution. By measuring the time delays and magnifications of lensed FRBs, it may be possible to improve our understanding of the peculiar environment in which these transients originate.

Since FRBs can be observed at higher redshifts than pulsars, their lensing provides a unique opportunity to measure the Hubble constant, independent of other methods [101]. By measuring the time delays and the magnification of lensed FRBs, it may be possible to obtain more precise measurements of the Hubble constant than can be obtained from any other source. This information is crucial for addressing the current tension between measurements of the Hubble constant from distant supernovae and the cosmic microwave background radiation. The potential of strong gravitational lensing for the study of radio transients extends beyond fast radio bursts. It has also been applied to the study of gamma-ray bursts (GRBs) [109]. While the compact size of GRBs suggests that they should be ideal targets for strong lensing, the high variability of GRBs presents significant challenges for measuring time delays and magnifications. In addition, the high energy of GRBs makes it difficult to identify lensing objects that produce subtle distortions in the observed light curves. Nevertheless, there have been several reports of possible candidates for strongly lensed GRBs, and the search for transient events is ongoing.

The detection of multiple images of transients will provide new and unique insights into the structure of galaxies and clusters of galaxies, the nature of dark matter, and the fundamental laws of physics. Here we take an example of point mass lenses [101] specifically of strong lensing phenomena for FRBs and give bounds on PBH as described in the rest of the chapter.

3.4 Time delay in modified gravity

Assuming the metric signature $(+,-,-,-)$, in the spherical polar coordinates (t, r, θ, ϕ), let us consider the following spherically symmetric line element

$$\mathrm{d}s^2 = B(r)c^2\,\mathrm{d}t^2 - A(r)\,\mathrm{d}r^2 - r^2\,\mathrm{d}\theta^2 - r^2\sin^2\theta\,\mathrm{d}\phi^2\,. \tag{3.4}$$

Hence, the time required for the light ray to reach the distance of closest approach r_0 from an arbitrary distance r, or vice-versa, is given by [110]

$$t\,(r, r_0) = \frac{1}{c}\int_{r_0}^{r}\sqrt{\frac{A(r)/B(r)}{1-\frac{B(r)}{B(r_0)}\left(\frac{r_0}{r}\right)^2}}\,\mathrm{d}r\,. \tag{3.5}$$

In GR, for the Schwarzschild metric outside of a black hole of mass M_L, expanding up to $\mathcal{O}(M_\mathrm{L}/r)$, the above expression can be written as follows [110]:

$$t\,(r, r_0) = \frac{1}{c}\sqrt{r^2 - r_0^2} + \frac{2GM_\mathrm{L}}{c^3}\ln\left(\frac{r+\sqrt{r^2-r_0^2}}{r_0}\right) + \frac{GM_\mathrm{L}}{c^3}\sqrt{\frac{r-r_0}{r+r_0}}, \tag{3.6}$$

where G is Newton's gravitational constant.

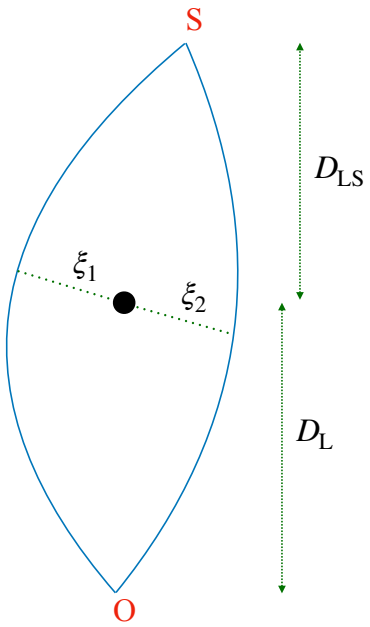

Figure 3.2 Schematic diagram of deflection of a light ray in the presence of a compact object.

Now consider that a light ray travels from a source at S to an observer at O, passing by a compact object as shown in figure 3.2. Due to the curvature of spacetime, the compact object behaves like a lens, and the light ray is deflected forming two images of the source at S for the observer at O. It is worth noting that here we are only considering the case of strong lensing where multiple images can be formed for a single source. Weak lensing and microlensing, where only a single deformed image is formed, are not considered here as we are interested in measuring the differences in delays between the two lensed images. Let us assume that the closest distances of these light rays from the compact object are ξ_1 and ξ_2, and the angular diameter distances of the compact object from O and S are respectively $D_{\rm L}$ and $D_{\rm LS}$. Therefore, defining the Einstein radius $\theta_{\rm E}$ as

$$\theta_{\rm E} = \sqrt{\frac{4GM_{\rm L}}{c^2}\frac{D_{\rm LS}}{D_{\rm L}\left(D_{\rm L}+D_{\rm LS}\right)}}, \tag{3.7}$$

we define the following dimensionless quantities

$$y = \frac{r}{\theta_{\rm E}\left(D_{\rm L}+D_{\rm LS}\right)} \tag{3.8}$$

$$\text{and} \quad \zeta_{1,2} = \frac{\xi_{1,2}}{D_{\rm L}\theta_{\rm E}}, \tag{3.9}$$

such that the positions of the lensed images are given by

$$\zeta_{1,2} = \frac{1}{2}\left(y \pm \sqrt{y^2+4}\right). \tag{3.10}$$

If the redshift of the lens is $z_{\rm L}$, the differential time delay between the two images is given by

$$\Delta t = (1+z_{\rm L})\left[t\left(D_{\rm LS},\xi_1\right)+t\left(D_{\rm L},\xi_1\right)-t\left(D_{\rm LS},\xi_2\right)-t\left(D_{\rm L},\xi_2\right)\right]. \tag{3.11}$$

Assuming $\xi_1, \xi_2 \ll D_{\rm L}, D_{\rm LS}$, for the Schwarzschild metric, the above expression can be approximated as [103]

$$\Delta t \approx \frac{4GM_{\rm L}\left(1+z_{\rm L}\right)}{c^3}\left[\frac{y}{2}\sqrt{y^2+4}+\ln\left(\frac{\sqrt{y^2+4}+y}{\sqrt{y^2+4}-y}\right)\right]. \tag{3.12}$$

Let us now consider the following generic modified spherically symmetric metric with modified gravity parameter Ψ capturing the effect of modified gravity

$$\mathrm{d}s^2 = \left(1 - \frac{2GM_{\mathrm{L}}}{c^2 r} + \Psi r^2\right) c^2\,\mathrm{d}t^2 - \frac{1}{1 - \frac{2GM_{\mathrm{L}}}{c^2 r} + \Psi r^2}\,\mathrm{d}r^2 - r^2\,\mathrm{d}\theta^2 - r^2 \sin^2\theta\,\mathrm{d}\phi^2\,. \tag{3.13}$$

It is also known as the Schwarzschild–de Sitter (SdS) metric. In GR, the Schwarzschild metric is a unique solution of the Einstein field equation according to Birkhoff's theorem. However, if one incorporates the cosmological constant Λ in the field equation, the solution resembles the aforementioned metric of equation (3.13). It is worth noting that this solution no longer readily reduces to the flat Minkowski metric in the limit $r \to \infty$. Moreover, this metric is also a solution for different modified gravity theories. For example, in $f(R)$ gravity, it was shown that the above metric is a solution when R remains constant i.e. $R = R_0$ provided $R_0 f'(R_0) - 2f(R_0) = 0$ [111]. In such a case, we have $\Psi = R_0/12$. Note that by replacing $f(R)$ by $f(X) - f'(X)(R - X)$ with X being a dynamical scalar field and defining $\phi = -f'(X)$, one can show that the action of $f(R)$ gravity resembles the same for scalar-tensor theory provided $f''(X) \neq 0$. Moreover, one can define a potential $V(\phi)$ such that it follows $\phi^2 V = \phi X(\phi) - f(X(\phi))$ [112]. This potential provides the scalar field with a non-zero effective mass in the presence of matter via the 'chameleon mechanism' [113, 114]. The mass of this scalar field depends on the curvature and thus density of the system. Therefore, $f(R)$ gravity turns out to be a subset of chameleon gravity. Furthermore, the SdS metric is also a solution in $f(T)$ gravity with T being the scalar torsion [115].

Now, substituting the SdS metric in equation (3.5) and expanding up to $\mathcal{O}(M/r)$, we obtain

$$\begin{aligned} t\,(r, r_0) = {} & \frac{\tan^{-1}\left(\sqrt{\Psi}\sqrt{\frac{r^2 - r_0^2}{1 + \Psi r_0^2}}\right)}{c\sqrt{\Psi}} + \frac{2GM_{\mathrm{L}}}{c^3}\tanh^{-1}\left[r\sqrt{\frac{1 + \Psi r_0^2}{r^2 - r_0^2}}\right] \\ & + \frac{GM_{\mathrm{L}}}{c^3}\frac{(1 - \Psi r r_0)}{\sqrt{1 + \Psi r_0^2}\,(1 + \Psi r^2)}\sqrt{\frac{r - r_0}{r + r_0}}. \end{aligned} \tag{3.14}$$

Therefore, the differential time delay between the two images is given by

$$\begin{aligned} \Delta t \approx {} & \frac{1 + z_{\mathrm{L}}}{c\sqrt{\Psi}}\tan^{-1}\left[\frac{2\sqrt{\Psi}\,(D_{\mathrm{L}} + D_{\mathrm{LS}})\,(\xi_1^2 - \xi_2^2)\,(2 - \Psi\xi_1^2)\,(2 - \Psi\xi_2^2)}{D_{\mathrm{L}} D_{\mathrm{LS}}\,(2 - \Psi\xi_1^2)^2\,(2 - A\xi_2^2)^2 - 4\Psi\,(\xi_1^2 - \xi_2^2)^2}\right] \\ & + \frac{4GM_{\mathrm{L}}\,(1 + z_{\mathrm{L}})}{c^3}\ln\left(\frac{\sqrt{y^2 + 4} + y}{\sqrt{y^2 + 4} - y}\right). \end{aligned} \tag{3.15}$$

In the limit $\Psi\xi_1^2, \Psi\xi_2^2 \ll 1$, it reduces to

$$\Delta t = \frac{1+z_{\rm L}}{c\sqrt{\Psi}} \tan^{-1}\left[\frac{\sqrt{\Psi}\,(D_{\rm L}+D_{\rm LS})\,(\xi_1^2-\xi_2^2)}{2D_{\rm L}D_{\rm LS}}\right] + \frac{4GM_{\rm L}\,(1+z_{\rm L})}{c^3}\ln\left(\frac{\sqrt{y^2+4}+y}{\sqrt{y^2+4}-y}\right) \tag{3.16}$$

$$= (1+z_{\rm L})\left[\frac{1}{c\sqrt{\Psi}}\tan^{-1}\left(\sqrt{\Psi}\frac{4GM}{c^2}\frac{y}{2}\sqrt{y^2+4}\right) + \frac{4GM_{\rm L}}{c^3}\ln\left(\frac{\sqrt{y^2+4}+y}{\sqrt{y^2+4}-y}\right)\right]. \tag{3.17}$$

As mentioned above, we are only interested in the case of strong lensing and this limit ensures that the light ray passes close enough to the black hole which can produce multiple images. It is evident that this expression reduces to equation (3.12) as $\Psi \to 0$. Moreover, the magnification ratio of these two images is given by

$$\mu = \left(\frac{y+\sqrt{y^2+4}}{y-\sqrt{y^2+4}}\right)^2. \tag{3.18}$$

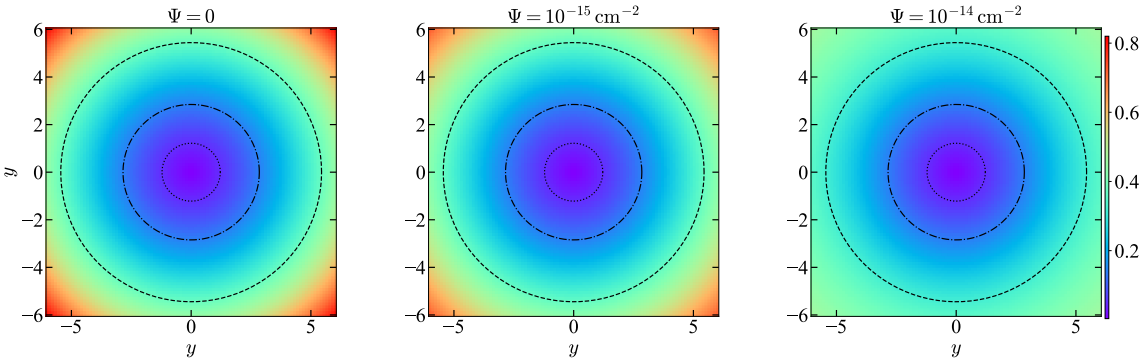

Figure 3.3 Differential delay Δt for $1\,M_\odot$ lens mass as Ψ increases. The color bar shows Δt in the units of ms. The dotted, dash-dotted, and dashed circles depict the radii of the delay surfaces corresponding to $\mu = 10$, 100, and 1000, respectively.

Figure 3.3 shows different time delay surfaces as Ψ changes assuming $z_{\rm L} = 0$ But this can be easily translated to other $z_{\rm L}$ values as shown in Figure 3.4. The dotted, dash-dotted, and dashed circles indicate the amount of time delay Δt between the two lensed images for different magnifications. It is evident that as Ψ increases, Δt at the same radius decreases. In other words, while obtaining the same magnification of the lensed images, the time difference between the two rays to reach the observer is reduced. This is because as Ψ increases, the effective mass of the lens decreases; thus producing less gravitational curvature around it, and

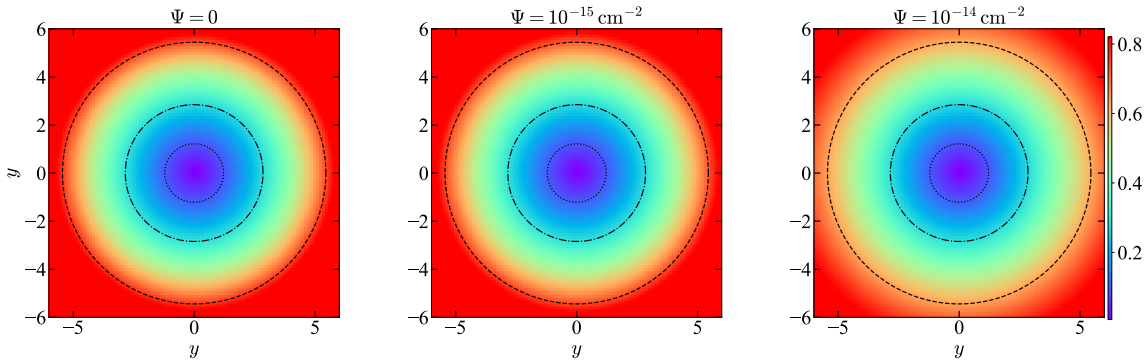

Figure 3.4 Differential delay Δt for $1\ M_\odot$ and $z_L = 1$ and lens mass as Ψ increases. The color bar shows Δt in the units of ms. The dotted, dash-dotted, and dashed circles depict the radii of the delay surfaces corresponding to $\mu = 10$, 100, and 1000, respectively.

the light rays are effectively deflected less. In some sense, the presence of modified gravity somewhat screens the compact object.

3.5 Effect of modified gravity in lensing of fast radio bursts

In this article, we consider 636 FRBs detected by CHIME[1]. We are limited by the dimmest image which should also be bright enough to be detected, which sets an upper limit in μ. Denoting S/N to be the signal-to-noise ratio of the primary peak of the burst, it was inferred that the bounds on μ were $1 < \mu < 1/3 \times$ S/N [79]. Assuming the redshift of the source z_S, its optical depth is given by [78]

$$\tau(M_L, z_S) = \int_0^{z_S} \mathrm{d}\chi(z_L)\,(1+z_L)^2\, n_L \sigma(M_L, z_L), \tag{3.19}$$

where $\chi(z)$ is the comoving distance at a redshift z, n_L is the average comoving number density of the lens, and σ is the lensing cross section for a point mass lens, given by the annulus between the minimum and maximum impact parameters, y_{min} and y_{max}, respectively. Mathematically, it is represented by

$$\sigma(M_L, z_L) = \frac{4\pi G M_L D_L D_{LS}}{c^2 D_S}\left[y^2_{max}(\mu) - y^2_{min}(M_L, z_L)\right]. \tag{3.20}$$

Note that as we are interested in constraints on primordial mass black holes making up Dark Matter, we are not restricted to solar mass black holes. Rather we want to consider primordial mass black holes, and hence we denote M_L as the mass of the primordial mass black hole. The

[1] as of April 2023

comoving distance $\chi(z_{\rm L})$ is given by

$$\chi(z_{\rm L}) = c\int_0^{z_{\rm L}} \frac{{\rm d}z}{H(z)}, \tag{3.21}$$

where $H(z)$ is the Hubble function at a redshift z, given by $H(z) = H_0\sqrt{\Omega_{\rm m}\,(1+z)^3 + \Omega_\Lambda}$ with $\Omega_{\rm m}$ and Ω_Λ respectively being the present matter and vacuum density fraction. Moreover, assuming a monochromatic mass function with a peak at mass $M_{\rm L}$, we define the following lens mass function ${\rm d}n_{\rm L}/{\rm d}M$ as [82]

$$\frac{{\rm d}n_{\rm L}}{{\rm d}M} = \frac{\rho_{\rm crit}}{M_{\rm L}}\, f_{\rm PBH}\,\Omega_{\rm c}\,\delta(M - M_{\rm L}), \tag{3.22}$$

such that

$$\int \frac{{\rm d}n_{\rm L}}{{\rm d}M} M\,{\rm d}M = \rho_{\rm crit}\, f_{\rm PBH}\,\Omega_{\rm c}. \tag{3.23}$$

Here $f_{\rm PBH}$ is the fraction of dark matter made up of primordial mass black holes, which act as the lens, $\Omega_{\rm c}$ is the current cold dark matter density, and $\rho_{\rm crit} = 3H_0^2/8\pi G$ is the critical density of the universe. Now, substituting equations (3.20)–(3.23) in equation (3.19), we obtain

$$\tau(M_{\rm L}, z_{\rm S}) = \frac{3}{2} f_{\rm PBH}\Omega_{\rm c}\int_0^{z_{\rm S}} {\rm d}z_{\rm L}\,\frac{H_0^2}{cH(z_{\rm L})}\frac{D_{\rm L}D_{\rm LS}}{D_{\rm S}}\,(1+z_{\rm L})^2\left[y^2_{\rm max}(\mu) - y^2_{\rm min}(M_{\rm L}, z_{\rm L})\right]. \tag{3.24}$$

The determination of redshifts of FRBs using their measured DM values is important for this work briefly introduced in Equation 1.2 we explain it in detail here. The current CHIME/FRB dataset [116–118] reports the DM as well as the excess DM of FRBs, which we use to estimate the redshifts of these FRBs. The excess DM receives contributions from the host galaxy, the IGM, and foreground galaxies if any, and is found by subtracting the DM contribution of the Milky Way using the NE2001 model [119]. Observation/selection biases and propagation effects introduce noise into the CHIME/FRB data set, therefore we introduce cutoffs suggested by the CHIME/FRB team for our sample data set. The average excess DM ($\langle {\rm DM_{exc}}(z_{\rm S})\rangle$) measured for the bursts has two major contributions: from the inter-galactic medium (IGM) and from the host galaxy. Hence, based on [120], $\langle {\rm DM_{exc}}(z_{\rm S})\rangle$ is given by

$$\langle {\rm DM_{exc}}(z_{\rm S})\rangle = \langle {\rm DM_{IGM}}(z_{\rm S})\rangle + \langle {\rm DM_{Host}}(z_{\rm S})\rangle, \tag{3.25}$$

where following [82], the median DM contribution from host galaxies is assumed to be $117\,\mathrm{pc\,cm^{-3}}$ at the source of the burst, such that

$$\langle \mathrm{DM_{Host}}(z_\mathrm{S})\rangle = \frac{117\,\mathrm{pc\,cm^{-3}}}{1+z_\mathrm{S}}. \tag{3.26}$$

Here, $\langle \mathrm{DM_{IGM}}(z)\rangle$ is the average DM contribution from the IGM along the line of sight. It is primarily a function of the electron density along the line of sight:

$$\langle \mathrm{DM_{IGM}}(z_\mathrm{S})\rangle = \frac{3cH_0\Omega_\mathrm{b}}{8\pi G m_\mathrm{p}} \int_0^{z_\mathrm{S}} \frac{f_\mathrm{IGM}(z)\chi(z)(1+z)}{\sqrt{\Omega_\mathrm{m}\,(1+z)^3+\Omega_\Lambda}}\,\mathrm{d}z\,, \tag{3.27}$$

where Ω_b is the baryonic matter density, m_p is the proton mass, f_IGM is the baryon mass fraction in the IGM, and $\chi(z)$ the ionisation fraction along the line of sight, given by

$$\chi(z) = Y_\mathrm{H}\chi_\mathrm{e,H}(z) + \frac{1}{2}Y_\mathrm{p}\chi_\mathrm{e,He}(z), \tag{3.28}$$

with $\chi_\mathrm{e,H}$ and $\chi_\mathrm{e,He}$ respectively being the ionisation fractions of the intergalactic hydrogen and helium, and $Y_\mathrm{H} = 3/4$, $Y_\mathrm{p} = 1/4$ their respective mass fractions. The factor $\sqrt{\Omega_\mathrm{m}\,(1+z)^3+\Omega_\Lambda}$ encodes information about Λ cold dark matter (ΛCDM) cosmology[121]. We use the nine-year Wilkinson Microwave Anisotropy Probe (WMAP9) for cosmological parameter values, assuming flat ΛCDM cosmology [122]. We obtain z_S using equation (3.25), shown in figure 3.5. Except for the sources with high DM, the DM–z_S relation is approximately linear, and for our analysis, $z_\mathrm{S} \approx \langle \mathrm{DM_{exc}}(z_\mathrm{S})\rangle/1023\,\mathrm{pc\,cm^{-3}}$ holds, also depicted in figure 3.5. We include high DM FRBs considering their offsets from the linear relation described in [123]. CHIME/FRB team reported DM error bars based on `fit_b` algorithm [116], although future Very Long Baseline Interferometry (VLBI) observations will provide a better estimation for DM error values. For this analysis, we use average DM values for the redshift estimates. We further consider a lower cutoff of $\langle \mathrm{DM_{exc}}(z_\mathrm{S})\rangle$ at $117\,\mathrm{pc\,cm^{-3}}$, however the results are robust to the choice of cutoff. Moreover, these z_S values, derived using equation (3.25), are based on the measured average DMs; the true redshifts for some of these sources can be different from these estimated numbers depending on variations in the line of sight IGM, foreground galaxies if any or different host galaxy contributions.

Once we obtain τ for one FRB using equation (3.24), we can compute the integrated optical depth $\bar{\tau}$ considering all of the FRBs. If we know the redshift distribution function $N(z_\mathrm{L})$, it is

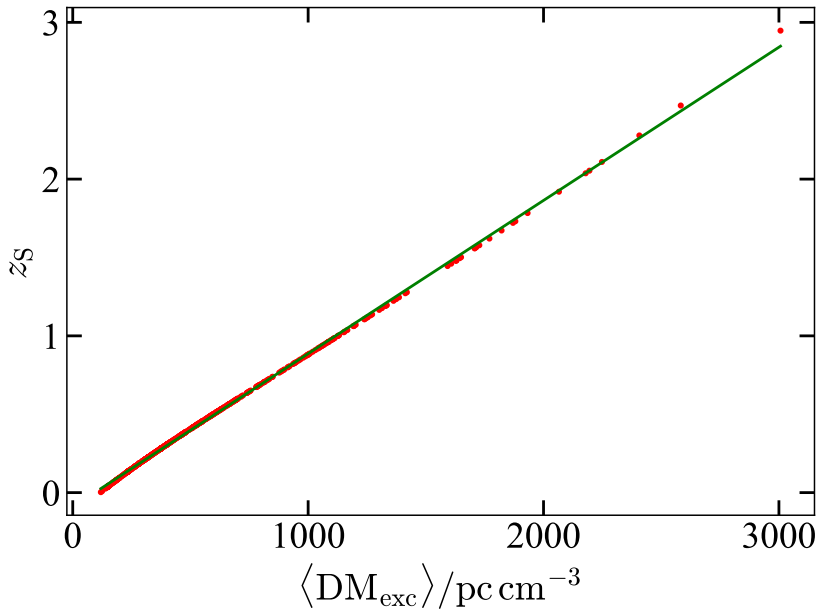

Figure 3.5 Source redshift as a function of average excess DM for the reported CHIME/FRB data sample shown in red dots. The green solid line is the best-fitted linear approximation with $z_\mathrm{S} \approx \langle \mathrm{DM_{exc}}(z_\mathrm{S}) \rangle / 1023\,\mathrm{pc\,cm^{-3}}$.

given by

$$\bar{\tau}(M_\mathrm{L}) = \int \tau(M_\mathrm{L}, z_\mathrm{L}) N(z_\mathrm{L})\,\mathrm{d}z_\mathrm{L}\,. \tag{3.29}$$

Previous works [78, 80, 82] used to consider different redshift distribution functions such as constant-density redshift distribution [124] or star-formation redshift distribution [125]. The constant-density redshift distribution is based on the assumption that FRBs have a constant comoving number density while the latter assumes that the FRBs follow the star-formation history. However, a recent result using the CHIME/FRB dataset suggests that $N(z_\mathrm{L})$ does not follow these distributions [126]. Moreover, we no longer require such an assumption because we now have data on a significant number of FRBs. Hence, we rather simply use the following discretized definition for the integrated optical depth

$$\bar{\tau} = \frac{1}{\mathcal{N}_\mathrm{FRB}} \sum_{i=1}^{\mathcal{N}_\mathrm{FRB}} \tau(M_\mathrm{L}, z_{\mathrm{S},i}), \tag{3.30}$$

where $\mathcal{N}_\mathrm{FRB}$ is the number of FRBs in the data sample to be considered.

Since the lensed FRBs $\mathcal{N}_{\rm lensed,FRB}$ are expected to be quite small in number in comparison to the total number of FRBs, one can safely use Poisson statistics to obtain the following relation [80]

$$\mathcal{N}_{\rm lensed,FRB} = \left(1 - e^{-\bar{\tau}}\right) \mathcal{N}_{\rm FRB}. \tag{3.31}$$

Owing to the fact that no lensed FRB has been confirmed so far, using the above relation, we obtain

$$f_{\rm PBH} < \frac{1}{\tau_1} \ln\left(\frac{\mathcal{N}_{\rm FRB}}{\mathcal{N}_{\rm FRB} - 1}\right), \tag{3.32}$$

where $\bar{\tau} = f_{\rm PBH}\tau_1$. In the limit $\mathcal{N}_{\rm FRB} \gg 1$, this relation reduces to $f_{\rm PBH} < 1/(\tau_1 \mathcal{N}_{\rm FRB})$.

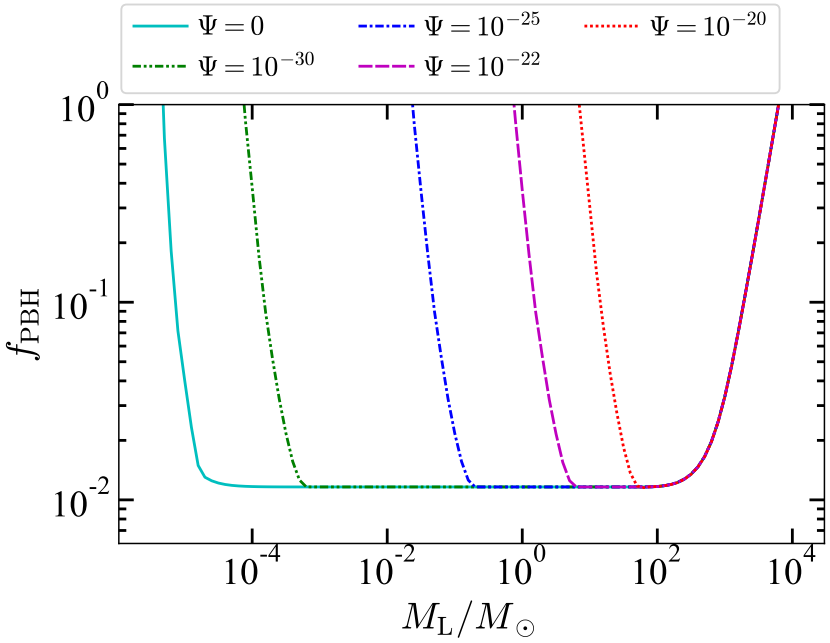

Figure 3.6 Bounds on the fraction of dark matter made up of primordial black holes for different values of modified gravity parameter Ψ in the unit of cm^{-2}.

Figure 3.6 shows the bound on $f_{\rm PBH}$ using the CHIME data for different modified gravity parameters. It is evident that as the value of Ψ increases, the bound is changed considerably. The left cut-off of each curve is determined from the minimum Δt of the telescope, which is approximately 10^{-9} s for the CHIME telescope. The cut-off on the right side of each curve is determined from the maximum magnification ratio μ, which essentially indicates if the dimmer image is detectable along with the brighter one. In this work, we choose $\mu = 1/3 \times$ S/N following [79]. For a certain lens mass, we obtain that $f_{\rm PBH}$ increases as Ψ increases. In other

words, the bound on $f_{\rm PBH}$ gets weaker with the increase in the modified gravity parameter. The modified gravity parameter Ψ is constrained for various modified gravity models. The ongoing New Horizons mission in the outskirts of our solar system is providing extended radio-tracking data, which gives $|\Psi| \lesssim 10^{-49}\,{\rm cm}^{-2}$ [127]. It is important to note that these findings are highly dependent on the specific experiment and can vary with each observation. Different bounds on Ψ were discussed in [128, 129] and found a much-relaxed bound with up to $|\Psi| \lesssim 2 \times 10^{-24}\,{\rm cm}^{-2}$. This clearly shows the chameleon effect [113, 114] is present and the effective values could be very different at different length scales. In this work, we show how the bound on the fraction of dark matter made up of primordial black holes changes with changing Ψ. The exact values are not very important, rather the effect itself is what we hope to exemplify.

3.6 Discussion and conclusion

The use of gravitational lensing to study modified gravity is not new, but it has not been studied in great detail from its timing perspective. Some properties of gravitational lensing was studied under $f(R,T)$ [130] and Horndeski theories [131]. Moreover, a ray-tracing approach was utilized to construct weak lensing maps from the simulated light cones, enabling the examination of weak lensing effects under different gravity conditions [132]. More recently, using the SgrA* and M87* black hole shadow observations, some modified gravity parameters have been constrained and thus a case is made that modified gravity can be distinguished from GR by analyzing lensing observables in the strong gravity regime [133].

In this work, we have studied gravitational lensing with a simple modified gravity metric. We have considered the SdS metric with Ψ being the modified gravity parameter and thereby obtained the differential time delay between the two lensed images. Note that we have only considered the case of strong lensing where multiple images can be formed. We have found that for the two lensed images, the time difference between these two rays to reach the observer is reduced as the strength of modified gravity increases. We further use this expression to constrain the fraction of dark matter that is made up of primordial black holes using the observed CHIME FRBs. We have considered 636 FRBs and using their reported excess DM values based on the NE2001 model, we have estimated redshifts of the sources, which we further utilize to obtain their integrated optical depths. Finally, we have obtained the $f_{\rm PBH}$ bound and found that for a given mass, this bound gets weaker as the strength of modified gravity increases.

It was previously established that $f_{\rm PBH}$ bound gets weaker as the lensing due to intergalactic plasma is taken into account [82]. This means that the lensing due to modified gravity acts similarly to plasma lensing, introducing decoherence to the signal. If any astronomical survey shows a deficit of plasma in the direction of an FRB, modified gravity can certainly make up for

it. This result will be improved by the Hydrogen Intensity and Real-time Analysis eXperiment (HIRAX), which will soon be able to detect a lot more FRBs in the Southern sky [37]. Similarly, other telescopes such as Deep Synoptic Array (DSA)-2000 [56] and Bustling Universe Radio Survey Telescope in Taiwan (BURSTT) [134] are expected to detect gravitationally lensed FRBs to obtain new constraints on $f_{\rm PBH}$. A more precise way of modifying the result is by considering a more appropriate metric using the Horndeski or Chameleon gravity following the recent astronomical and cosmological observations. In the future, if the intergalactic plasma contribution can be measured and if any lensing in FRBs is observed, these will help in effectively constraining the various modified gravity models and parameters.

4

Topological Data Analysis of FRBs

A particularly perplexing property of FRBs is that a relatively small subset of observed bursts have been observed to repeat. To date, no periodic repeaters have been found and the timescales between repetitions are varied, thus it is difficult to prove that all FRBs are not repeaters. This has led to speculation about two or more distinct populations of progenitors that give rise to these bursts [135–141].

In this chapter, we present a novel approach to analyse recent data from the Canadian Hydrogen Intensity Mapping Experiment (CHIME) collaboration on FRBs [142]. High-dimensional data, as encountered, presents a formidable challenge in various scientific domains, including astrophysics. Its inherent complexity arises from the inability to visually grasp its entirety, especially when it is noisy and incomplete. As the number of parameters or dimensions in a dataset grows, the volume occupied by the data expands exponentially, and, in the real world, where observations are limited, high-dimensional datasets often become sparsely populated. This phenomenon, often referred to as the "curse of dimensionality", poses a significant obstacle to extracting meaningful insights and organising data efficiently, a challenge rarely encountered in lower-dimensional settings. In addressing this challenge, one critical strategy is dimensionality reduction (DR), which aims to uncover essential low-dimensional structures within high-dimensional datasets. These low-dimensional representations facilitate visualisation and aid in the analysis and extraction of valuable information.

Effectively reducing dimensions can be transformative, shedding light on hidden patterns and relationships within the data. The most straightforward method of DR involves projection, which entails mapping the data onto lower-dimensional spaces. For instance, focusing on a subset of data features corresponds to a projection along specific axes. While this technique can reveal crucial insights, it may also obscure the true distances between neighbouring data points. Thus, the choice of projection is a pivotal step in the analysis. Principal Component

Analysis (PCA) is among the most prevalent DR techniques. PCA identifies linear combinations of original features, known as principal components, that capture the maximum variance in the data. This method has been widely employed for dimensionality reduction and visualisation. It simplifies complex data while preserving much of the data's inherent structure. In addition to PCA, several sophisticated DR algorithms have emerged, addressing the limitations of linear projections. Nonlinear iterative approaches, such as t-Distributed Stochastic Neighbor Embedding (t-SNE), Uniform Manifold Approximation and Projection (UMAP), and the recent Pairwise Controlled Manifold Approximation Projection (PaCMAP) [143], aim to uncover nonlinear relationships in the data. These methods preserve the closeness of data points, yielding low-dimensional representations that are rich in meaning and facilitate advanced analyses.

Extending and updating the results first reported in [144], we apply Topological Data Analysis (TDA) to the recent CHIME/FRB dataset, with a focus on repeating FRBs. TDA is a branch of applied mathematics that uses techniques from topology - the study of the shape and connectivity of spaces - to infer relevant features within the data from complex and high-dimensional data sets. Specifically, it provides tools to capture qualitative properties of data that are invariant under deformations. As such, TDA can reveal hidden patterns, clusters, and structures in data that are robust to noise and insensitive to the choice of metric.

We use the first CHIME/FRB catalogue, which contains 535 FRBs detected by CHIME between 25 July 2018 and 1 July 2019, including 62 bursts from 18 repeating sources supplemented with a repeater catalogue containing 146 bursts of 25 repeaters detected from 2019 September 30 to 2021 May 1. We use various features of FRBs such as luminosity and energy of the burst based on fluence (the integrated flux over time), intrinsic width (the duration of the burst after correcting for dispersion and scattering), spectral bandwidth (the range of frequencies over which the burst is detected), and frequency slope (the change in frequency over time) to parameterise the data space.

Our main goal is to use TDA to make predictions for where to find new repeaters among the FRBs detected by CHIME. We hypothesise that repeating FRBs have some distinctive topological features that can be captured by TDA. We aim to explore the similarities and differences between repeaters and non-repeaters in terms of their physical properties and their distribution in the sky. We hope that our analysis can shed some light on the nature and origin of FRBs and their possible applications to cosmology and fundamental physics.

4.1 Dimension Reduction Algorithms

4.1.1 Principle Component Analysis (PCA)

Principal Component Analysis (PCA) is a powerful statistical technique used for dimensionality reduction and data visualisation. It transforms a set of correlated variables into a smaller set of uncorrelated variables, known as principal components, which capture the maximum variance of the original data. PCA works by finding a set of orthogonal (perpendicular) axes in the high-dimensional space of the original variables. These axes are chosen such that the first axis captures the maximum variance, the second axis captures the maximum remaining variance, and so on. The principal components are then the projections of the original data onto these axes.

PCA can be broken down into five components [145], **Standardization:** The original data is first standardized to ensure that all variables have the same scale and variance. This is essential for preventing variables with larger scales from dominating the analysis. **Covariance Matrix:** The covariance matrix is calculated, which measures the relationships (correlations) between all pairs of variables **Eigenvalue Decomposition:** The covariance matrix is decomposed into its eigenvalues and eigenvectors. The eigenvalues represent the amount of variance explained by each principal component, and the eigenvectors define the directions of the principal components. **Principal Components:** The eigenvectors corresponding to the largest eigenvalues are selected, forming the principal components. These components capture the most significant patterns in the data. **Dimensionality Reduction:** The original data is projected onto the subspace defined by the chosen principal components. This reduces the dimensionality of the data while preserving as much information as possible.

PCA has a wide range of applications across various fields, including biology, ecology, and computer science. In biology, it is used to analyse gene expression data, identifying groups of genes that are co-expressed. Ecology utilizes PCA to analyse species abundance data, understanding how environmental factors influence species distribution. Computer science employs PCA for image compression, where it reduces the dimensionality of image data while preserving important features. PCA also plays a crucial role in recommender systems, where it predicts user preferences based on past interactions with items. Moreover, PCA is used for facial recognition, where it extracts key features from images for identification.

4.1.2 Uniform Manifold Approximation and Projection (UMAP)

Uniform Manifold Approximation and Projection (UMAP) is a dimensionality reduction technique that aims to preserve both local and global structure in data. It was introduced in 2018 by Leland McInnes, John Healy, and James Melville as a more scalable and robust

alternative to t-SNE. UMAP is based on a theoretical framework rooted in Riemannian geometry and algebraic topology. It works by constructing a fuzzy topological representation of the data, which captures the local neighborhood relationships and global connectivity of the manifold. UMAP [146] then optimises a low-dimensional layout of this representation to minimize the difference between the two topological structures. One of UMAP's key strengths is its ability to scale to large datasets. It has no computational restrictions on embedding dimension and is able to handle high-dimensional data more efficiently than t-SNE. Moreover, UMAP is more robust to noise and outliers than t-SNE, making it suitable for a wider range of applications. UMAP has found wide use in bioinformatics, materials science, and machine learning. It is used for visualization, clustering, anomaly detection, and as a pre-processing step for other machine learning tasks.

The key benefits of UMAP are: **Scalability:** UMAP can handle massive datasets with high dimensionality. **Robustness:** UMAP is robust to noise and outliers. **Preservation of Structure:** UMAP preserves both local and global structure in the data, making it suitable for a wider range of applications. **Speed:** UMAP is often faster than other dimensionality reduction techniques, particularly for large datasets.

While UMAP has many advantages, it also has some limitations. It lacks the interpretability of methods like PCA, and its performance can be sensitive to the choice of hyperparameters. Nonetheless, UMAP is a powerful and versatile tool that is well-suited for many dimensionality reduction tasks.

4.1.3 Pairwise Controlled Manifold Approximation Projection (PaCMAP)

Pairwise Controlled Manifold Approximation Projection (PaCMAP) is a novel algorithm for dimensionality reduction designed to preserve both local and global structure in the data. It leverages a carefully designed loss function and a dynamic choice of graph components to achieve this balance. PaCMAP incorporates three types of pairwise loss terms: 1) neighbour edges, which encourage attraction between neighbouring points; 2) mid-near edges, which aim to preserve global structure by attracting points that are moderately close but not neighbours; and 3) further edges, which push further points away, promoting separation between clusters.

The strengths of PaCMAP lie in its ability to handle both local and global structures without relying solely on one or the other [147]. It employs a three-stage dynamic optimization process to optimise both local and global structure, beginning by heavily weighting mid-near pairs to establish global structure early in the process. The weights on these mid-near pairs are gradually reduced, allowing the algorithm to refocus on local structure and refine the embedding in the latter stages. This adaptive approach ensures that PaCMAP doesn't sacrifice

one type of structure for the other and that both local and global information are captured in the low-dimensional representation.

PaCMAP's robustness is highlighted by its performance across various datasets, including those with predominantly local or global structures. It outperforms other algorithms on metrics like random triplet accuracy and centroid triplet accuracy, which measure global structure preservation, while also demonstrating competitive performance on local structure metrics such as KNN and SVM accuracy. This demonstrates its ability to effectively preserve both local and global structure in a balanced manner. Another key aspect of PaCMAP's effectiveness is its computational efficiency. It uses a simpler loss function and avoids the need for triplets, resulting in faster training times and making it suitable for large-scale datasets. The algorithm also shows good robustness to initialization, with its performance remaining consistent even with random initialisation.

Compared to other algorithms like t-SNE, UMAP, and TriMap, PaCMAP demonstrates a superior ability to preserve both local and global structures. t-SNE tends to distribute data uniformly, potentially hindering global structure preservation. UMAP focuses primarily on local structure, while TriMap's performance relies heavily on initialization. PaCMAP's dynamic approach to graph components and its inclusion of mid-near pairs address the shortcomings of these other algorithms, allowing it to effectively capture both local and global structures. In essence, PaCMAP offers a promising approach to dimensionality reduction that balances local and global structure preservation. Its innovative loss function, dynamic graph component selection, and computational efficiency make it a powerful tool for data visualisation.

4.2 Topological Data Analysis

Within the domain of TDA, Persistent Homology and the Mapper algorithm represent two major tools to explore the shape of a dataset, each with distinct foci and applications. A broad outline of how these two algorithms work is given below.

4.2.1 Persistent Homology

Persistent homology operates on the fundamental concept that topological features, such as connected components (0-dimensional), loops (1-dimensional), or voids (2-dimensional), can persist across different levels of granularity. Figure 4.1 depicts an example of persistent homology with three points and feature generation over ε based on the steps described below. The algorithm focuses on capturing features that persist and evolve as the filtration parameter changes, making it particularly suitable for understanding the global topological characteristics of data. It proceeds as follows:

- **Filtration:** The process begins by constructing a simplicial complex from the data points. A simplicial complex is a mathematical representation of topological features. The filtration, a continuous parameter like distance or radius, gradually increases, considering data points in an ascending order of this parameter.
- **Complex Evolution:** As the filtration parameter increases, new simplices (vertices, edges, triangles, etc.) are added to the complex. This process mimics the "growing" of topological features.
- **Tracking Birth and Death:** Persistent homology keeps track of when these topological features are "born" and "die" as the filtration parameter increases. A feature is born when it first appears in the complex, and it dies when it merges or disappears.

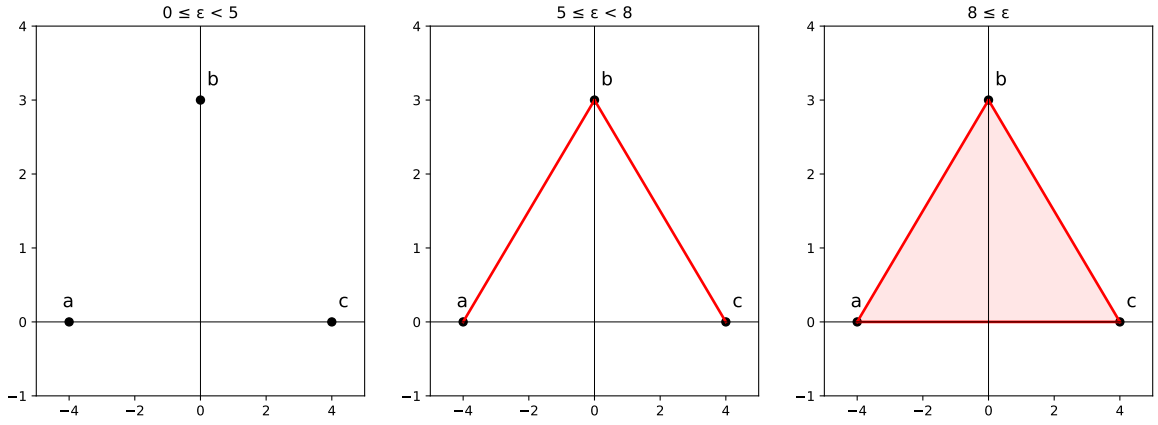

Figure 4.1 The graph display an example of persistent homology of three distinct regions corresponding to different ranges of ε. For $0 \leq \varepsilon < 5$, is represented by a single point 'a' at position (-4, 0). When $5 \leq \varepsilon < 8$, Y(ε) forms a line segment connecting points 'a' and 'b' where 'b' is located at (0, 3). Finally, for $\varepsilon \geq 8$, Y(ε) represents a triangle formed by connecting points 'a', 'b', and 'c' where 'c' is positioned at (4, 0). This representation visually highlights the transformation of Y(ε) from a single point to a line segment and ultimately to a triangle as ε increases.

To represent this persistence of topological features, persistent homology uses visual tools like *persistence diagrams* or *barcodes*. A persistence diagram is a scatter plot with birth on the x-axis and death on the y-axis. Each point on the diagram corresponds to a topological feature (connected component, loop, void). The horizontal position of a point indicates when the feature is born, and the vertical position represents when it dies.

4.2.2 The Mapper Algorithm

The second major tool in the TDA framework is the Mapper algorithm that, like Persistent Homology, facilitates the exploration and representation of the shape and structure of complex data. Unlike Persistent Homology, which focuses on capturing topological features across different resolutions, Mapper offers a different approach that can be summarised as follows:

- **Dimensionality Reduction:** Mapper begins by mapping high-dimensional data to a lower-dimensional space using a filter function or lens. This filter function can be based on various techniques like projecting data onto principal components or estimating data density. The goal is to simplify the data while retaining its essential characteristics.
- **Cover Construction:** In this step, Mapper constructs a cover of the lower-dimensional projected space. This cover is formed by dividing the space into overlapping intervals or hyper-balls of constant size. The choice of intervals or balls depends on the specific dataset and the problem being analysed.
- **Clustering:** Within each interval or ball, Mapper applies a clustering algorithm of choice to group data points that are close to each other. Common clustering methods like k-means or DBSCAN can be used. This step aims to identify local patterns or clusters within the data.
- **Simplicial Complex:** Finally, Mapper builds a simplicial complex, which is a network composed of nodes and edges. Each cluster from the previous step corresponds to a node in the complex, and edges are established between clusters that share some common data points. This connectivity reveals the relationships between clusters and captures the global and local structure of the data.

While each is useful in its domain, Mapper's approach of overlapping bins or intervals ensures local connectivity in the representation of data. This allows for a detailed exploration of clusters and patterns at various scales, making it suitable for analysing complex datasets. Identifying separate disconnected clusters or regions in the mapper graph can reveal different populations or distinct structures within the dataset.

4.3 Fast Radio Bursts and Their Intrinsic Properties

Observable quantities associated with FRBs contain information about the nature of the source, effects associated with propagation to the observer, and the instrument used to detect them. Notable among FRB observables is the dispersion measure (DM), which we further use to calculate luminosity and energy of the burst described introduced in Equation 1.2 and further

explained in Equation 3.25, 3.27, 3.28. These expressions can provide a crude proxy for distance to the source. By neglecting the host galaxy contribution to the observed DM, and subtracting off the relatively well-modelled Milky Way contribution, one can use Equation 3.27 to place an upper limit on the redshift of the FRB. This does not give accurate redshift measurements and overestimates the distances by not including the host galaxy and foreground galaxy distributions, if any.

Once the redshift of a source is known, observed frequencies (and bandwidths) can be converted to their rest-frame values using the standard expression,

$$\nu_{\rm rest} = \nu_{\rm obs}(1+z), \tag{4.1}$$

where $\nu_{\rm rest}$ is the rest-frame frequency, and $\nu_{\rm obs}$ is the observed frequency.

Another important observable associated with FRBs is their spectral flux density, S_ν. This contains information on the energetics of the source, together with propagation and detection effects. By assuming isotropic emission, and the inverse square law, one can approximate the intrinsic spectral luminosity as [148, 149]

$$L_p \sim 4\pi D_L^2(z) S_\nu \nu \,. \tag{4.2}$$

Similarly, the total radiative energy emitted by a source can be determined using [148, 149]

$$E \sim \frac{4\pi D_L^2(z)}{(1+z)} F_\nu \nu \,. \tag{4.3}$$

In these equations, $D_L(z)$ represents the luminosity distance, while S_ν denotes the average flux values. Using equations 4.2- 4.3 with the approximate redshifted given by Equation 3.27, produce crude upper limits on intrinsic source properties since contributions from cosmic inhomogeneities and the FRB host galaxy are neglected. We use the central frequency of emission with the reported peak frequency interchangeably for energy calculations. This assumption is valid as CHIME/FRBs have well-defined peak frequencies for a Gaussian-like spectral shape. In addition, the frequency cutoff described in Section 4.4 removes bursts that have central emission frequencies outside the receiver band. These expressions will suffice for our purposes since TDA is known to perform well in the presence of noise, and we will be using an FRB catalogue which does not contain redshift information.

4.4 Description of the Data

The initial release of the CHIME/FRB catalogue comprised 536 bursts (or sub-bursts in case of multiple burst reception), categorised into two groups: 474 bursts are considered apparent

Intrinsic Burst Properties	Description
width_fitb	upper limit sub-pulse width by `fitburst`
sp_idx	spectral index of the sub-burst
sp_run	frequency dependency of spectral shape
restframe_peak_freq	peak frequency of the pulse in MHz at FWTM*
restframe_bw	bandwidth obtained from `high_freq` a `low_freq` at FWTM*
log_E	energy values of the burst
log_Lp	luminosity of the the burst

Table 4.1 CHIME/FRB catalogue parameters included in this analysis, together with the derived "rest frame" parameters. (*Full Width at a Tenth Maximum)

non-repeaters, while the remaining 62 bursts are associated with 18 repeating sources [150]. For each CHIME/FRB catalogue burst, there are ~ 30 observable parameters reported. Some of these, such as the DM, scattering time, spectral shape, bandwidth, flux, and pulse width, are closely related to astrophysical processes. In contrast, others, such as the Signal-to-Noise Ratio (SNR) and positions on the sky etc., are more biased to their detection at the instrument. Since we aim to construct a dataset which reflects the intrinsic properties of FRBs in their rest frame, uncontaminated by propagation and instrumental effects, we use only a subset of those provided in the catalogue and derive approximate rest-frame quantities for each burst. We use the reported extragalactic DM to approximate the redshift according to Equation 3.27, and with this, we compute the isotropic luminosity using Equation 4.2 and isotropic energy using Equation 4.3. In addition, we shift all measured frequencies (and bandwidths) to their rest-frame values. A summary of the parameters we include in our dataset is shown in Table 4.1.

To enhance data reliability and mitigate unwanted biases arising from instrumental effects, we apply further cuts to the catalogue. In particular, we exclude bursts with low SNR. We also exclude low-DM bursts from the sample, as these may be dominated by Milky Way subtraction and host galaxy uncertainties. We exclude bursts with peak frequencies falling outside of the $400 - 800$ MHz band since we use these values to compute the rest-frame luminosity and energy.

1. SNR > 12
2. DM $> 1.5 \max(DM_{\rm NE2001}, DM_{\rm YMW16})$
3. $400.1 \leq \nu_{\rm peak} \leq 799.9$ MHz

Once these cuts have been applied, we are left with 584 bursts in the sample, of which 185 are flagged as repeaters. To ensure accuracy, we utilise more precise `fitburst` values calculated

offline for SNR, DM, and pulse width, as real-time measurements often come with larger error bars due to limited time resolutions within the receiver system.

Since the features in our dataset have vastly different ranges, we apply a prepossessing transformation to avoid the need for a non-Euclidean metric in the clustering algorithm employed by mapper. Various transformations were explored. We found that most linear preprocessing methods yielded comparable clustering outcomes for repeaters and non-repeaters. We opted for `StandardScalar`, which scales all data features such that they have zero mean and unit variance. For further detail on the choice of prepossessing transformation, see the Appendix for further in the formation of mappers.

4.5 Results

We apply the TDA methods described in Section 4.2 to the FRB dataset described in Section 4.4, using the Python packages `ripser` [151], and `kepler-mapper` [152].

Singly connected components - loops - cavities - and hypercubes in TDA provide a localised view of data density whereas the Betti numbers offer a more global perspective on the data's overall shape and connectivity. The persistence diagram (Figure 4.2, left panel) depicts the birth and death timescales of the first two homology groups, H_0 (black) and H_1 (red). A horizontal line segment (dashed line) signifies that a topological feature persists indefinitely. Therefore, this diagram visualises how long each topological feature persists across different scales within the parameter space defined in Table 4.1. The persistence diagram here reflects the presence of noise CHIME/FRB catalogues. Note that in particular, two H_0 points persist over a large range of scales (birth 0, death >5.5). Distances in data space are filtered with the evolution of the $epsi$ threshold parameter during the filtration process. We believe that the TDA diagram on the right-hand side of Figure 4.2 is placed within the range between 5.5 and 10. Given our high-dimension noisy data, over the scales of 0 to 4, there exist multiple nuisances H_0 and H_1 points i.e. connected components and one-dimension loops or circles because of the noise in the data and not significant. However, these topological features above the value of 5.5 are robust to perturbations in the data and are distinct from the features that only persist below the value of 4. The persistence diagram lends support to our observation about three distinct groups, since the mapper result is quite sensitive to the choice of hyperparameters (scale), whereas persistent homology tells us about structures across a range of scales and filtration values, and is a compact representation of the global geometry of the data. Note also the absence of any persistent H_1 groups in our data that indicates an absence of any loops in the data.

On the right panel of Figure 4.2, we show the distribution of repeaters and apparent non-repeaters in seven-dimensional parameter space. We see three distinct connected components, green coloured dominated by apparent non-repeaters, red coloured dominated by repeaters

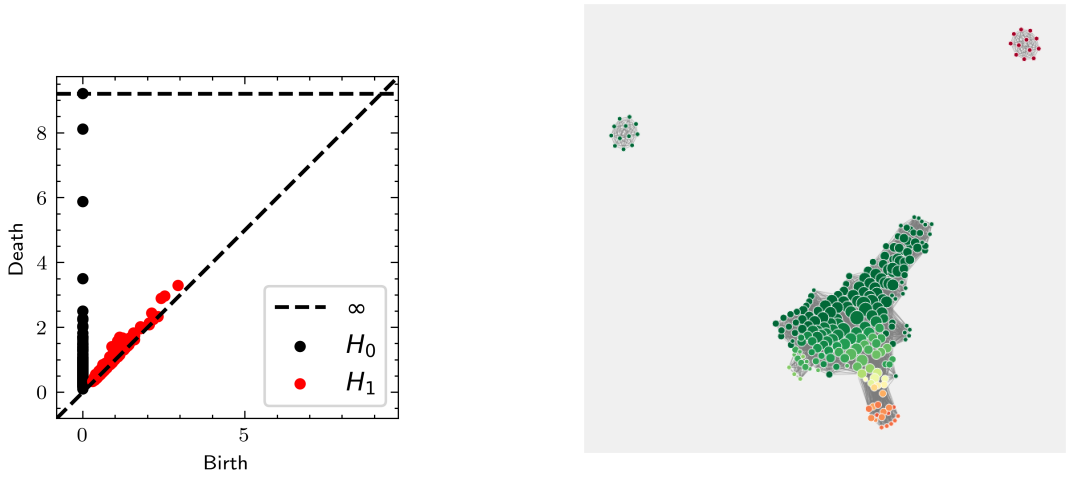

Figure 4.2 The persistence diagram (left) and mapper output (right) for the rest-frame FRB datasets described in Section 4.4. The persistence diagram shows the birth and death of the first two homology groups, H_0 (black) and H_1 (red). The mapper output depicts clusters of repeaters and apparent non-repeaters. The size of each node is proportional to the number of FRBs it contains, coloured-coded according to the faction of repeaters.

and a bigger cluster that hosts both categories. This clustering arrangement gives us a few non-repeaters in the proximity of repeating FRBs. Hence, our analysis identifies apparent non-repeaters that potentially share characteristics with repeaters. These candidates are situated in nodes where more than half of the elements are repeaters. We designate such a node as a "repeater node". For instance, we find that single-burst candidates grouped with higher SNR values tend to exhibit higher energy levels and are more amenable to follow-up observations, thus falling into repeater nodes. The repeater nodes are marked with warm red-toned colours in the right panel of Figure 4.2.

As demonstrated in Figure 4.5 in Appendix 4.7, clustered groups exhibit varying characteristics based on different parameters. Specifically, separate clusters are observed to have low spectral running and low bandwidth. Conversely, repeaters are discerned by higher spectral indices, narrower bandwidth, and lower SNR. We find that there exists a subgroup among repeaters characterised by high SNR but relatively lower luminosity and spectral running.

Further analysis uncovers that among the repeater candidates, FRB20190430C was initially identified as single-burst FRBs but were later found to exhibit repeating behaviour in the CHIME/FRB 2023 catalogue [116]. Based on our simulations, we identify FRB20181221A, along with the candidates listed in Table 4.2, as intriguing candidates warranting further investigation for repeater characteristics. To validate our findings, we confirm the clustering patterns

of repeaters and non-repeaters within the mapper by projecting known repeater candidates back into two-dimensional PCA projections. This analysis effectively corroborates that all repeater candidates exhibit similar properties to those of known repeaters, as evidenced in Figure 4.4. Proposed repeater candidates in the figure are marked in blue, with red denoting known repeaters and black are apparent non-repeaters.

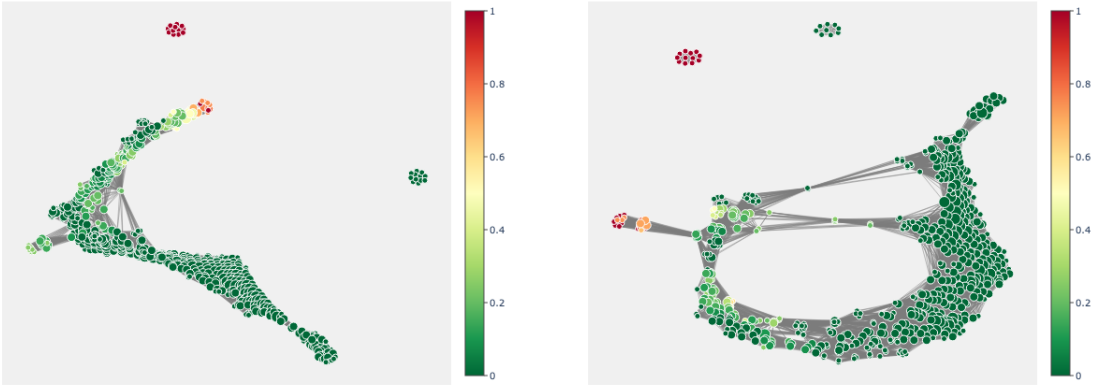

Figure 4.3 The persistence diagram (left) and mapper output (right) for the rest-frame FRB datasets described in Section 4.4. The mapper outputs for UMAP(left) and PacMAP(right) as filter/lens depict clusters of repeaters and apparent non-repeaters similar to Figure 4.2. The size of each node is proportional to the number of FRBs it contains, coloured-coded according to the faction of repeaters.

We have projected all parameters for repeaters published by CHIME so far to PCA filter as shown in the top panel of Figure 4.4 in Appendix 4.7. The similar colour coding in the lower panel of Figure 4.4 multiple bursts from one repeater source. This analysis includes multiple bursts from 2021 and 2023 repeater sources. We argue that the repeaters themselves do not have any preferences in the parameter space. We have not performed mapper analysis for only the repeater dataset yet and await more bursts for better estimations.

4.6 Discussion and Summary

In this paper, we have applied topological data analysis (TDA) to study the properties of fast radio bursts (FRBs) detected by the CHIME/FRB experiment. We have used the mapper algorithm to construct networks that capture global shape of parameter space. We have focused on the repeater and non-repeater populations. Our main findings are:

Lens/Filter	Repeater Candidates
PCA	FRB20181129B, FRB20181017B, FRB20181213B, FRB20190112A, FRB20190218B, FRB20190228A, FRB20190403G, FRB20190422A, FRB20181128C, FRB20181203B, FRB20190129A, FRB20190621C
UMAP	FRB20181017B, FRB20190422A, FRB20181129B, FRB20181203B, FRB20190112A, FRB20190218B, FRB20190228A, FRB20190430C, FRB20190125A, FRB20190129A, FRB20181213B
PaCMAP	FRB20181017B, FRB20181129B

Table 4.2 Repeaters candidates from different algorithms

- The bursts from three distinct clusters in the mapper networks are based on their inferred source properties. One of these clusters contains the majority of, and is exclusively associated with, repeating bursts.
- The repeater population can be further divided into three sub-groups based on clustering shown in Figure 4.2 and Figure 4.5. One subgroup is Based on their spectral properties ie spectral index, spectral running and bandwidth, luminosity and energy these sub-groups may hint at different types of mechanisms that produce repeating FRBs.
- The PCA projections and mappers do not reveal any clear trend or dichotomy among the repeaters themselves, therefore we conclude the repeater properties do not seem to depend on the given intrinsic parameter space in the 2023 catalogue.

Most repeaters in our dataset exhibit larger `bc_width` and narrower `bw`. Presuming these repeaters share characteristics with FRB 121102 and reside in dense circumgalactic environments, we anticipate them to exhibit extended scattering times (large `scat_time`). Alternatively, a substantial fraction of the anticipated repeaters may display significant scattering times. Previous studies on CHIME/FRB have employed dimensionality reduction algorithms, such as UMAP and t-SNE, to achieve clustering and classification of the CHIME/FRB catalogue2021[138, 140]. Unlike the higher compute load of tSNE, UMAP is built on the mathematical concept of topology but projects the data on a lower dimension introducing information loss. [141] leverages clustering algorithms like k-means and DBSCAN in conjunction with a dimensionality reduction (DR) technique for analysis. Whereas, this paper provides an alternate perspective on the CHIME catalogues with mapper and persistence homology diagrams. To facilitate a comparative analysis between our findings and those derived from the the previous analysis, we employed these dimensionality reduction (DR) algorithms as complementary analytical lenses to our simulation in addition to PCA. Similar to PCA, mappers with UMAP and PacMAP filters have three connected components as shown in Figure 4.3, however,

the number of repeater candidates is different and lower in UMAP and PacMAP as shown in Table 4.2. We expect these differences as projections of PCA, UMAP and PacMAP show different proximities in the parameter space. We observe a loop in the mapper with PaCMAP projection as shown in the right-hand side of Figure 4.3 that is a consequence of PacMAP projection. However as PCA and UMAP filters do not show loops, we are currently debating on this, and more data will help determine if it is a noisy feature. Our analysis identified one potential repeater candidate overlapping with those reported in [140, 141]. Additionally, seven candidates were identified within existing repeater catalogues.

We conclude that TDA is a powerful tool to explore the diversity and complexity of the FRB phenomenon. It can help us to identify and classify different populations and sub-populations of FRBs, and to reveal their intrinsic and extrinsic features. We suggest that future studies should apply TDA to larger and more complete FRB samples, and incorporate other parameters such as polarisation, dispersion measure and rotation measure. The TDA algorithms have a larger scope of applications with different transient objects and cosmological parameter estimations such as pulsars and cosmological parameter estimation. We recommend that follow-up observations of the repeater candidates should be conducted to verify their nature and origin.

4.7 Mapper plots with observed parameters

To ensure the robustness of our mapper generation process and prevent numerical extremes, we employ the standardscaler transformation shown in the top panel of Figure 4.4. This transformation effectively centres the data, giving it an average value of zero and a standard deviation of one. In our evaluation, we have compared standardscaler with various other preprocessing techniques, aiming to assess their impact on clustering results. Notably, we observed that most linear preprocessing methods yielded comparable clustering outcomes for repeaters and non-repeaters.

As illustrated in the top panel of Figure 4.4, this assessment of preprocessing techniques was conducted on a seven-dimensional dataset that was subsequently projected onto a two-dimensional space. The PCA analysis is a dimensionality reduction technique that finds the principal components of the data, which are the directions of greatest variance. The first principal component (pca1) explains the most variance in the data, followed by the second principal component (pca2), and so on. It is worth highlighting that linear scaling algorithms such as standardscaler introduce a discernible separation between a repeater and apparent non-repeater clusters. The once-off bursts are more spread out across the plot, which suggests that they are more diverse. While the lower panel of Figure 4.4 depicts confirmed repeaters,

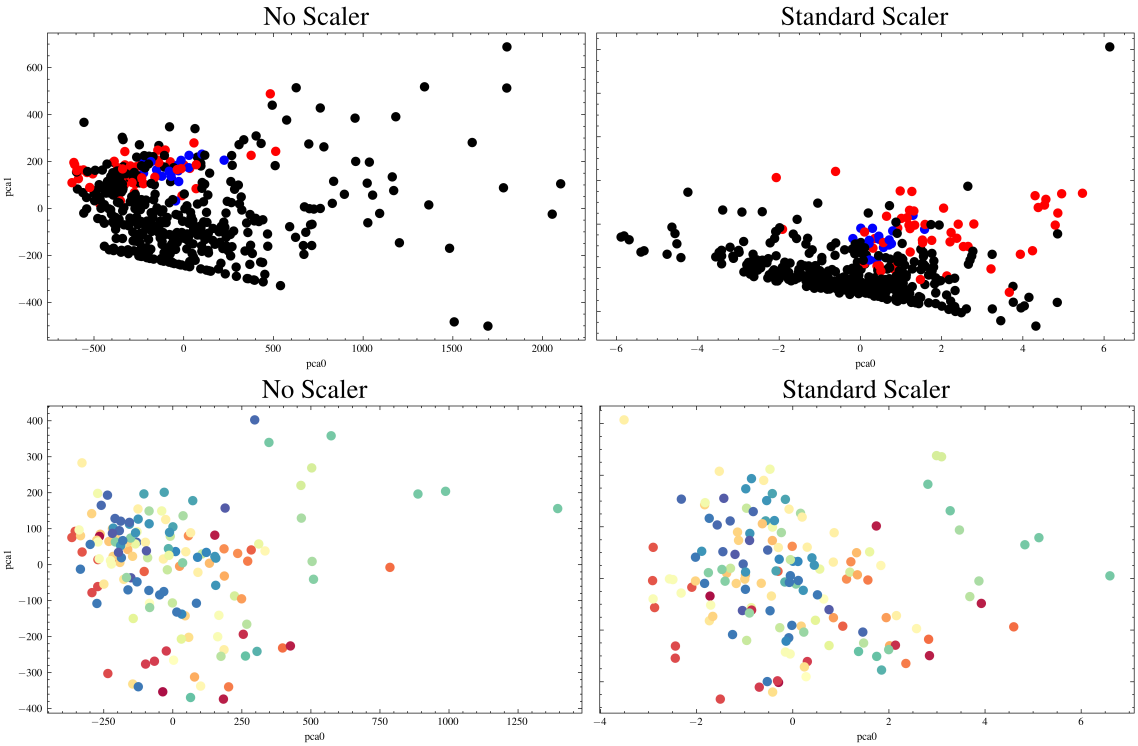

Figure 4.4 Top panel: PCA projection of the data described in Section 4.4, for two preprocessing transformations. Once-off bursts are shown in black, repeaters in red, and repeater candidates in blue. Lower panel: PCA projection of only repeaters, for two preprocessing transformations. A total of 39 repeaters are colour-coded and projected in PCA for parameters described in Table 4.1.

their distribution appears relatively uniform within the parameter space. This suggests minimal inherent clustering tendencies based on repeater data in the current PCA projection. This suggests that these objects are similar to each other in terms of their properties. However, incorporating additional repeater data in future analyses has the potential to reveal more distinct clustering patterns. Overall, the current PCA projection using only repeaters provides valuable initial insights, and further data acquisition can enhance our ability to identify potential clusters.

As in our detailed analysis in Section 4.5, in this appendix, we unveil the intricate behaviours of crucial observational parameters within the identified clusters. These parameters are dispersion measure, spectral shape metrics including spectral index and spectral running, bandwidth, pulse width, and scattering time within the context of clustered phenomena. Notably, our examination uncovers discernible variations in luminosity and energy magnitudes within clusters of repeaters, shedding valuable light on the complex dynamics and characteristics of these intriguing astrophysical entities.

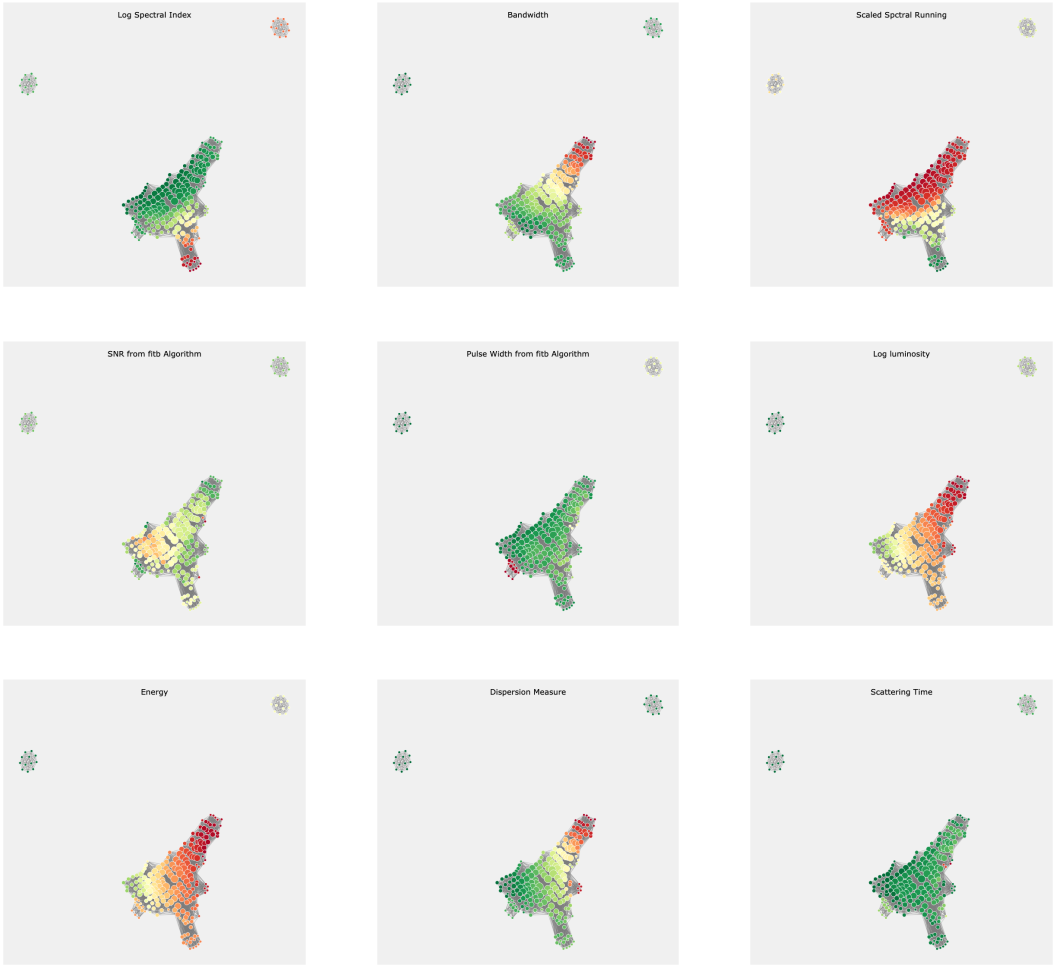

Figure 4.5 mapper output coloured by catalogue parameter values

The Figure 4.5 shows the output of a mapper algorithm, which is a topological data analysis technique that can be used to visualize and understand complex datasets. The mapper algorithm constructs a simplicial complex, which is a mathematical object that represents the topology of the data. The simplicial complex is then visualized as a graph, with the nodes of the graph representing the clusters of data points and the edges of the graph representing the relationships between the clusters. In this figure, the mapper algorithm was applied to a dataset of simulated gravitational wave signals. The dataset is characterized by a number of different parameters, such as the log spectral index, bandwidth, SNR from `fitb` algorithm, energy, pulse width from `fitb` algorithm, log luminosity, dispersion measure, and scattering time. The figure shows the mapper output for each of these parameters, colour-coded to indicate the values of the parameter. The figure shows that the mapper algorithm can effectively capture the topological structure of the data. For example, the figure shows that the data points with higher log spectral indices tend to be clustered together, while the data points with lower log spectral indices tend to be scattered more widely. The figure also shows that the data points with higher bandwidths tend to be clustered together, while the data points with lower bandwidths tend to be scattered more widely. Overall, the figure demonstrates the power of the mapper algorithm for visualizing and understanding complex datasets. The algorithm is able to effectively capture the topological structure of the data, which can be used to identify patterns and insights that might not be apparent from simply looking at the raw data.

5

Input Data Processing and Analysis of MeerTRAP FRBID Classifier

Discriminating Fast Radio Bursts (FRBs) from terrestrial radio frequency interference (RFI) poses a significant challenge in observational astronomy. This difficulty arises from the requirement for continuous, high-sensitivity surveys that cover a large FoV of the sky. To address this challenge, the MeerTRAP commensal project was developed. The MeerTRAP pipeline is designed to search for transients and pulsars in the radio sky. It utilizes the excellent sensitivity and sky coverage of the MeerKAT telescope to detect these objects. The pipeline consists of two main components: a coherent search and an incoherent search.

The coherent search uses the core dishes of MeerKAT to achieve maximum sensitivity. The separation of the dishes results in a coherent beam with a small FoV, however, MeerTRAP uses 400 beams for a total FoV of 0.1 square degrees. The incoherent search uses the sum of the 64 dishes, which results in a lower sensitivity but samples the entire 1.27 square degree FoV of a MeerKAT dish. Both searches are essential for detecting dispersed fast radio transients in real-time, allowing for rapid follow-up observations. The pipeline uses a coherent beam localisation method to give (sub)arcsecond positions within a few seconds for bright transients. Once a burst is detected, a transient buffer captures up to 30s of data, allowing for the localisation of transients detected with dispersion measure of at least 3000 pc cm-3 (redshifts beyond 2). This buffer includes enough time for processing and triggering.

Coherent mode involves combining the signals from the dishes in phase, which results in maximum sensitivity. However, the separation of the dishes results in a coherent beam with a small field of view. To increase the field of view, MeerTRAP will use 400 beams, each with a field of view of 0.00025 square degrees, which will provide a total field of view of 0.1 square degrees [153].

Incoherent mode, on the other hand, involves summing the intensities of the signals from the dishes, resulting in a lower sensitivity but samples the entire 1.27 square degree field of view of a MeerKAT dish. The coherent mode is more sensitive and can provide more precise localisation of transients, while the incoherent mode can sample a larger field of view. The choice of mode depends on the specific scientific goals of the observation. For example, if the goal is to detect a large number of pulsars, the incoherent mode would be more suitable as it can cover a larger area of the sky. However, if the goal is to detect a specific transient with high precision, the coherent mode would be more suitable as it provides higher sensitivity and better localisation.

The MeerTRAP pipeline also incorporates optical observations with the MeerLICHT telescope. This 65-cm aperture telescope is matched to the MeerKAT FoV and continuously points at the same location in the sky, providing simultaneous optical and radio data. This allows for the search for prompt and afterglow emission, as well as for the mining of the rich multi-wavelength data available for many MLSP fields. Following the initial detection stage, a state-of-the-art machine learning algorithm, the FRBID (Fast Radio Bursts Intelligent Distinguisher) is employed for post-processing. FRBID tackles the critical task of classifying single radio pulses, differentiating between FRBs, known astrophysical sources like pulsars and Rotating Radio Transients (RRATs), and various forms of noise and RFI, collectively referred to as N-RFI [154].

The vast number of transient radio source candidates identified by pipelines such as MeerTRAP presents a significant challenge for human analysis. Visual inspection of this immense data volume becomes impractical due to sheer quantity. To address this bottleneck, advanced machine learning classification techniques offer a powerful solution. These algorithms can significantly reduce the human workload associated with candidate classification, enabling real-time detection and triggering of observations for promising FRB candidates. The FRBID algorithm [154] exemplifies such a machine learning approach, serving as a crucial component of the MeerTRAP pipeline.

5.1 Single Pulse Classification with Machine Learning

The MeerTRAP signal processing pipeline yields a substantial output of candidate pulses encompassing a range of DM. However, this data also includes a significant number of noise and RFI events mimicking single pulses. The sheer volume of such detections necessitates the adoption of machine learning techniques for efficient analysis. Machine learning excels at pattern recognition tasks involving large datasets, precisely the scenario encountered with MeerTRAP data. Given the availability of extensive training samples, MeerTRAP leverages supervised learning algorithms.

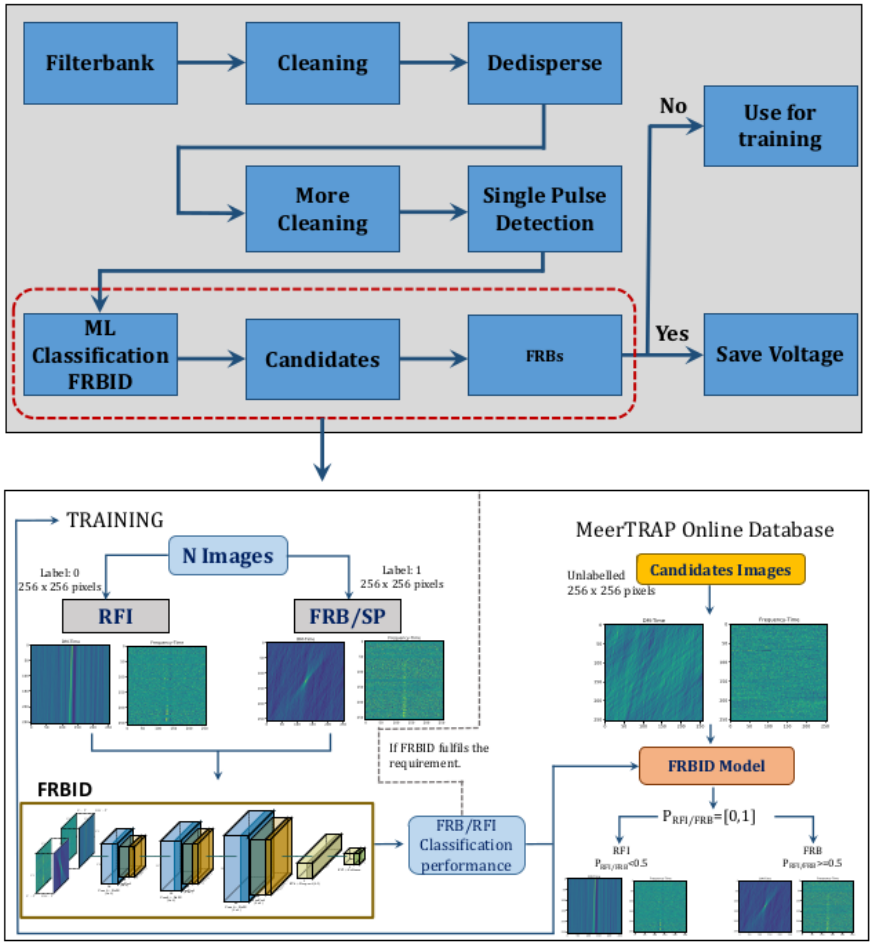

Figure 5.1 MeerTRAP signal processing pipeline and FRBID[FRBID]

Supervised learning entails training a model using labeled data, where each data point is associated with a known outcome or classification. In the context of FRBID, the task can be framed as a computer vision problem within the domain of machine learning [155]. Single pulse detection can be considered a binary classification task where based on input images/features/input variables/instances the pulse is either an FRB-like pulse or noise-RFI. For FRBID these features are discrete and have classification labels as ground truth decided by humans. A single pulse in the frequency domain will have a dispersion sweep that shows up as a bow-tie shape in dispersion trial-time plots. FRBID is trained to look for a pulse in frequency time and characteristics bow tie in dispersion trial-time plots. Therefore the input to the FRBID deep learning approach is these two plots shown in Figure 5.2. The FRBID is a binary, discrete, finite category classification tool. To convert information about each instance into quantifiable information supervised classification is followed.

A deep learning classification problem in simple words can be stated below. Here, f is a feature map, $\mathbf{X}$ is an input vector, W kernel, b is vector bias and α is a nonlinear activation factor.

$$f = \alpha\left(\mathbf{X} * \mathbf{W} + b\right) \tag{5.1}$$

A deep neural network can be categorised into three major components, liner convolutional layers, hidden non-linear layers and pooling. The convolution depth of the filter in the first layer is similar to the depth of the input image. Whereas several channels depend on parameters, for example, in an RGB image 3 channels of filter are considered. For radio transients and FRBID, 2 channels frequency-time and dispersion measure-time are considered. The filter slides over the input image and generates a feature map by convolution operation. For the second stage, a nonlinear activation feature ReLU is set up. The third layer is pooling. In most cases, maximum output in the rectangular grid is desired therefore max pooling is obtained.

Once components are assembled, a training task on a neural network is performed. Training of data often encounters errors such as overfitting and underfitting ie oversimplified/unreliable results. The underfitting of both training and data predictions is poor which means that the model requires more parameters to fit. To avoid this scenario slicing of the data is done and a verification task is performed to evaluate a model.

The most simple approach for splitting is to divide data in $\frac{2}{3}$ for training and $\frac{1}{3}$ for validation fractions. But there are other techniques for advanced splitting: holdout and K-fold cross-validation. During training, one needs to initialise all weights W to small random values and biases b to be initialised to 0 or small positive values. Split labelled data is given to the network and for supervised learning often forward propagation is performed on chunks of data. During the training task, optimisation of the cost function for the network is performed. The labels are

used to train neural network - the difference between a true label and classification probability is quantified by the cost function. For backward propagation gradient-based optimisation is performed. That is to optimise cost function and gradient descent with adjusting weights of the network. In most cases, the cost function is the maximum likelihood for the system. The training process is done in small batches of training data.

Data augmentation is generally used to avoid underfitting in the training process. Data augmentation involves creating modified versions of existing data points in your training set. These modifications introduce slight variations that the model might encounter in real-world scenarios, making it more robust and adaptable. In addition to quantifying the validity of the machine learning model, evaluation parameters are formulated such as balance accuracy, precision, recall, F1 score, sensitivity and specificity. These parameters are primarily based on true positive, true negative, false positive and false negative values.

- **True Positive/True Negative:** In the domain of classification tasks, True Positives (TP) and True Negatives (TN) serve as essential metrics for evaluating model performance. A True Positive signifies a correct classification of a positive instance. In the context of FRBID, this translates to accurately identifying a single pulse, akin to an image recognition system correctly classifying a "bow-tie" pattern as such. Conversely, a True Negative represents a successful prediction of a negative case. For FRBID, this would be correctly classifying any shape other than the "bow-tie" pattern, which falls under the category of RFI and is not considered a single pulse. By analysing these values alongside False Positives (incorrect positive predictions) and False Negatives (incorrect negative predictions), we gain valuable insights into the model's ability to distinguish between positive and negative examples. A high number of True Positives and True Negatives suggests the model is effectively learning the characteristic patterns that differentiate the two classes, leading to robust classification performance.

- **False Positive/False Negative:** Supervised learning models rely on False Positives (FP) and False Negatives (FN) as error indicators to reveal their limitations in classification tasks. A False Positive occurs when a negative instance is erroneously classified as positive. This is analogous to a spam filter mistakenly labeling a legitimate email as spam. Conversely, a False Negative arises when the model fails to detect a true positive case. In the context of FRBID, this could translate to missing a genuine single pulse. Analysing these errors is critical for model improvement. By understanding the nature of these misclassifications, we can refine the model's ability to differentiate between positive and negative examples, ultimately leading to enhanced overall performance.

- **Confusion matrix:** A confusion matrix is a valuable tool for evaluating the performance of classification models. It visualises the model's predictions by juxtaposing them against the ground truth labels (actual classifications) of the data. This matrix is structured with rows representing the true classes and columns representing the predicted classes. Each cell within the matrix quantifies the number of instances where the model predicted a specific class. Analysis of the confusion matrix proves instrumental in identifying areas for model improvement. For example, a high number of entries where the model predicted "not N-RFI" (implying a different class) for candidates that were actually RFI suggests potential deficiencies in the model's ability to capture relevant N-RFI features. Overall, the confusion matrix serves as a clear and informative technique for assessing a model's strengths and weaknesses in performing classifications.

- **Loss function:** The loss function serves as a cornerstone metric in evaluating the discrepancy between a model's predictions and the ground truth labels (actual classifications) of the data. In the context of FRBID, the loss function acts as a quantitative measure of N-RFI. A lower loss value signifies improved alignment between the model's predictions and the true values. Optimisation algorithms utilise the loss function to guide the model's learning process. By minimising the loss function, the model iteratively adjusts its internal parameters (weights and biases) with the objective of generating increasingly accurate predictions on unseen data. The selection of the appropriate loss function is crucial and depends on the specific classification task at hand. Monitoring the loss function during training offers valuable insights into the model's progress. This allows for the identification of potential issues such as overfitting (excessive memorisation of training data leading to poor generalisation) or underfitting (inability to capture the underlying patterns in the data). By guiding the model towards minimising the loss function, we steer it towards making more accurate predictions on future, unseen data.

- **Accuracy** of model: Accuracy, a prevalent metric in supervised learning, offers a general indication of a classification model's effectiveness. It is calculated as the proportion of predictions FRBID correctly classifies. While seemingly intuitive, accuracy has limitations, particularly for datasets with imbalanced class distributions. Consider FRBID's task of distinguishing between single pulses and N-RFI. If 99% of the data consists of single pulses, a model that perpetually predicts "N-RFI" would achieve a high accuracy (99%). However, this model would be ineffective as it would miss all genuine single pulses, leading to a high number of False Negatives (missed positive cases). To circumvent this limitation, accuracy should be employed in conjunction with other metrics such as precision, recall, and F1 score. These metrics delve deeper into the model's

ability to identify true positives (correctly classified positive cases) while minimising false positives (incorrectly classified positive cases) and false negatives. By incorporating this broader range of metrics, we gain a more nuanced understanding of the model's strengths and weaknesses in handling various classes within the data.

$$Accuracy = \frac{T_p + T_M}{T_p + F_p + T_N + F_N} \tag{5.2}$$

- **Precision:** Precision, also known as positive predictive value (PPV), is a critical metric in supervised learning, especially when evaluating models on imbalanced datasets. It quantifies the fraction of positive predictions that are genuinely correct. Analogy: Medical Diagnosis: Consider a medical diagnosis system classifying patients for a specific disease. Precision indicates the percentage of patients flagged as positive by the model who are truly afflicted with the disease. High precision is crucial in scenarios where false positives (incorrect positive classifications) carry significant consequences. For example, a high-precision security system would minimise false alarms, thereby reducing unnecessary security responses. Limitations of Precision: However, focusing solely on precision can be misleading. A model might achieve very high precision by simply predicting a negative outcome for all cases. While this approach guarantees no false positives, it also misses true positive cases entirely. Therefore, precision is often used in conjunction with other metrics like recall (the ability to identify true positives) to provide a more comprehensive picture of the model's effectiveness across different classes. A critical aspect of evaluating FRBID's performance hinges on analysing both precision and recall. Precision refers to the fraction of identified FRBs that are genuine, ensuring a minimal number of false positives (incorrect FRB classifications). Conversely, recall reflects the model's ability to detect true positive cases, preventing the omission of actual FRBs. By carefully examining both metrics, one can achieve a well-balanced model that effectively minimises false positives while maintaining a high success rate in identifying true FRBs.

$$\text{Precision} = \frac{T_p}{T_p + F_p} \tag{5.3}$$

- **Recall:** Also known as sensitivity or true positive rate (TPR), is another critical metric in supervised learning. It emphasizes the model's capacity to identify all genuine positive instances. In simpler terms, recall reflects the proportion of actual positive cases that the model correctly classifies as positive. Analogy: Spam Email Filtering: Consider a system

filtering emails for spam. Recall focuses on the system's effectiveness in capturing actual spam emails, minimising the number of False Negatives (emails incorrectly classified as not spam). High recall is essential in scenarios where missing positive cases carry significant weight. For instance, a medical diagnosis system with high recall strives to ensure it doesn't overlook any potential diseases in patients. Trade-off with False Positives: However, an exclusive focus on recall can lead to an increase in False Positives (unnecessary alarms). For example, a security system with perfect recall might flag every event as an intrusion, resulting in wasted resources investigating false alarms. Therefore, recall is often employed in conjunction with other metrics like precision to establish a balanced perspective on the model's performance across different classes. Joint analysis of precision and recall allows for the optimisation of the model's ability to identify true positives while minimising the generation of false alarms.

$$recall = \frac{T_p}{T_p + F_N} \tag{5.4}$$

- **F1 score:** The F1-score serves as a harmonic mean in supervised learning, providing a balanced assessment by incorporating both precision and recall. Precision reflects the proportion of positive predictions that are truly correct, while recall emphasizes the model's ability to identify all relevant positive cases. The F1-score merges these metrics by calculating their harmonic mean, thereby penalising models that excel in one metric but struggle in the other. A high F1-score signifies that the model achieves a well-balanced performance, minimising both False Positives (incorrect positive predictions) and False Negatives (missing true positives). This is particularly advantageous for imbalanced datasets, where a model might prioritize predicting the dominant class and overlook the less frequent but potentially crucial positive cases. The F1-score offers a more comprehensive perspective compared to relying solely on precision or recall. Therefore, it is a valuable metric for tasks where both identifying true positives and minimising false positives are of significant importance.

$$f1 = 2 \times \frac{Precision \times Recall}{Precision + Recall} \tag{5.5}$$

The following section presents an algorithm for processing filterbank data. This algorithm generates frequency-time and dispersion measure (DM)-time features to be utilised by FRBID.

5.2 Data processing for FRBID

Input data to FRBID: The FRBID system operates on two pre-processed input plots: dispersion measure (DM)-time and frequency-time (as illustrated in Figure 5.1). This normalisation

step ensures the plots are independent of factors like frequency-time resolution and the true DM value. This work introduces a novel approach for resizing the DM-time plots. Figure 5.1 depicts the original input format employed by the previous FRB classifier system, encompassing both DM-time and frequency-time representations. The DM-time plot was generated by conducting trials across a range of dispersion measures, extending from zero to two times the true DM value. Our analysis revealed a bias in the prior FRB classifier against FRBs with high dispersion measures. To overcome this limitation, this work proposes a method for resynthesising the DM-time plots directly from the input frequency-time data. This resynthesis process strategically restricts the DM trial range to values that are multiples of the pulse width. An additional advantage of this refined DM trial approach is the mitigation of artefacts caused by zero-DM Radio Frequency Interference (RFI) within the DM-time plane.

5.2.1 Determining DM Trials

A top hat/Gaussian pulse of the transient candidate has a time resolution briefly introduced in Equation 1.1 we use here,

$$W^2 = (W_{int})^2 + (t_{samp})^2 + (\Delta t_{DM})^2 + (\Delta t_{DMerr})^2 + (\tau_s)^2 \tag{5.6}$$

- W^2 - width_ms observed time resolution obtained from the MeerTRAP real-time pipeline
- $(W_{int})^2$ - intrinsic pulse width
- $(t_{samp})^2$ - sampling time
- $(\Delta t_{DM})^2$ - dispersive delay across an individual frequency channel inversely proportional to the bandwidth
- $(\Delta t_{DMerr})^2$ - dispersive delay corresponds to slightly incorrect dispersion, for FRBID analysis taken to be $30 * width\_ms$
- $(\tau_s)^2$ - scattering timescales, assumed negligible for determining the DM trials

$$\Delta DM = \frac{delay\_factor \times pulse\_width_{second}}{k_{DM} \times (freq\_low^{-2} - freq\_high^{-2})} \tag{5.7}$$

The equation demonstrates that varying the DM offset (Δt_{DMerr}) in multiples of the pulse width allows for the estimation of an appropriate DM trial range for pulses with a defined area. This approach, where DM trials are restricted based on pulse width instead of the true/optimal/best DM value, effectively magnifies the DM-time plane. This magnification facilitates the identification of high-dispersion measure (DM) FRBs that were previously missed

by the older FRBID system. Notably, the image resolution of the DM-time plane (256x256) is maintained for consistency with the prior setup, even with the new DM trial range. It is well-established that the signal-to-noise ratio (SNR) of a pulse exhibits an inverse square root proportionality to its width (W) as referenced in [156]. In simpler terms, wider pulses generally have lower SNR. For example, restricting DM trials within a range of ±30 times the pulse width will generate a DM-time plane that excludes regions where the SNR falls below 18.257% of its peak value. This strategic exclusion helps focus on the most promising areas within the DM-time plane for FRB detection.

5.2.2 Processing Image/Filterbank data

For generating and processing, filterbank generated a script to label data and generate a list of parameters. Following is the GUI output of the script.

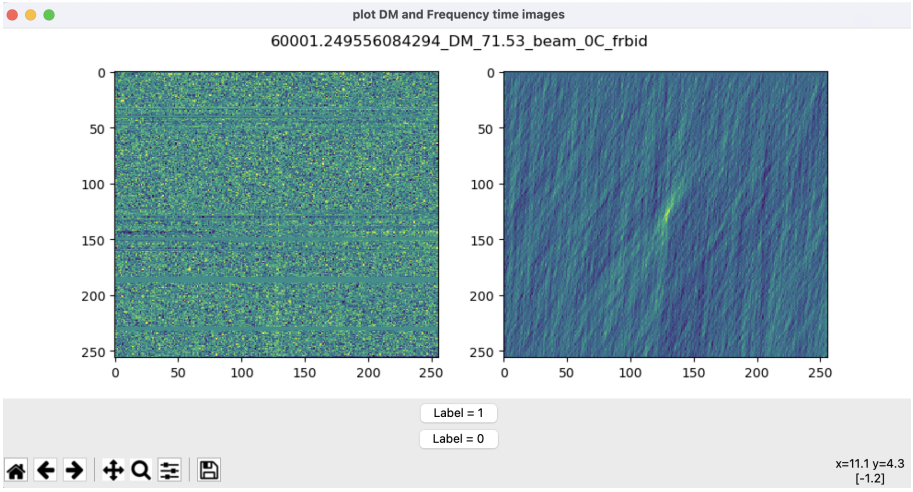

Figure 5.2 GUI output from the preprocessing script

We processed Filterbank data to improve the resolution of the dispersion measure 'bow-tie' structure along the time sample axis. The standard procedure of zero-DMing [157] for broadband RFI and elementary thresholding for narrowband RFI has been performed on the filterbank data. We generated the DM-time plane using the aforementioned algorithm applied to the filter bank data. While time averaging was employed, the DM-time plane included a cut proportional to the maximum DM shift on either side of the signal arrival time.

For estimating the FRBID system's performance after applying a new set of DM trials, processing for February 2023 is underway. We utilised a script for human classification, followed by feeding the data to the FRBID classifier. The FRBID with an edited input dataset can identify high DM FRBs in the analysis. Following is an algorithm walk-through of steps for generating DM-trail limited inputs to FRBID.

The first step is to determine DM cutoffs for each single pulse as explained in the section above;

Preprocessing of filterbank data targeted the enhancement of the dispersion measure (DM) "bow-tie" structure's resolution along the time sample axis. This involved standard procedures for mitigating Radio Frequency Interference (RFI):

- **Zero-DMing:** This technique, as described in [157], addresses broadband RFI. The zero-DM filter removes broad-band RFI signals by taking the average of all frequency channels in each time sample and subtracting this average from each frequency channel. Since RFI is generally undispersed, it appears as a simultaneous rise across all frequency channels, and this subtraction effectively removes it. This filtering process produces a high-pass filter, meaning low-frequency signals are attenuated. While this can affect the signal-to-noise ratio of faint pulsars, it also significantly reduces the amount of RFI and enhances the visibility of dispersed signals. This technique benefits the search algorithm by, improving the quality of pulsar search data by reducing the number of spurious candidates. It eliminates the need for other, more complex RFI excision techniques like clipping or zapping.

- **Elementary Thresholding:** This approach targets narrowband RFI. The Inter-Quartile Range Mitigation (IQRM) is a new RFI mitigation algorithm deployed on the MeerTRAP pipeline [158] that cleans the data from narrow-band RFI by automatically generating an adaptive, time-variable mask. This means that IQRM can identify and mask RFI that is not stationary in frequency and time. This is a significant improvement over previous methods of RFI mitigation, which relied on static frequency channel masks or zero-DM excision. The IQRM algorithm works by first calculating the interquartile range (IQR) of the data in each frequency channel. The IQR is a measure of the spread of the data, and it is calculated by subtracting the first quartile (25th percentile) from the third quartile (75th percentile). RFI is typically characterized by having a much larger IQR than the rest of the data. The IQRM algorithm then creates a mask that flags any frequency channel where the IQR exceeds a certain threshold. This mask is then used to remove the corrupted data from the pipeline. The IQRM algorithm is very effective at removing narrow-band RFI, and it has been shown to improve the quality of the data processed by MeerTRAP significantly. In addition to the static frequency channel mask, IQRM helps to remove any remaining RFI that is not detected by the static channel mask.

Following preprocessing, we employed the filterbank data to generate the DM-time plane utilising the aforementioned algorithm in Subsection 5.2.1. We applied time averaging to the DM-time plane generated from the preprocessed filterbank data. With our algorithm, the

plane was truncated proportionally to the maximum DM shift on either side of the signal arrival time. Evaluation of the FRBID system's performance with this new DM trial set, focusing on data from February 2023, is ongoing. We employed a processing script for human classification, followed by feeding the data to the FRBID classifier. This modification to the FRBID input dataset enables the identification of high-DM FRBs during analysis. Nevertheless, it is important to acknowledge that the system did miss a small number of strong SNR FRBs.

```
if "/cand/detection/filterbank" in h5_data :
    freq_bot  =  freq_top + chan_band_mhz*nchans
else :
    freq_bot  =  freq_top + chan_band_mhz*nchans_ml

#get exccess DM worth of 16*pulse_width
fudge_factor = 14
delta_dm =~(fudge_factor*~(width_ms * 1e-03)) /~(k_dm*~(freq_bot**-2 -
 freq_top**-2))

if delta_dm > cand_dm :
  delta_dm = cand_dm
  print~(f"get_dm_range : Warning: DM trial values will become
negative, therefore DM offset is {-delta_dm:.5} to {delta_dm:.5}")
else:
  print~(f"get_dm_range : The DM offset range {cand_dm-delta_dm:.5} to
 {cand_dm+delta_dm:.5} for true DM of {cand_dm:.5}")
  # print~(f"DM trial runs until SNR value drops to {pulse_snr/~(
fudge_factor**0.5):.5} approximately {~(1/fudge_factor**0.5*100):.5}%")
```

A time-domain cutoff is applied to the filterbank data to achieve a trade-off between computational efficiency and data fidelity. This approach facilitates expedited processing while mitigating potential difficulties in handling the entire dataset. The code patch is designed to calculate the appropriate delay DM offset range for a given radio signal. It does this by considering the signal's frequency, bandwidth, and pulse width. First, it calculates the maximum possible DM offset based on the signal's frequency range and the pulse width. This is done by multiplying the signal's bandwidth by the pulse width and dividing by the square of the signal's frequency. The result is then multiplied by a "fudge factor" of 14, which accounts for uncertainties in the calculation. Next, the code checks if this maximum DM offset is greater than the candidate DM offset, which is the estimated DM offset based on other information. If it is, the maximum DM offset is set to the candidate DM offset. Finally, the code prints a message indicating the appropriate DM offset range. This range is defined as the candidate DM offset plus or minus the maximum DM offset. This patch is useful for optimising the

search for radio signals from pulsars, fast radio bursts, and other transient sources. By correctly identifying the DM offset range, astronomers can more efficiently search for these signals within their data.

```
 #get a time sample slice
 time_shift_per_freq_in_s = k_dm*delta_dm*~(freq_bot**-2 - freq_top
**-2)
 print~("get_tsmp_range : time_shift_per_freq_in_s",
time_shift_per_freq_in_s)
 delta_tsmp = int~(time_shift_per_freq_in_s/tsamp)
 print~("get_tsmp_range : delta_time_samp", delta_tsmp)

 if~(delta_tsmp < 128*time_avg)  :
    delta_tsmp = 128*time_avg

 if~(time_samp_cand < delta_tsmp) :
         delta_tsmp = int~(time_samp_cand/128)*128

         print~(f"Warning: Keeping all the time samples from in the
Filterbank data and need to pad data for averaging")
         print~(f"The signal is coming at the timesample of {
time_samp_cand} and we will slice {time_samp_cand} around arrival-time
on both sides")
         #print~("get_tsmp_range : delta_time_samp", delta_time_samp)
 else :
         #print~(f"Acquired time samples for freq-t and dm-t : {
delta_time_samp*2}")
         print~(f"The signal is coming at the timesample of {
time_samp_cand} and we will slice {delta_tsmp} around arrival-time on
both sides")
```

The Python code snippet above is designed to determine the appropriate time window for analysing a signal received from a filterbank. The filterbank is a device that splits a wide range of frequencies into separate channels, each corresponding to a specific frequency band. The code begins by calculating the time shift per frequency `time_shift_per_freq_in_s` based on the DM and the frequency range. This time shift is essential for accounting for the delay caused by the interstellar medium, which varies depending on the frequency. the code calculates the `delta_tsmp`, which represents the time duration of the desired time sample. It checks if the `delta_tsmp` is within a certain threshold (128 times the average time interval). If it exceeds the threshold, it is adjusted to a multiple of 128. The if statement checks if the candidate time sample (`time_samp_cand`) is within the calculated delta_tsmp. If it's smaller, the code adjusts the `delta_tsmp` to a multiple of 128 based on the candidate time

	with processing		without processing	
	FRBs	**Total**	**FRBs**	**Total**
Training Set	745	1633	745	1633
Validation Set	189	409	189	409
Testing Set	934	2042	934	2042

Table 5.1 Number of examples used for training FRBID model. Training, validation and testing happen for 30 epochs each epoch consisting of an above number of candidates.

sample. If the `delta_tsmp` is too large (exceeding the threshold), a warning message is printed indicating that the code needs to pad the data for averaging.

The following logic is implemented to modify the HDF5 file,

```
freq_time = freq_time_fb_avg_candmaker.copy~()
dm_time = dm_time_fb_avg_candmaker.copy~()
ml_dataset = h5_data["/cand/ml/"]
print~(ml_dataset.keys~())
ml_dataset['dm_time'][:,:] = dm_time
ml_dataset['freq_time'][:,:] = freq_time
```

5.2.3 Training FRBID Model with Pre-processed data

A total of 2600 candidate signals were subjected to our pre-processing techniques. Of these, 1555 were classified as Noise - Radio Frequency Interference (N-RFI), while the remaining 1045 were identified as Fast Radio Bursts (FRBs). Figure 5.3 shows the ground truth labels of our data sample. The x-axis represents the dispersion measure and the y-axis represents the ground truth label. There are two clear clusters of data points: one around label=0 and the other around label=1. The data points around label=1 represent single pulses, while those around label=0 represent N-RFI.

Table 5.1 summarises the number of input data samples used to train FRBID. To prevent class imbalance within the training dataset, the numbers of single pulse and N-RFI samples were maintained at approximately equal levels. Furthermore, data from a limited number of days was excluded from the training analysis. The performance of the FRBID module is evaluated using the comparison metrics described earlier. This evaluation is performed for both scenarios: with and without preprocessing applied during the training phase. The results are presented in Figures 5.4, 5.5, and 5.6. For both the preprocessed and non-preprocessed training runs, the FRB and N-RFI samples (as detailed in Table 5.1) were divided roughly in half. This approach mitigates potential bias within the machine learning model.

The training process was executed for 30 epochs to ensure a balanced training regimen. This approach facilitates the development of a robust model less susceptible to biases. The

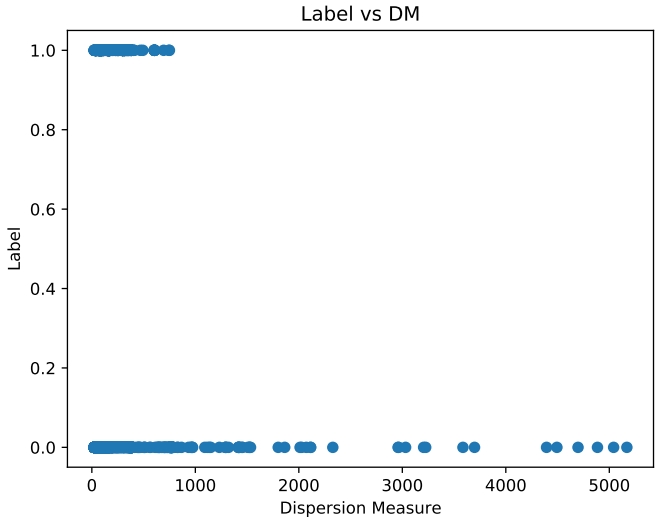

Figure 5.3 Ground Truth label of FRBID candidates for dispersion measure. Out of 1633 candidates, our training and validation set combined consists of 2024 samples, out of which 934 samples are single pulses and 1108 are N-RFI. We observe that for this sample, the DM of single pulses is between 21.49 to 607.386.

following section delves into the results obtained by evaluating the model parameters within the FRBID framework.

5.2.4 Quantifying FRBID with Evaluation Parameters

Our FRBID model achieved a substantially higher accuracy (0.981825) when trained on data that was preprocessed using our module. This represents a significant improvement compared to the model trained on non-preprocessed data (0.732615). As detailed in Table 5.2, a thorough evaluation of various metrics reveals that the preprocessed data leads to enhanced model performance across both precision and recall. This improvement is particularly advantageous for our analysis because our primary goal is to identify single FRBs amongst the overwhelming noise (N-RFI) in the data. The table shows the precision, recall, f1-score, and support for each class, as well as the average performance across all classes. The results show that the model performs better with preprocessing. For example, the f1-score for the "RFI" class is 0.98 with preprocessing, but only 0.72 without preprocessing. The table also shows that the model has a higher accuracy with preprocessing (0.98) than without preprocessing (0.73). Overall, the results suggest that preprocessing is beneficial for this classification task.

In this context, high recall is crucial. Recall refers to the model's ability to correctly identify all true FRBs. By achieving a high recall with preprocessed data, our model minimises the chances of missing actual FRBs. The model makes fewer mistakes in classifying FRBs from

	with processing				without processing			
	precision	**recall**	**f1-score**	**support**	**precision**	**recall**	**f1-score**	**support**
RFI	0.98	0.99	0.98	1108	0.83	0.64	0.72	1108
FRB	0.99	0.98	0.98	934	0.66	0.85	0.74	934
Accuracy	-	-	0.98	2042	-	-	0.73	2042
Macro avg	0.98	0.98	0.98	2042	0.75	0.74	0.73	2042
Weighted avg	0.98	0.98	0.98	2042	0.75	0.73	0.73	2042

Table 5.2 Classification Report with preprocessing and without processing

noise. The model effectively identifies the vast majority of true FRBs present in the data. This is particularly important for our analysis since we are primarily interested in finding as many FRBs as possible, even if it means including a few false positives (classifying noise as an FRB). This trade-off between accuracy and recall is acceptable in our case because missing even a single true FRB could be scientifically significant.

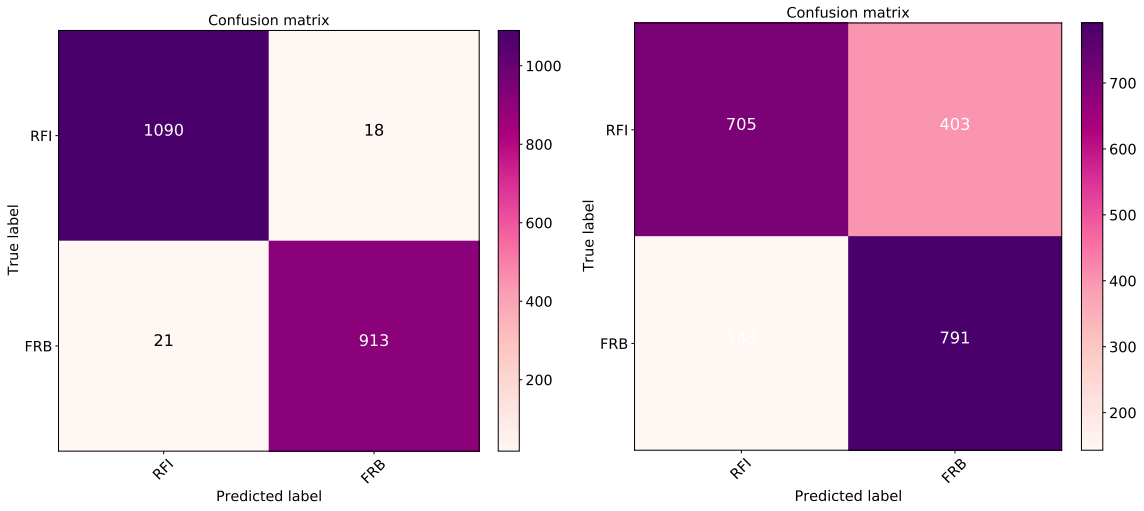

Figure 5.4 Confusion matrix for FRBID left-hand side is with preprocessing and the right-hand side of the confusion matrix is without preprocessing

Figure 5.4 matrix shows the number of correctly and incorrectly identified samples for FRBID. The right-hand side of Figure 5.4 shows the performance of FRBID with processed data. We see that The model with preprocessing applied identifies 913 out of 934 single pulse or FRBs compared to that of 791 without a preprocessing module. The model performs better with preprocessing, with a higher number of correct classifications and fewer misclassifications. Preprocessing seems to have improved the model's ability to distinguish between N-RFI and FRB signals.

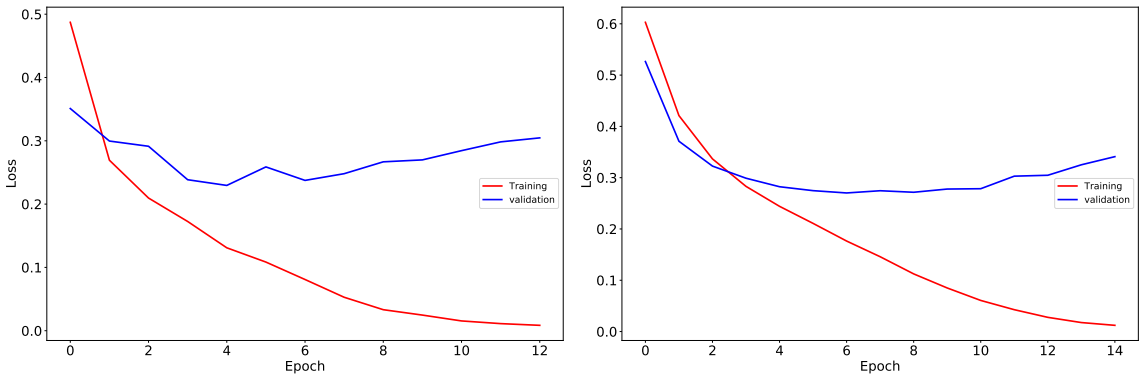

Figure 5.5 Loss of FRBID module with preprocessing and without preprocessing module. FRBID with preprocessing module provides optimised loss performance within a small number of epochs as shown on the right-hand side although with more unstable loss performance for the smaller epochs.

The image shows the loss curves of a FRBID model with and without a preprocessing module. The model with the preprocessing module converges faster, with a lower loss achieved after fewer epochs. However, the loss curve for the model with preprocessing is more unstable, especially at the beginning of training. This indicates that preprocessing can improve the convergence speed and final loss, but it can also lead to more fluctuating performance during training. This trade-off should be considered when deciding whether or not to use preprocessing.

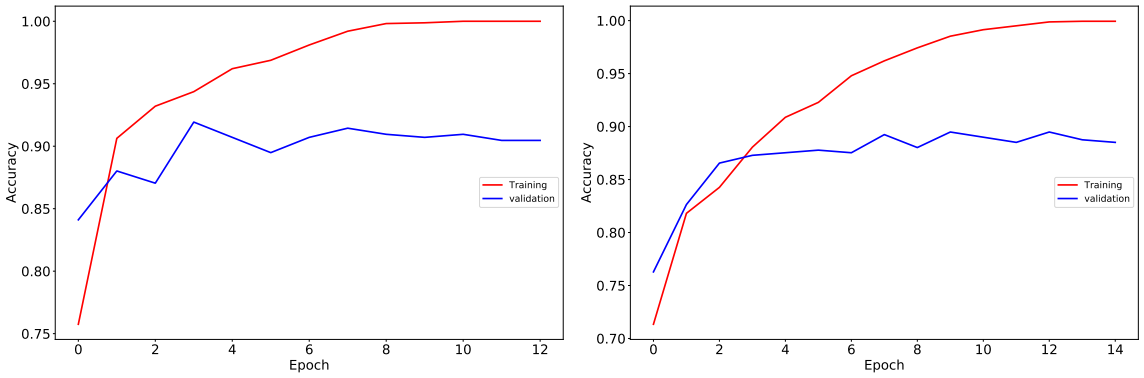

Figure 5.6 Accuracy matrix for FRBID, FRBID with preprocessing module provides optimised model accuracy within a small number of epochs as shown in the right-hand side although with more unstable performance for the smaller epochs.

The image shows two accuracy graphs for different models, likely based on the FRBID architecture. The left graph represents FRBID without any preprocessing module, while the right graph in Figure 5.6 shows the results for FRBID with preprocessing module. The graphs illustrate the accuracy of both training and validation sets across various epochs. The right-hand

graph demonstrates a much quicker and smoother convergence of the model towards high accuracy, particularly with respect to the validation set. This indicates that the preprocessing module, applied on the right-hand side model, effectively improves the model's performance and speeds up its convergence. However, the left-hand graph of Figure 5.6 reveals a more erratic behavior in the early epochs. Despite achieving a comparable accuracy level to the right-hand side graph after more epochs, the training and validation curves exhibit more fluctuations and less stability during the initial training stages. Overall, the visualisation highlights the beneficial impact of the preprocessing module in FRBID, resulting in a faster and more stable learning process, ultimately yielding a higher accuracy model.

5.2.5 Conclusion

In conclusion, this work, conducted within the framework of the MeerTRAP collaboration, focuses on preprocessing input data to enhance the performance of the FRBID classifier for archival datasets. We observed a bias in the previous FRBID classifier against high-dispersion measure FRBs. To address this limitation, we propose a method to resynthesise the DM-time plots from the raw frequency-time data. This resynthesis process restricts the range of DM trials to a multiple of the pulse width. This refined approach magnifies the DM-time plane by strategically clipping DM trials based on pulse width instead of relying on the true/optimal/best DM value. This modification facilitates the identification of high-DM FRBs that were previously missed by the older FRBID system. We maintain the image resolution of the DM-time plane at 256x256 for the new DM trial range to ensure consistency with the prior setup. It is well-established that the SNR of a pulse exhibits an inverse proportional relationship with half of the pulse width. For example, restricting DM trials within a range of ±30 times the pulse width generates a DM-time plane that excludes regions where the SNR falls below 18.257% of the peak SNR value. Evaluation of our preprocessing steps through system testing revealed improved performance and a requirement for fewer training epochs to achieve optimal performance.

6

Conclusion and Future Scope

Fast Radio Bursts (FRBs) constitute a profound research problem in contemporary radio astronomy, characterised by transient radio signals that burst forth with extraordinary luminosity over mere millisecond durations. Despite their remarkable intensity, the origins and underlying physical processes governing FRB emission remain a mystery. Nevertheless, FRBs have emerged as potent instruments for probing fundamental theories, including cosmology and general relativity. Our research endeavours have focused on categorising FRBs and leveraging them to impose constraints on the fraction of Primordial Black Holes (PBHs) through the analysis of lensed FRBs.

While characterising Fast Radio Bursts (FRBs) presents significant challenges, recent advancements offer promising avenues for exploration. High-precision localisation with telescopes like MeerKAT has yielded valuable insights. By pinpointing the host galaxies of FRBs, these observations provide crucial clues about their formation environments. To complement radio observations, a key area of current research involves multi-wavelength campaigns. These campaigns aim to identify potential electromagnetic counterparts to FRBs across the spectrum.

The future of FRB research is brimming with exciting possibilities. Advancements in telescope technology hold the key to unlocking the secrets of these phenomena. The next generation of telescopes will boast significantly enhanced sensitivity and resolution. This will allow us to: **Pinpoint the origins with greater precision:** By more accurately locating FRBs, we can identify their host galaxies and potentially even their specific stellar environments. This will shed light on the conditions that foster FRB creation. **Detect fainter bursts:** Increased sensitivity will open a window to a whole new population of fainter FRBs that may have previously gone undetected. This expanded dataset will be crucial for a more comprehensive understanding of FRBs. A larger and more diverse dataset of FRBs will pave the way for robust

statistical analysis. This analysis has the potential to reveal: **Sub-populations:** Unearthing distinct sub-groups within the FRB population based on their properties. This could hint at different origins or mechanisms at play. **Hidden patterns:** Identifying subtle trends or correlations within the data that might offer new insights into FRB behaviour. A powerful synergy exists between theoretical modelling and observations of repeating FRBs. By combining these approaches, we can: **Constrain progenitor models:** Refine existing theoretical models for FRB generation by comparing them to the observed characteristics of repeating FRBs. This will help us narrow down the most likely scenarios for how these bursts originate. **Test predictions:** Utilise observations of repeating FRBs to test the predictions made by various theoretical models. This iterative process will lead to a more comprehensive understanding of the physics behind FRBs.

The field of FRB research stands poised for a revolutionary leap forward with the advent of next-generation telescopes such as HIRAX, CHORD and SKA. These telescopes will boast unprecedented sensitivity, capable of detecting fainter FRBs that have eluded current instruments. Additionally, they will offer superior resolution, enabling us to pinpoint the origins of FRBs with much greater precision. This transformative capability is akin to transitioning from blurry, pixelated images to high-definition close-ups of the celestial realm.

Imagine not only identifying the host galaxy of an FRB but potentially even resolving its location within that galaxy – pinpointing its stellar birthplace. This newfound clarity will provide invaluable insights into the astrophysical environments that nurture FRB production. By correlating the location of FRBs with specific stellar populations or other galactic features (e.g., spiral arms, young star clusters, or the presence of massive black holes), we can begin to identify the physical conditions that trigger these powerful bursts. For instance, if a significant correlation is found between FRBs and regions of intense star formation, it could bolster theories suggesting the involvement of massive stars or stellar mergers in FRB generation. The increased sensitivity of next-generation telescopes will act as a cosmic key, unlocking a hidden population of fainter FRBs that have eluded detection thus far. This expanded dataset will be instrumental in constructing a more comprehensive statistical portrait of the FRB phenomenon. Consider the analogy of a botanist studying a flowerbed. With a limited view, they might only observe a few dominant flower species. However, with a wider lens, they can discover a richer diversity of flora, including smaller or less conspicuous plants. Similarly, the current FRB dataset might be biased towards brighter, more easily detectable bursts. Including fainter FRBs could reveal a more complete picture of the FRB population, potentially leading to the discovery of new sub-types or shedding light on the distribution of FRB energies. By analysing a larger and more diverse sample of FRBs, we can employ robust statistical methods to identify potential sub-populations within the FRB class. These sub-populations might be

differentiated by a variety of characteristics. Variations in pulse duration, dispersion measure (a measure of the interstellar medium's effect on the signal), or frequency could indicate distinct physical mechanisms at play. Some FRBs are mere milliseconds long, while others exhibit durations lasting tens of milliseconds. Unveiling any correlations between burst duration and other properties could provide valuable clues about the underlying processes. If distinct sub-populations are found to reside in fundamentally different environments (e.g., elliptical vs. spiral galaxies, active galactic nuclei vs. quiescent galaxies), it would strongly suggest diverse origins for these phenomena.

The existence of distinct sub-populations could be a crucial clue, hinting at the presence of diverse progenitor mechanisms responsible for FRB generation. For instance, one sub-population might be linked to the violent deaths of massive stars, while another could be associated with the energetic processes around supermassive black holes. A powerful synergy exists between theoretical modeling and observations of repeating FRBs. These unique objects, unlike their non-repeating counterparts, offer a chance to observe FRB activity from the same source on multiple occasions. This allows the community to test and refine existing theoretical models. Imagine having a glimpse into the inner workings of a complex machine by observing it in action multiple times. Similarly, by confronting theoretical predictions with real-world data from repeating FRBs, we can refine our understanding of FRB progenitors and the fundamental physics at play. Observations of repeating FRBs might reveal periodicities or patterns in their emission, which could then be used to constrain theoretical models and identify the most likely mechanisms responsible for FRB generation.

The study of FRBs is entering a new phase, characterised by enhanced observational and analytical capabilities. The integration of next-generation telescopes, advanced statistical methods, and a coordinated approach combining theoretical and observational perspectives is expected to facilitate significant progress in understanding FRBs. This development is anticipated to provide new insights into the physical mechanisms and properties of these transient events, ultimately advancing our knowledge of the astrophysical contexts in which they occur.

This collective effort holds the potential to revolutionise our understanding in several key areas: **Stellar Evolution:** By pinpointing the precise locations of FRBs within their host galaxies and potentially even identifying their stellar birthplaces, we can gain valuable insights into the final stages of massive star evolution. This newfound clarity could shed light on the specific stellar processes or environments that trigger FRB production. Are they associated with core-collapse supernovae, magnetar formation, or other exotic phenomena? Unveiling the stellar connection could fundamentally alter our understanding of the dramatic and explosive deaths of massive stars. **The Interstellar Medium:** FRBs act as powerful probes as they travel

through the vast expanse of space. By analysing the dispersion measure (DM) of their radio signals, we can probe the properties of the interstellar medium (ISM) along the line of sight. The increased sensitivity of next-generation telescopes will allow for the detection of even fainter FRBs, potentially from more distant locations. This expanded dataset will provide a more comprehensive picture of the ISM across different galaxies and environments, offering valuable insights into its composition, density variations, and potential effects on electromagnetic waves.
Fundamental Physics: The extreme nature of FRBs, with their immense energy densities and potentially short durations, pushes the boundaries of our current physical understanding. Observations of FRBs have the potential to challenge or even redefine fundamental physics concepts like Lorentz invariance, which dictates the relationship between space and time. While current data remains inconclusive, future observations with enhanced precision could reveal deviations from this principle, potentially leading to groundbreaking discoveries that reshape our cosmological perspective.

The upcoming era of FRB research promises to be a period of groundbreaking discoveries, not only for understanding these phenomena themselves, but also for shedding light on a multitude of scientific disciplines. As we delve deeper into the mysteries of FRBs, we stand at the precipice of a revolution in our understanding of the cosmos.

References

[1] B. J. Kavanagh, *bradkav/pbhbounds: Release version*, Nov., 2019. 10.5281/zenodo.3538999.

[2] D. R. Lorimer and M. Kramer, *Handbook of Pulsar Astronomy*. Cambridge University Press, 2012.

[3] D. R. Lorimer, M. Bailes, M. A. McLaughlin, D. J. Narkevic et al., *A Bright Millisecond Radio Burst of Extragalactic Origin*, *Science* **318** (2007) 777 [0709.4301].

[4] E. Platts, A. Weltman, A. Walters, S. P. Tendulkar et al., *A living theory catalogue for fast radio bursts*, Phys. Rep. **821** (2019) 1 [1810.05836].

[5] D. J. Champion, E. Petroff, M. Kramer et al., *Five new fast radio bursts from the HTRU high-latitude survey at Parkes: first evidence for two-component bursts*, MNRAS **460** (2016) L30 [1511.07746].

[6] C. D. Bochenek, D. L. McKenna, K. V. Belov et al., *STARE2: Detecting Fast Radio Bursts in the Milky Way*, PASP **132** (2020) 034202 [2001.05077].

[7] C. D. Bochenek, V. Ravi, K. V. Belov et al., *A fast radio burst associated with a Galactic magnetar*, Nature **587** (2020) 59 [2005.10828].

[8] CHIME/FRB Collaboration, B. C. Andersen, K. M. Bandura et al., *A bright millisecond-duration radio burst from a Galactic magnetar*, Nature **587** (2020) 54 [2005.10324].

[9] CHIME/FRB Collaboration, B. C. Andersen, K. Bandura, M. Bhardwaj et al., *CHIME/FRB Discovery of Eight New Repeating Fast Radio Burst Sources*, ApJL **885** (2019) L24 [1908.03507].

[10] K. Rajwade and J. van Leeuwen, *A needle in a cosmic haystack: A review of frb search techniques*, 2024.

[11] L. G. Spitler, P. Scholz, J. W. T. Hessels, S. Bogdanov et al., *A repeating fast radio burst*, Nature **531** (2016) 202 [1603.00581].

[12] S. Chatterjee, C. J. Law, R. S. Wharton, S. Burke-Spolaor et al., *A direct localization of a fast radio burst and its host*, Nature **541** (2017) 58 [1701.01098].

[13] H. Falcke and L. Rezzolla, *Fast radio bursts: the last sign of supramassive neutron stars*, A&A **562** (2014) A137 [1307.1409].

[14] T. Totani, *Cosmological Fast Radio Bursts from Binary Neutron Star Mergers*, PASJ **65** (2013) L12 [1307.4985].

[15] K. Kashiyama, K. Ioka and P. Mészáros, *Cosmological Fast Radio Bursts from Binary White Dwarf Mergers*, ApJL **776** (2013) L39 [1307.7708].

[16] X. Liu, *The Remnant of Neutron Star-White Dwarf Merger and the Repeating Fast Radio Bursts*, *Int. J. Astron. Astrophys.* **10** (2020) 28 [2002.03693].

[17] P. Kumar, W. Lu and M. Bhattacharya, *Fast radio burst source properties and curvature radiation model*, MNRAS **468** (2017) 2726 [1703.06139].

[18] W. Lu and P. Kumar, *The maximum luminosity of fast radio bursts*, MNRAS **483** (2019) L93 [1810.11501].

[19] W. Wang, R. Luo, H. Yue et al., *FRB 121102: A Starquake-induced Repeater?*, ApJ **852** (2018) 140 [1710.00541].

[20] Y. Lyubarsky, *A model for fast extragalactic radio bursts.*, MNRAS **442** (2014) L9 [1401.6674].

[21] S. R. Kulkarni, E. O. Ofek, J. D. Neill, Z. Zheng et al., *Giant Sparks at Cosmological Distances?*, ApJ **797** (2014) 70 [1402.4766].

[22] S. Kalita and A. Weltman, *Continuous gravitational wave detection to understand the generation mechanism of fast radio bursts*, MNRAS **520** (2023) 3742 [2211.00940].

[23] B. Zhang, *The physical mechanisms of fast radio bursts*, Nature **587** (2020) 45 [2011.03500].

[24] Z. J. Zhang, K. Yan, C. M. Li, G. Q. Zhang et al., *Intergalactic Medium Dispersion Measures of Fast Radio Bursts Estimated from IllustrisTNG Simulation and Their Cosmological Applications*, ApJ **906** (2021) 49 [2011.14494].

[25] V. Ravi, R. M. Shannon, M. Bailes, K. Bannister et al., *The magnetic field and turbulence of the cosmic web measured using a brilliant fast radio burst*, *Science* **354** (2016) 1249 [1611.05758].

[26] A. M. Cook, M. Bhardwaj, B. M. Gaensler, P. Scholz et al., *An FRB Sent Me a DM: Constraining the Electron Column of the Milky Way Halo with Fast Radio Burst Dispersion Measures from CHIME/FRB*, ApJ **946** (2023) 58 [2301.03502].

[27] M. Caleb, C. Flynn and B. W. Stappers, *Constraining the era of helium reionization using fast radio bursts*, MNRAS **485** (2019) 2281 [1902.06981].

[28] P. Beniamini, P. Kumar, X. Ma and E. Quataert, *Exploring the epoch of hydrogen reionization using FRBs*, MNRAS **502** (2021) 5134 [2011.11643].

[29] A. Walters, A. Weltman, B. M. Gaensler, Y.-Z. Ma et al., *Future Cosmological Constraints From Fast Radio Bursts*, ApJ **856** (2018) 65 [1711.11277].

[30] J. P. Macquart, J. X. Prochaska, M. McQuinn, K. W. Bannister et al., *A census of baryons in the Universe from localized fast radio bursts*, Nature **581** (2020) 391 [2005.13161].

[31] C. W. James, E. M. Ghosh, J. X. Prochaska et al., *A measurement of Hubble's Constant using Fast Radio Bursts*, MNRAS **516** (2022) 4862 [2208.00819].

[32] J.-J. Wei and F. Melia, *Investigating Cosmological Models and the Hubble Tension Using Localized Fast Radio Bursts*, ApJ **955** (2023) 101 [2308.05918].

[33] Q. Wu, G.-Q. Zhang and F.-Y. Wang, *An 8 per cent determination of the Hubble constant from localized fast radio bursts*, MNRAS **515** (2022) L1 [2108.00581].

[34] Q. Wu, G.-Q. Zhang and F.-Y. Wang, *Correction to: An 8 per cent determination of the Hubble constant from localized fast radio bursts*, MNRAS **531** (2024) L8.

[35] A. Caputo, L. Sberna, M. Frías, D. Blas et al., *Constraints on millicharged dark matter and axionlike particles from timing of radio waves*, Phys. Rev. D **100** (2019) 063515 [1902.02695].

[36] J.-J. Wei and X.-F. Wu, *Testing fundamental physics with astrophysical transients*, *Frontiers of Physics* **16** (2021) 44300 [2102.03724].

[37] D. Crichton, M. Aich, A. Amara et al., *Hydrogen Intensity and Real-Time Analysis Experiment: 256-element array status and overview*, *Journal of Astronomical Telescopes, Instruments, and Systems* **8** (2022) 011019 [2109.13755].

[38] L. B. Newburgh, K. Bandura, M. A. Bucher, T. C. Chang et al., *HIRAX: a probe of dark energy and radio transients*, in *Ground-based and Airborne Telescopes VI*, H. J. Hall, R. Gilmozzi and H. K. Marshall, eds., vol. 9906 of *Society of Photo-Optical Instrumentation Engineers (SPIE) Conference Series*, p. 99065X, Aug., 2016, DOI [1607.02059].

[39] A. Einstein, *Cosmological Considerations in the General Theory of Relativity*, *Sitzungsber. Preuss. Akad. Wiss. Berlin (Math. Phys.)* **1917** (1917) 142.

[40] A. Friedman, *On the Curvature of space*, *Z. Phys.* **10** (1922) 377.

[41] G. Lemaître, *A homogeneous universe of constant mass and increasing radius accounting for the radial velocity of extra-galactic nebulae*, MNRAS **91** (1931) 483.

[42] E. Hubble, *A Relation between Distance and Radial Velocity among Extra-Galactic Nebulae*, *Proceedings of the National Academy of Science* **15** (1929) 168.

[43] A. A. Penzias and R. W. Wilson, *A Measurement of Excess Antenna Temperature at 4080 Mc/s.*, ApJ **142** (1965) 419.

[44] R. H. Dicke, P. J. E. Peebles, P. G. Roll and D. T. Wilkinson, *Cosmic Black-Body Radiation.*, ApJ **142** (1965) 414.

[45] A. G. Riess, A. V. Filippenko, P. Challis, A. Clocchiatti et al., *Observational Evidence from Supernovae for an Accelerating Universe and a Cosmological Constant*, AJ **116** (1998) 1009 [astro-ph/9805201].

[46] S. Perlmutter, G. Aldering, G. Goldhaber, R. A. Knop et al., *Measurements of* Ω *and* Λ *from 42 High-Redshift Supernovae*, ApJ **517** (1999) 565 [astro-ph/9812133].

[47] Y. B. Zel'dovich, *Gravitational instability: An approximate theory for large density perturbations.*, A&A **5** (1970) 84.

[48] eBOSS collaboration, *Completed SDSS-IV extended Baryon Oscillation Spectroscopic Survey: Cosmological implications from two decades of spectroscopic surveys at the Apache Point Observatory*, *Phys. Rev. D* **103** (2021) 083533 [2007.08991].

[49] T. M. C. Abbott, M. Aguena, S. Allam, A. Amon et al., *Dark Energy Survey Year 3 results: A 2.7% measurement of baryon acoustic oscillation distance scale at redshift 0.835*, Phys. Rev. D **105** (2022) 043512 [2107.04646].

[50] Euclid Collaboration, R. Scaramella, J. Amiaux, Y. Mellier et al., *Euclid preparation. I. The Euclid Wide Survey*, A&A **662** (2022) A112 [2108.01201].

[51] J. J. Condon and S. M. Ransom, *Essential Radio Astronomy*. Princeton University Press, 2016.

[52] J. D. Romney, *Theory of Correlation in VLBI*, in *Very Long Baseline Interferometry and the VLBA*, J. A. Zensus, P. J. Diamond and P. J. Napier, eds., vol. 82 of *Astronomical Society of the Pacific Conference Series*, p. 17, Jan., 1995.

[53] E. R. Kuhn, B. R. B. Saliwanchik, K. Bandura, M. Bianco et al., *Antenna characterization for the HIRAX experiment*, in *Ground-based and Airborne Telescopes IX*, H. K. Marshall, J. Spyromilio and T. Usuda, eds., vol. 12182 of *Society of Photo-Optical Instrumentation Engineers (SPIE) Conference Series*, p. 1218225, Aug., 2022, DOI [2207.12461].

[54] E. F. Keane and E. Petroff, *Fast radio bursts: search sensitivities and completeness*, MNRAS **447** (2015) 2852 [1409.6125].

[55] A. Pescalli, G. Ghirlanda, R. Salvaterra, G. Ghisellini et al., *The rate and luminosity function of long gamma ray bursts*, A&A **587** (2016) A40 [1506.05463].

[56] L. Connor and V. Ravi, *Stellar prospects for FRB gravitational lensing*, MNRAS **521** (2023) 4024 [2206.14310].

[57] H. K. Vedantham, V. Ravi, G. Hallinan and R. M. Shannon, *The Fluence and Distance Distributions of Fast Radio Bursts*, *The Astrophysical Journal* **830** (2016) 75 [1606.06795].

[58] K. Vanderlinde, A. Liu, B. Gaensler, D. Bond et al., *The Canadian Hydrogen Observatory and Radio-transient Detector (CHORD)*, in *Canadian Long Range Plan for Astronomy and Astrophysics White Papers*, vol. 2020, p. 28, Oct., 2019, DOI [1911.01777].

[59] A. Recnik, K. Bandura, N. Denman, A. D. Hincks et al., *An Efficient Real-time Data Pipeline for the CHIME Pathfinder Radio Telescope X-Engine*, *arXiv e-prints* (2015) arXiv:1503.06189 [1503.06189].

[60] G. 't Hooft and M. Veltman, *One-loop divergencies in the theory of gravitation*, *Annales de L'Institut Henri Poincare Section (A) Physique Theorique* **20** (1974) 69.

[61] D. A. Howell, M. Sullivan, P. E. Nugent et al., *The type Ia supernova SNLS-03D3bb from a super-Chandrasekhar-mass white dwarf star*, Nature **443** (2006) 308 [astro-ph/0609616].

[62] R. A. Scalzo, G. Aldering, P. Antilogus et al., *Nearby Supernova Factory Observations of SN 2007if: First Total Mass Measurement of a Super-Chandrasekhar-Mass Progenitor*, ApJ **713** (2010) 1073 [1003.2217].

[63] R. Abbott, T. D. Abbott, S. Abraham et al., *GW190814: Gravitational Waves from the Coalescence of a 23 Solar Mass Black Hole with a 2.6 Solar Mass Compact Object*, ApJL **896** (2020) L44 [2006.12611].

[64] K. Huang, J. Hu, Y. Zhang and H. Shen, *The Possibility of the Secondary Object in GW190814 as a Neutron Star*, ApJ **904** (2020) 39 [2008.04491].

[65] S. Kalita and B. Mukhopadhyay, *Modified Einstein's gravity to probe the sub- and super-Chandrasekhar limiting mass white dwarfs: a new perspective to unify under- and over-luminous type Ia supernovae*, J. Cosmology Astropart. Phys. **2018** (2018) 007 [1805.12550].

[66] A. V. Astashenok, S. D. Odintsov and V. K. Oikonomou, *Maximal masses of white dwarfs for polytropes in R^2 gravity and theoretical constraints*, Phys. Rev. D **106** (2022) 124010 [2209.13693].

[67] G. J. Olmo, D. Rubiera-Garcia and A. Wojnar, *Stellar structure models in modified theories of gravity: Lessons and challenges*, Phys. Rep. **876** (2020) 1 [1912.05202].

[68] C. P. L. Berry and J. R. Gair, *Linearized f(R) gravity: Gravitational radiation and Solar System tests*, Phys. Rev. D **83** (2011) 104022 [1104.0819].

[69] S. Kalita and B. Mukhopadhyay, *Gravitational Wave in $f(R)$ Gravity: Possible Signature of Sub- and Super-Chandrasekhar Limiting-mass White Dwarfs*, ApJ **909** (2021) 65 [2101.07278].

[70] G. Lambiase, M. Sakellariadou and A. Stabile, *Constraints on extended gravity models through gravitational wave emission*, J. Cosmology Astropart. Phys. **2021** (2021) 014 [2012.00114].

[71] B. P. Abbott, R. Abbott, T. D. Abbott et al., *Gravitational Waves and Gamma-Rays from a Binary Neutron Star Merger: GW170817 and GRB 170817A*, ApJL **848** (2017) L13 [1710.05834].

[72] Y. Gong, E. Papantonopoulos and Z. Yi, *Constraints on scalar-tensor theory of gravity by the recent observational results on gravitational waves*, *Eur. Phys. J. C* **78** (2018) 738 [1711.04102].

[73] J. Oost, S. Mukohyama and A. Wang, *Constraints on Einstein-aether theory after GW170817*, Phys. Rev. D **97** (2018) 124023 [1802.04303].

[74] T. Gupta, M. Herrero-Valea, D. Blas, E. Barausse et al., *New binary pulsar constraints on Einstein-æther theory after GW170817*, *Classical and Quantum Gravity* **38** (2021) 195003 [2104.04596].

[75] L. Bonetti, J. Ellis, N. E. Mavromatos et al., *Photon mass limits from fast radio bursts*, *Phys. Lett. B* **757** (2016) 548 [1602.09135].

[76] H. Wang, X. Miao and L. Shao, *Bounding the photon mass with cosmological propagation of fast radio bursts*, *Phys. Lett. B* **820** (2021) 136596 [2103.15299].

[77] H.-N. Lin, L. Tang and R. Zou, *Revised constraints on the photon mass from well-localized fast radio bursts*, MNRAS **520** (2023) 1324 [2301.12103].

[78] J. B. Muñoz, E. D. Kovetz, L. Dai and M. Kamionkowski, *Lensing of Fast Radio Bursts as a Probe of Compact Dark Matter*, Phys. Rev. Lett. **117** (2016) 091301 [1605.00008].

[79] M. W. Sammons, J.-P. Macquart, R. D. Ekers et al., *First Constraints on Compact Dark Matter from Fast Radio Burst Microstructure*, ApJ **900** (2020) 122 [2002.12533].

[80] R. Laha, *Lensing of fast radio bursts: Future constraints on primordial black hole density with an extended mass function and a new probe of exotic compact fermion and boson stars*, Phys. Rev. D **102** (2020) 023016 [1812.11810].

[81] K. Liao, S. B. Zhang, Z. Li and H. Gao, *Constraints on Compact Dark Matter with Fast Radio Burst Observations*, ApJL **896** (2020) L11 [2003.13349].

[82] C. Leung, Z. Kader, K. W. Masui et al., *Constraining primordial black holes using fast radio burst gravitational-lens interferometry with CHIME/FRB*, Phys. Rev. D **106** (2022) 043017 [2204.06001].

[83] T. Treu and P. J. Marshall, *Time delay cosmography*, A&A Rev. **24** (2016) 11 [1605.05333].

[84] C. S. Kochanek and P. L. Schechter, *The Hubble Constant from Gravitational Lens Time Delays*, in *Measuring and Modeling the Universe*, W. L. Freedman, ed., p. 117, Jan., 2004, DOI [astro-ph/0306040].

[85] S. H. Suyu, P. J. Marshall, M. W. Auger, S. Hilbert et al., *Dissecting the Gravitational lens B1608+656. II. Precision Measurements of the Hubble Constant, Spatial Curvature, and the Dark Energy Equation of State*, ApJ **711** (2010) 201 [0910.2773].

[86] Ž. Ivezić, S. M. Kahn, J. A. Tyson, B. Abel et al., *LSST: From Science Drivers to Reference Design and Anticipated Data Products*, ApJ **873** (2019) 111 [0805.2366].

[87] Planck Collaboration, N. Aghanim, Y. Akrami, M. Ashdown et al., *Planck 2018 results. VI. Cosmological parameters*, A&A **641** (2020) A6 [1807.06209].

[88] B. Carr and F. Kuhnel, *Primordial Black Holes as Dark Matter Candidates*, *arXiv e-prints* (2021) arXiv:2110.02821 [2110.02821].

[89] A. M. Green and B. J. Kavanagh, *Primordial black holes as a dark matter candidate*, *Journal of Physics G Nuclear Physics* **48** (2021) 043001 [2007.10722].

[90] J. Liu, L. Bian, R.-G. Cai, Z.-K. Guo et al., *Primordial black hole production during first-order phase transitions*, Phys. Rev. D **105** (2022) L021303 [2106.05637].

[91] T. W. B. Kibble, *Topology of cosmic domains and strings*, *Journal of Physics A Mathematical General* **9** (1976) 1387.

[92] S. Bird, I. Cholis, J. B. Muñoz, Y. Ali-Haïmoud et al., *Did LIGO Detect Dark Matter?*, Phys. Rev. Lett. **116** (2016) 201301 [1603.00464].

[93] T. Naderi, A. Mehrabi and S. Rahvar, *Primordial black hole detection through diffractive microlensing*, Phys. Rev. D **97** (2018) 103507 [1711.06312].

[94] B. J. Carr, K. Kohri, Y. Sendouda and J. Yokoyama, *New cosmological constraints on primordial black holes*, Phys. Rev. D **81** (2010) 104019 [0912.5297].

[95] P. Jangra, D. Gaggero, B. J. Kavanagh and J. M. Diego, *The cosmic history of primordial black hole accretion and its uncertainties*, 2024.

[96] J. Koechler, *Phenomenology of dark matter indirect detection*, 2024.

[97] V. Suryanarayana Mummidi, P. Lamba and S. K. Vempati, *Supersymmetry: a decade after higgs discovery*, *Indian Journal of Physics* **97** (2023) 3315–3326.

[98] S. Profumo, *Ultralight primordial black holes*, 2024.

[99] D. H. Lyth, *Generating the curvature perturbation at the end of inflation*, J. Cosmology Astropart. Phys. **2005** (2005) 006 [astro-ph/0510443].

[100] J. C. Niemeyer and K. Jedamzik, *Dynamics of primordial black hole formation*, Phys. Rev. D **59** (1999) 124013 [astro-ph/9901292].

[101] P. Schneider, J. Ehlers and E. E. Falco, *Gravitational Lenses*. Springer-Verlag, Heidelberg, 1992, 10.1007/978-3-662-03758-4.

[102] A. J. Shajib, G. Vernardos, T. E. Collett, V. Motta et al., *Strong Lensing by Galaxies*, Space Sci. Rev. **220** (2024) 87 [2210.10790].

[103] P. Schneider and J. Schmid-Burgk, *Mutual coherence of gravitationally lensed images*, A&A **148** (1985) 369.

[104] N. Kaiser, *Weak Lensing and Cosmology*, ApJ **498** (1998) 26 [astro-ph/9610120].

[105] C. Alcock, R. A. Allsman, D. R. Alves, T. S. Axelrod et al., *The MACHO Project: Microlensing Results from 5.7 Years of Large Magellanic Cloud Observations*, ApJ **542** (2000) 281 [astro-ph/0001272].

[106] Y. Tsapras, *Microlensing Searches for Exoplanets*, *Geosciences* **8** (2018) 365 [1810.02691].

[107] J. M. Cordes and S. Chatterjee, *Fast radio bursts: An extragalactic enigma*, *Annual Review of Astronomy and Astrophysics* **57** (2019) 417–465.

[108] J. M. Cordes, I. Wasserman, J. W. T. Hessels, T. J. W. Lazio et al., *Lensing of fast radio bursts by plasma structures in host galaxies*, *The Astrophysical Journal* **842** (2017) 35.

[109] G. F. Marani, R. J. Nemiroff, J. P. Norris, K. Hurley et al., *Gravitationally lensed gamma-ray bursts as probes of dark compact objects*, *The Astrophysical Journal* **512** (1999) L13–L16.

[110] S. Weinberg, *Gravitation and Cosmology: Principles and Applications of the General Theory of Relativity*. Wiley, 1972.

[111] T. Multamäki and I. Vilja, *Spherically symmetric solutions of modified field equations in $f(R)$ theories of gravity*, Phys. Rev. D **74** (2006) 064022 [astro-ph/0606373].

[112] C. M. Will, *Theory and Experiment in Gravitational Physics*. Cambridge University Press, 2 ed., 2018, 10.1017/9781316338612.

[113] J. Khoury and A. Weltman, *Chameleon Fields: Awaiting Surprises for Tests of Gravity in Space*, Phys. Rev. Lett. **93** (2004) 171104 [astro-ph/0309300].

[114] J. Khoury and A. Weltman, *Chameleon cosmology*, Phys. Rev. D **69** (2004) 044026 [astro-ph/0309411].

[115] K. Atazadeh and M. Mousavi, *Vacuum spherically symmetric solutions in $f(T)$ gravity*, *Eur. Phys. J. C* **73** (2013) 2272 [1212.3764].

[116] CHIME/FRB Collaboration, M. Amiri, B. C. Andersen et al., *The First CHIME/FRB Fast Radio Burst Catalog*, ApJS **257** (2021) 59 [2106.04352].

[117] E. Fonseca, B. C. Andersen, M. Bhardwaj et al., *Nine New Repeating Fast Radio Burst Sources from CHIME/FRB*, ApJL **891** (2020) L6 [2001.03595].

[118] Chime/FRB Collaboration, B. C. Andersen, K. Bandura et al., *CHIME/FRB Discovery of 25 Repeating Fast Radio Burst Sources*, ApJ **947** (2023) 83 [2301.08762].

[119] J. M. Cordes and T. J. W. Lazio, *NE2001.I. A New Model for the Galactic Distribution of Free Electrons and its Fluctuations*, *arXiv e-prints* (2002) astro [astro-ph/0207156].

[120] A. Walters, A. Weltman, B. M. Gaensler, Y.-Z. Ma et al., *Future Cosmological Constraints From Fast Radio Bursts*, ApJ **856** (2018) 65 [1711.11277].

[121] T. Hashimoto, T. Goto, A. Y. L. On et al., *No redshift evolution of non-repeating fast radio burst rates*, MNRAS **498** (2020) 3927 [2008.09621].

[122] G. Hinshaw, D. Larson, E. Komatsu et al., *Nine-year Wilkinson Microwave Anisotropy Probe (WMAP) Observations: Cosmological Parameter Results*, ApJS **208** (2013) 19 [1212.5226].

[123] M. Rafiei-Ravandi, K. M. Smith, D. Li et al., *CHIME/FRB Catalog 1 Results: Statistical Cross-correlations with Large-scale Structure*, ApJ **922** (2021) 42 [2106.04354].

[124] N. Oppermann, L. D. Connor and U.-L. Pen, *The Euclidean distribution of fast radio bursts*, MNRAS **461** (2016) 984 [1604.03909].

[125] M. Caleb, C. Flynn, M. Bailes, E. D. Barr et al., *Are the distributions of fast radio burst properties consistent with a cosmological population?*, MNRAS **458** (2016) 708 [1512.02738].

[126] R. C. Zhang and B. Zhang, *The CHIME Fast Radio Burst Population Does Not Track the Star Formation History of the Universe*, ApJL **924** (2022) L14 [2109.07558].

[127] L. Iorio, M. L. Ruggiero, N. Radicella and E. N. Saridakis, *Constraining the Schwarzschild-de Sitter solution in models of modified gravity*, *Physics of the Dark Universe* **13** (2016) 111 [1603.02052].

[128] V. Kagramanova, J. Kunz and C. Lämmerzahl, *Solar system effects in Schwarzschild de Sitter space time*, *Physics Letters B* **634** (2006) 465 [gr-qc/0602002].

[129] M. Sereno and P. Jetzer, *Solar and stellar system tests of the cosmological constant*, Phys. Rev. D **73** (2006) 063004 [astro-ph/0602438].

[130] A. Alhamzawi and R. Alhamzawi, *Gravitational lensing by $f(R,T)$ gravity*, *Int. J. Mod. Phys. D* **25** (2016) 1650020.

[131] P. Bessa, *Strong gravitational lensing in Horndeski theory of gravity*, Phys. Rev. D **108** (2023) 024062 [2304.08141].

[132] C. Giocoli, M. Baldi and L. Moscardini, *Weak lensing light-cones in modified gravity simulations with and without massive neutrinos*, MNRAS **481** (2018) 2813 [1806.04681].

[133] X.-M. Kuang, Z.-Y. Tang, B. Wang and A. Wang, *Constraining a modified gravity theory in strong gravitational lensing and black hole shadow observations*, Phys. Rev. D **106** (2022) 064012 [2206.05878].

[134] S. C. C. Ho, T. Hashimoto, T. Goto, Y.-W. Lin et al., *Future Constraints on Dark Matter with Gravitationally Lensed Fast Radio Bursts Detected by BURSTT*, ApJ **950** (2023) 53 [2304.04990].

[135] Z. Pleunis, D. C. Good, V. M. Kaspi, R. Mckinven et al., *Fast Radio Burst Morphology in the First CHIME/FRB Catalog*, ApJ **923** (2021) 1 [2106.04356].

[136] T. Hashimoto, T. Goto, B. H. Chen, S. C. C. Ho et al., *Energy functions of fast radio bursts derived from the first CHIME/FRB catalogue*, MNRAS **511** (2022) 1961 [2201.03574].

[137] H.-Y. Guo and H. Wei, *A possible subclassification of fast radio bursts*, J. Cosmology Astropart. Phys. **2022** (2022) 010 [2203.12551].

[138] B. H. Chen, T. Hashimoto, T. Goto, S. J. Kim et al., *Uncloaking hidden repeating fast radio bursts with unsupervised machine learning*, MNRAS **509** (2022) 1227 [2110.09440].

[139] S. J. Kim, T. Hashimoto, B. H. Chen, T. Goto et al., *On the relationship between the duration and energy of non-repeating fast radio bursts: census with the CHIME data*, MNRAS **514** (2022) 5987 [2206.11330].

[140] X. Yang, S. B. Zhang, J. S. Wang and X. F. Wu, *Classifying FRB spectrograms using nonlinear dimensionality reduction techniques*, MNRAS **522** (2023) 4342 [2304.13912].

[141] J.-M. Zhu-Ge, J.-W. Luo and B. Zhang, *Machine learning classification of CHIME fast radio bursts - II. Unsupervised methods*, MNRAS **519** (2023) 1823 [2210.02471].

[142] CHIME/FRB Collaboration, M. Amiri, K. Bandura, P. Berger et al., *The CHIME Fast Radio Burst Project: System Overview*, ApJ **863** (2018) 48 [1803.11235].

[143] Y. Wang, H. Huang, C. Rudin and Y. Shaposhnik, *Understanding how dimension reduction tools work: An empirical approach to deciphering t-sne, umap, trimap, and pacmap for data visualization*, *Journal of Machine Learning Research* **22** (2021) 1.

[144] J. Murugan and D. Robertson, *An Introduction to Topological Data Analysis for Physicists: From LGM to FRBs*, *arXiv e-prints* (2019) arXiv:1904.11044 [1904.11044].

[145] M. Greenacre, P. Groenen, T. Hastie, A. Iodice D'Enza et al., *Principal component analysis*, *Nature Reviews Methods Primers* **2** (2022) 100.

[146] L. McInnes, J. Healy and J. Melville, *UMAP: Uniform Manifold Approximation and Projection for Dimension Reduction*, *arXiv e-prints* (2018) arXiv:1802.03426 [1802.03426].

[147] Y. Wang, H. Huang, C. Rudin and Y. Shaposhnik, *Understanding How Dimension Reduction Tools Work: An Empirical Approach to Deciphering t-SNE, UMAP, TriMAP, and PaCMAP for Data Visualization*, *arXiv e-prints* (2020) arXiv:2012.04456 [2012.04456].

[148] B. Zhang, *Fast radio burst energetics and detectability from high redshifts*, *The Astrophysical Journal Letters* **867** (2018) L21.

[149] S.-Q. Zhong, W.-J. Xie, C.-M. Deng, L. Li et al., *Can a Single Population Account for the Discriminant Properties in Fast Radio Bursts?*, ApJ **926** (2022) 206 [2202.04422].

[150] M. Amiri, B. C. Andersen, K. Bandura, S. Berger et al., *The First CHIME/FRB Fast Radio Burst Catalog*, ApJS **257** (2021) 59 [2106.04352].

[151] C. Tralie, N. Saul and R. Bar-On, *Ripser.py: A lean persistent homology library for python*, *The Journal of Open Source Software* **3** (2018) 925.

[152] H. J. van Veen, N. Saul, D. Eargle and S. W. Mangham, *Kepler mapper: A flexible python implementation of the mapper algorithm.*, *Journal of Open Source Software* **4** (2019) 1315.

[153] K. Rajwade, B. Stappers, F. Jankowski, M. Caleb et al., *Hunting for Fast Radio Bursts with MeerTRAP*, in *43rd COSPAR Scientific Assembly. Held 28 January - 4 February*, vol. 43, p. 1194, Jan., 2021.

[154] F. Jankowski, M. Berezina, B. W. Stappers, E. D. Barr et al., *Real-time triggering capabilities for Fast Radio Bursts at the MeerKAT telescope*, *arXiv e-prints* (2020) arXiv:2012.05173 [2012.05173].

[155] D. Agarwal, K. Aggarwal, S. Burke-Spolaor, D. R. Lorimer et al., *FETCH: A deep-learning based classifier for fast transient classification*, MNRAS **497** (2020) 1661 [1902.06343].

[156] J. M. Cordes and M. A. McLaughlin, *Searches for Fast Radio Transients*, ApJ **596** (2003) 1142 [astro-ph/0304364].

[157] R. P. Eatough, E. F. Keane and A. G. Lyne, *An interference removal technique for radio pulsar searches*, MNRAS **395** (2009) 410 [0901.3993].

[158] K. Rajwade, B. Stappers, C. Williams, E. Barr et al., *MeerTRAP in the era of multi-messenger astrophysics*, in *Ground-based and Airborne Instrumentation for Astronomy VIII*, C. J. Evans, J. J. Bryant and K. Motohara, eds., vol. 11447 of *Society of Photo-Optical Instrumentation Engineers (SPIE) Conference Series*, p. 114470J, Dec., 2020, DOI [2103.08410].